

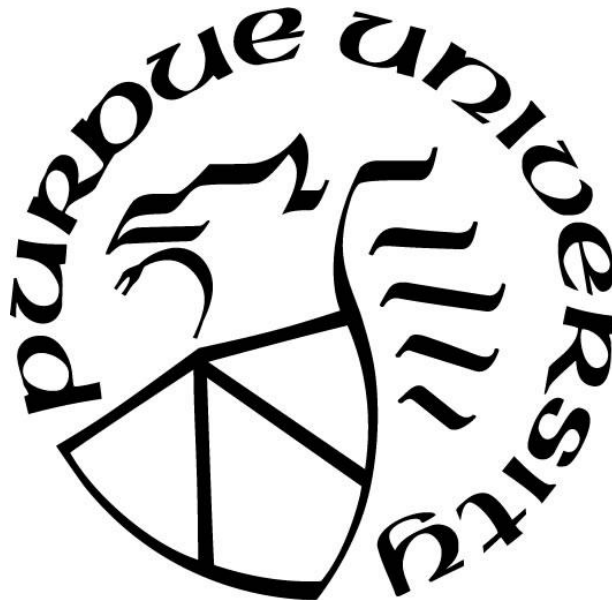
**COMPUTATIONAL INVESTIGATION OF CAVITY LEAKAGE FLOW
AND WINDAGE HEATING WITHIN AN AXIAL COMPRESSOR STATOR
WELL**

by
Nitya Kamdar

A Thesis

*Submitted to the Faculty of Purdue University
In Partial Fulfillment of the Requirements for the degree of*

Master of Science in Mechanical Engineering



School of Mechanical Engineering

West Lafayette, Indiana

December 2018

THE PURDUE UNIVERSITY GRADUATE SCHOOL
STATEMENT OF COMMITTEE APPROVAL

Dr. Nicole Key, Chair

School of Mechanical Engineering

Dr. Ivan Christov

School of Mechanical Engineering

Dr. Tom Shih

School of Aeronautics and Astronautics

Approved by:

Dr. Jay Gore

Head of the Graduate Program

“When you attend to things fully, when the doors of perception are cleansed, everything appears to man as it is. Infinite.” ~ Jason Silva

ACKNOWLEDGMENTS

On the very outset of this thesis, I would like to extend my sincere gratitude towards all the individuals who have helped me in this endeavor. This thesis becomes a reality with the kind support, active guidance and encouragement from many individuals without whom I would not have made headway in the project.

Foremost, I am extremely thankful to my advisor, Dr. Nicole Key, for her valuable guidance and support throughout this research as well as granting me the opportunity to be a part of an extraordinary compressor research lab where I was surrounded by incredible individuals and resources. I am also highly indebted to Purdue University and Dr. Nicole Key for the financial support in funding my education at a prestigious institution.

My appreciations also go to the members of the lab whose friendships, support, and expertise have been remarkable. I consider myself truly blessed to have had the opportunity to work amongst such a diligent and ingenious group. I would especially like to extend my gratitude towards: Doug Matthews for spending countless hours on coordinating ANSYS features in development of the computational model; Nicholas Kormanik for answering my incessant questions regarding the P3S geometry; and John Fabian for lending his computational and analytical expertise throughout this research. I would also like to acknowledge the efforts of previous investigators of P3S without whose meticulous documentation and comprehensive experimental data collection this computational model would not have become a reality.

A special thank you to all my friends, especially Nilkanth, Parth, and my Virginia Tech family, for their unwavering support and their ability to put a smile on my face throughout my time at Purdue University. At last but not least gratitude goes to my loving family. Nobody has been more important to me in the pursuit of this project than my parents, whose love and guidance have been with me in whatsoever I decide to pursue.

TABLE OF CONTENTS

LIST OF TABLES	8
LIST OF FIGURES	9
NOMENCLATURE	13
ABSTRACT.....	14
CHAPTER 1. INTRODUCTION	16
1.1 Motivation.....	16
1.2 Cavity Leakage Flows.....	17
1.2.1 Flow Path Overview	17
1.2.2 Interactions with Primary Flow	20
1.2.3 Cavity Flow Structure.....	21
1.3 Windage Effects.....	22
1.3.1 Cavity Heating	22
1.3.2 Re-ingestion of Hot Fluid	23
1.3.3 Interdependence of Leakage Flow and Windage Heating	24
1.4 Research Objectives.....	25
CHAPTER 2. CONFIGURATION DETAILS	27
2.1 Experimental Configurations	27
2.1.1 Facility Overview and Compressor Test Section	27
2.1.2 Steady Compressor Performance Measurements and Instrumentation	30
2.1.2.1 Primary Passage.....	30
2.1.2.2 Stator Cavity	32
2.1.3 Compressor Operating Conditions and Dataset Selection.....	34
2.2 Numerical Configurations.....	35
2.2.1 Main Passage Model.....	37
2.2.1.1 Discretization and Boundary Conditions.....	37
2.2.1.2 Domain Interfaces.....	39
2.2.1.3 Physics Solver Criteria	41
2.2.2 Cavity Flow Model Development	44
2.2.2.1 Discretization and Boundary Conditions.....	44

2.2.2.2 Domain Interfaces.....	47
2.3 Case Study and Analysis.....	48
2.3.1 Case Study	48
2.3.2 Data Extraction and Analysis	49
2.3.3 Grid Convergence Study.....	51
CHAPTER 3. INFLUENCE OF CAVITY LEAKAGE ON PRIMARY PASSAGE FLOW	56
3.1 Standalone and Coupled Cavity Model Comparison.....	56
3.2 Impact on Stage-wise and overall Compressor Performance	61
3.2.1 Overall Compressor Performance.....	61
3.2.2 Stator 1 Exit Performance.....	61
3.2.3 Cross-Passage Migration of Leakage Flow	66
3.2.4 Stator 1 Corner Separation.....	71
3.3 Inter-Stage Flow Profiles	73
3.3.1 Total Pressure and Total Temperature Profiles	73
3.3.2 Absolute Flow Angle and Momentum Variations	75
3.4 Cavity Flow Recirculation	80
3.4.1 Circumferential Variations at hub-cavity interfaces.....	81
3.4.2 Streamlines Indicating Re-ingestion.....	84
CHAPTER 4. CAVITY LEAKAGE FLOW CHARACTERISTICS IN STATOR WELLS	88
4.1 Near-hub Flow Variations.....	88
4.1.1 Radial Variations	88
4.1.2 Axial Variations.....	92
4.2 Cavity Leakage Flow Path.....	97
4.2.1 Cavity Inlet Well.....	97
4.2.1.1 Meridional Velocity Streamlines.....	97
4.2.1.2 Radial Variations in Flow Profiles	99
4.2.2 Cavity Outlet Well.....	106
4.2.2.1 Meridional Velocity Streamlines.....	106
4.2.2.2 Radial Variations in Flow Profiles	108
4.3 Windage Heating	115
4.3.1 Overall Temperature Rise.....	115

4.3.2 Overall Windage Work.....	116
4.4 Overall Cavity Leakage Flow Characteristics	118
CHAPTER 5. CONCLUSIONS AND RECOMMENDATIONS	121
APPENDIX A. ADDITIONAL RESULTS – CAVITY INLET WELL.....	126
APPENDIX B. ADDITIONAL RESULTS – CAVITY OUTLET WELL	131
REFERENCES	136

LIST OF TABLES

Table 1.1: Typical dimensions and parameters ranges for axial compressor cavities.....	19
Table 2.1: Radial Distributions of rake element locations.....	32
Table 2.2: Casing Temperature for isothermal shroud wall boundary conditions.....	39
Table 2.3: Summary of Boundary Conditions of the coupled model	48
Table 2.4: Typical dimensions and parameter ranges along with the range studied in this work	49
Table 2.5: Grid Convergence Study for the isolated Stator 1 and Cavity.....	52

LIST OF FIGURES

Figure 1.1: Stator Cavity Geometry and relevant terminology.....	18
Figure 1.2: Typical cavity parameters.	19
Figure 2.1: Purdue 3-Stage Axial Compressor Research Facility.	28
Figure 2.2: Cross Section of PAX100 Compressor Flow Path, Axial Location of Instrumentations, and Individual Blade counts.....	29
Figure 2.3: Generic Compressor Map.....	31
Figure 2.4: Stator 1 Cavity Geometry along with sensor locations.	33
Figure 2.5: Stator 3 Leakage Flow Path and manifold tubes from (a) the rear bearing plate to (b) an orifice plate run from Brossman (2012).....	34
Figure 2.6: Compressor Map with 100% Nc Speedline.	35
Figure 2.7: Geometric Model prior to model discretization.	37
Figure 2.8: Total Pressure and Total Temperature boundary conditions acquired from AIP measurements.....	39
Figure 2.9: A general connection representing Frame Change and Pitch Change Across a stator and a rotor.	40
Figure 2.10: Primary Passage model highlighting stage-mixing planes.....	41
Figure 2.11: Primary Passage model highlighting periodic interfaces.	41
Figure 2.12: Physical Timescale scheme as a function of iterations.	44
Figure 2.13: Cavities geometry cross sections in the coupled model.	45
Figure 2.14: Complete coupled model of the PAX100 geometry.	46
Figure 2.15: Stator domain division into inlet and outlet domains.....	46
Figure 2.16: Representation of rakes in the computational domain.	50
Figure 2.17: Representation of radial measurement planes in the cavity well.	50
Figure 2.18: Residuals of the coupled model following the grid convergence analysis.....	53
Figure 2.19: Results of grid convergence study in circumferential direction.....	54
Figure 2.20: Discretized fine grid in the stator passage domain.....	55
Figure 2.21: Discretized fine grid at the stator leading edge near-hub.....	55
Figure 3.1: Computational model accuracy on the compressor performance map with the black dot representing the experimental operating conditions for NL.	57
Figure 3.2: Total Pressure Radial Profiles comparing the standalone and coupled model with experimental data following GCS analysis.....	58

Figure 3.3: Total Temperature Radial Profiles comparing the standalone and coupled model with experimental data following GCS analysis.....	59
Figure 3.4: Absolute Flow Angle Radial Profiles comparing the standalone and coupled model with experimental data following GCS analysis.....	60
Figure 3.5: Impact of varying stator 1 seal clearance on compressor performance parameters... 61	
Figure 3.6: Comparison of Total Pressure contours at stator 1 exit for varying seal clearance. ..	63
Figure 3.7: Comparison of Total Temperature contours at stator 1 exit for varying seal clearance.	64
Figure 3.8: Comparison of absolute flow angle contours at stator 1 exit for varying seal clearance	65
Figure 3.9: Total Pressure contours at various axial locations indicating cross-passage migration of cavity leakage fluid.....	66
Figure 3.10: Total Temperature contours at various axial locations indicating cross-passage migration of hot cavity leakage fluid.	67
Figure 3.11: Comparison of axial velocity contours at stator 1 exit for varying seal clearance...	68
Figure 3.12: Comparison of circumferential velocity contours at stator 1 exit for varying clearance.	69
Figure 3.13: Comparison of radial velocity contours at stator 1 exit for varying seal clearance. 70	
Figure 3.14: Comparison of suction side streamlines on stator 1 vanes for varying seal clearance.	72
Figure 3.15: Total Pressure Radial Profiles comparison of varying seal clearance with experimental data.	73
Figure 3.16: Total Temperature Radial Profiles comparison of varying seal clearance with experimental data.	74
Figure 3.17: Absolute Flow Angle Radial Profiles comparison of varying seal clearance with experimental data.	76
Figure 3.18: Axial Velocity Radial Profiles comparison of varying seal clearance with standalone model.....	77
Figure 3.19: Circumferential Velocity Radial Profiles comparison of varying seal clearance with standalone model.	78
Figure 3.20: Radial Velocity profiles comparison of varying seal clearance with standalone model.	79
Figure 3.21: Radial velocity contours at the inlet and outlet cavity interfaces.....	82
Figure 3.22: Circumferential variations of Total Pressure, Axial, Circumferential, and Radial Velocity profiles for varying seal clearance at hub-cavity interface.	83
Figure 3.23: Velocity streamlines emerging from cavity outlet well and progressing through the stator passage for 0.250% span clearance case.	85

Figure 3.24: Velocity streamlines emerging from cavity outlet well and progressing through the stator passage for 1.000% span clearance case.	85
Figure 3.25: Velocity streamlines emerging from cavity outlet well and progressing through the stator passage for 1.375% span clearance case.	86
Figure 3.26: Velocity streamlines emerging from cavity outlet well and progressing through the stator passage for 1.750% span clearance case.	86
Figure 3.27: Velocity streamlines emerging from cavity outlet well and progressing through the stator passage for 2.500% span clearance case.	87
Figure 4.1: Total Pressure, Total Temperature, and Absolute Flow Angle radial profiles comparison of varying seal clearance near-hub and plunged into the cavity wells.	90
Figure 4.2: Axial, Circumferential and Radial Velocity profiles comparison of varying seal clearance near-hub and plunged into the cavity wells.	91
Figure 4.3: Meridional Streamlines near the inlet (right) and outlet (left) cavity interfaces of the 1.750 percent span clearance case at Leading Edge (Top) and Trailing Edge (Bottom).	93
Figure 4.4: Meridional Streamlines near the inlet (right) and outlet (left) cavity interfaces for varying seal clearance cases at the trailing edge of the stator.	95
Figure 4.5: Meridional Streamlines near the inlet (right) and outlet (left) cavity interfaces for varying seal clearance cases at the trailing edge of the stator.	96
Figure 4.6: Meridional Streamlines in the inlet cavity well for varying seal clearance cases.	98
Figure 4.7: Datum definitions for the radial variation profiles in the inlet and outlet wells.	99
Figure 4.8: Radial variations in flow profiles at radius ratio 0.99 in the cavity inlet well.	100
Figure 4.9: Radial variations in flow profiles at radius ratio 0.70 in the cavity inlet well.	101
Figure 4.10: Radial variations in flow profiles at radius ratio 0.212 in the cavity inlet well.	103
Figure 4.11: Radial variations in flow profiles at radius ratio 0.01 in the cavity inlet well.	105
Figure 4.12: Meridional Streamlines in the outlet cavity well for varying seal clearance cases.	107
Figure 4.13: Radial variations in flow profiles at radius ratio 0.212 in the cavity outlet well. ..	109
Figure 4.14: Radial variations in flow profiles at radius ratio 0.01 in the cavity outlet well.	110
Figure 4.15: Radial variations in flow profiles at radius ratio 0.70 in the cavity outlet well.	111
Figure 4.16: Radial variations in flow profiles at radius ratio 0.99 in the cavity outlet well.	112
Figure 4.17: Radial variations in flow profiles at radius ratio 0.212 throughout the cavity well.	114
Figure 4.18: Changes in total temperature at the hub-cavity interfaces for varying seal clearance and inlet circumferential velocity.	115
Figure 4.19: Change in total temperature inlet to outlet cavity interfaces for varying seal clearance and inlet circumferential velocity.	116

Figure 4.20: Windage heating contributions by the cavity for varying seal clearance as well as windage heating interdependence on inlet circumferential velocity.....	117
Figure 4.21: Changes in total pressure at the hub-cavity interfaces for varying seal clearance and inlet circumferential velocity.	118
Figure 4.22: Change in total pressure from inlet to outlet cavity interfaces for varying seal clearance and inlet circumferential velocity.	119
Figure 4.23: Circumferential velocity changes from inlet to outlet cavity interfaces for varying seal clearance and inlet circumferential velocity.	120
Figure 4.24: Changes in radial velocity at the hub-cavity interfaces for varying seal clearance and inlet circumferential velocity.	120
Figure A.1: Variations in flow profiles at radius ratio 0.01 in the cavity inlet well for varying seal clearance	126
Figure A.2: Variations in flow profiles at radius ratio 0.15 in the cavity inlet well for varying seal clearance	127
Figure A.3: Variations in flow profiles at radius ratio 0.30 in the cavity inlet well for varying seal clearance	128
Figure A.4: Variations in flow profiles at radius ratio 0.70 in the cavity inlet well for varying seal clearance	129
Figure A.5: Variations in flow profiles at radius ratio 0.99 in the cavity inlet well for varying seal clearance	130
Figure B.1: Variations in flow profiles at radius ratio 0.01 in the cavity outlet well for varying seal clearance	131
Figure B.2: Variations in flow profiles at radius ratio 0.15 in the cavity outlet well for varying seal clearance	132
Figure B.3: Variations in flow profiles at radius ratio 0.30 in the cavity outlet well for varying seal clearance	133
Figure B.4: Variations in flow profiles at radius ratio 0.70 in the cavity outlet well for varying seal clearance	134
Figure B.5: Variations in flow profiles at radius ratio 0.99 in the cavity outlet well for varying seal clearance	135

NOMENCLATURE

Symbols

a	Speed of sound
c_p	Specific heat capacity at constant pressure
δ	Identity Matrix
H	Convective heat transfer coefficient
h	Static Enthalpy
k	Thermal conductivity
L	Casing thickness
λ	Thermal Conductivity
\dot{m}	Mass Flow Rate
μ	Dynamic Viscosity
N	Rotational Speed
p	Static Pressure
ρ	Density
S_M	Momentum Source Term
S_E	Energy Source Term
τ	Shear Stress or molecular stress tensor
T	Static Temperature
\mathbf{U}	Vector of Velocity
W	Windage Work

Subscripts

act	Actual Condition
c	Corrected Conditions
$mech$	Mechanical
o, tot	Stagnation Condition
ref	Reference Condition

ABSTRACT

Author: Kamdar, Nitya, D. MSME

Institution: Purdue University

Degree Received: December 2018

Title: Computational Investigation of Cavity Leakage Flow and Windage Heating within an Axial Compressor Stator Well

Committee Chair: Dr. Nicole L. Key

The fundamental design of axial compressors has matured to an exceptional level of performance due to a century of research. With the improvements in efficiency becoming increasingly difficult, attention continues to be channeled towards understanding and reducing secondary losses such as hub or tip clearance leakages, seal leakages, etc. Studies detailing the impact of seal leakages are relatively scarce due to difficulties of obtaining data in the complex rotating geometries of a high-speed compressor cavity. While the impact of seal leakages on primary passage is readily available, details inside the cavity geometry is scarce in open literature because majority of the investigations have been performed on linear cascades with slots machined as cavities or standalone labyrinth seals that fail to provide a wholesome understanding of the leakage flow and windage heating in the rotating geometries.

Therefore, the principal objective of this work is to investigate flow physics in the stator cavity wells for understanding the flow path of the leakage fluid and windage heating within the cavity. A parametric model of the Purdue 3-Stage Compressor (P3S) is used to allow for rapid geometric modifications to the seal clearances in a coupled stator-cavity system. The investigations presented here consist of a series of numerical simulations using ANSYS CFX as the primary Computational Fluid Dynamics (CFD) tool. Measurements performed by previous investigators are utilized to define the boundary conditions of this model. This study's goal is to characterize the interdependence of parameters such as cavity leakage flow rate, circumferential velocity, and windage heating for understanding the flow structure inside the cavity wells and their impact on cavity temperatures. Data acquired is intended to reveal mechanisms through which cavity leakage flows affect the stator passage aerodynamics and the windage heating, both regarding their effect on the compressor performance and the details of the flow path within the cavity. Consequently, this will provide insight into how the complex cavity leakage flow influences the design considerations for optimizing stator passage aerodynamics and minimizing stator cavity heating.

The compressor operating conditions of Nominal Loading (NL) is the focus of this CFD work since the flow field at High Loading (HL) has significant boundary layer separation. NL is closest to both the design and peak efficiency conditions where the compressor would spend the majority of its time in operation, understanding cavity flow physics at this operating condition would have a direct impact on enhancing the overall compressor performance. A CFD model of the standalone primary passage is developed first using the dataset available from experiments performed by previous investigators for establishing confidence in the primary passage flow physics. Therefore, detailed total pressure, total temperature, velocity, and flow angle data collected behind each blade row is utilized for validating the primary passage flow in the CFD model. After validating the primary passage model, measurements in the coupled cavity model are acquired to understand the flow variations as well as temperature development in the cavity due to the varying labyrinth seal clearance.

The investigations in this work are divided into two distinct branches. First, to aid the aerodynamic research community, the flow structure inside the cavity wells is investigated to understand the impact cavity leakage flow has on the compressor efficiency and on its interactions with the primary flow path. Secondly, for understanding the development and rise of temperature in the cavity wells, i.e., the windage effect, are performed to aid the thermo-mechanical research community so that the material choices and stress analysis of the cavity components can be optimized. Hence, the trends in the data acquired provide the aerodynamic, mechanical, and secondary flow system designers an indication of the complexities of the flow within shrouded stator cavities and provide insight into designing and optimizing more complex geometries.

Results from this investigation describe how increasing seal clearance deteriorates the stator performance and enables the cross-passage migration of low momentum fluid to worsen hub corner separation. The simulations also state the case for re-ingestion at tight seal clearances as the 3D streamlines show heated efflux emerges from the upstream cavity interface, dwells near the hub, and gets recirculated back into the cavity inlet well. Radial variations inside the cavity wells show high cavity temperatures with excessive cavity due to re-ingestion, while the cases that avoid re-ingestion are observed at the lowest temperatures. These radial variations also identify the cavity leakage flow path and the development of circumferential velocity. Lastly, the total pressure loss, total temperature rise and windage heating, all show a strong dependence on circumferential velocity development, which is inherently dependent on the labyrinth seal clearances.

CHAPTER 1. INTRODUCTION

1.1 Motivation

Gas turbine engines have revolutionized the air travel and power generation industries. The fundamental design of a gas turbine engine has matured to an exceptional level of performance and reliability due to a century of research and development. Nevertheless, with environmental concerns and fiscal implications of rising fuel costs, engine companies continue to advance gas turbine engine development towards increased efficiency and lower fuel consumption. Due to the gas turbine engine technologies' high level of maturity, even slight gains in the engine efficiency are noteworthy. With the improvements in efficiency of gas turbine engine components (i.e., compressors and turbines) becoming increasingly difficult and expensive to accomplish, attention continues to be channeled towards understanding and reducing secondary losses. This drive for improved engine performance, coupled with advances in analytical and computational methods, allows to achieve these incremental improvements in compressor efficiency by understanding aerodynamic loss mechanisms such as hub or tip clearance leakages, seal leakages, corner separation, etc.

When leakage flows are not accounted for in the design process, efficiency of compressors are lowered from expected level as leakage flows alter the blockage and loss distributions in the primary flow path. Rotor blade tip clearance leakage has been actively studied, with numerous publications concerning the negative impact of this leakage on compressor performance. A general rule is to expect a 1.5-point reduction in efficiency for every 1 percent increase in the tip clearance-to-blade height ratio (Ludwig, 1978; Freeman, 1985) while stall margin can be reduced as much as 6 percent for every 1 percent increase in clearance-to-chord ratio (Wisler, 1988). Studies detailing the impact of other kinds of leakages on compressor performance are relatively scarce. The other leakages include shrouded blade seal leakage, rotor dovetail leakage, variable stator pivot/clearance leakage, and customer bleed.

Two common design considerations for the construction of stator vanes in axial-flow compressors are cantilevered or hub shrouded stators. Here, structural integrity such as avoiding the primary vibrational modes of first flex, first torsion, and two-stripe frequencies in the operating range outweigh the aerodynamic preferences (Wisler, 1988). Since shrouding provides the

mechanical stability desired, many modern engines utilize hub shrouded stators. Hence, the choice to employ hub shrouded stators eliminates losses linked to hub clearance leakage flows of cantilevered stators. Nevertheless, shrouding introduces shrouded stator leakage which entails flow recirculating backwards through the cavity due to the pressure differential across the stator, generally referred to as cavity leakage flow. In general, neglecting shroud leakage effects results in underpredicted hub temperatures, flow deviation, and overestimated efficiency (Naylor, 2009).

Consequently, the research into cavity leakage flow falls into two distinct areas. First, the aerodynamic research community, whose interest lies in understanding the impact cavity leakage flow has on the primary flow path and the compressor efficiency. Secondly, the air system and thermo-mechanical research community is concerned with understanding the local temperature rise in the cavity (i.e., the windage effect) so that the material choices and stress analysis of components adjacent to the cavity can be optimized. While a few experimental investigations focusing on cavity leakage effects have been conducted (Wellborn and Okishi, 1999; Phadke et al., 1987; Lewis, 2002), limited experimental data are readily available due to difficulties of obtaining data in the complex rotating geometries of a high-speed compressor seal cavity. Therefore, the use of computational fluid dynamics (CFD) as an investigative tool becomes very useful. Using CFD in a parameterized study allows for rapid geometry modifications in a coupled stator-cavity system to understand not only the interactions between the cavity leakage flow path and the primary flow path, but also understand its connection to windage heating. Doing so can help determine the areas of interest in the cavity geometry and experiments can be planned accordingly for further investigation.

1.2 Cavity Leakage Flows

1.2.1 Flow Path Overview

The shrouded stator vanes in an axial compressor are pinned between two concentric rings, the outer and the inner, with the outer fastened to the compressor housing while the rotor blades are mounted in grooves milled into the rotor blisks. Therefore, the rotor shaft must be manufactured with a cavity between two adjacent rotor discs to accommodate for the inner ring. In a high-speed axial compressor, the function of this stator seal cavity is to provide clearance

between the rotating rotor drum and the stationary inner ring (landing), which stabilizes the stator vanes. Figure 1.1 shows a stator cavity.

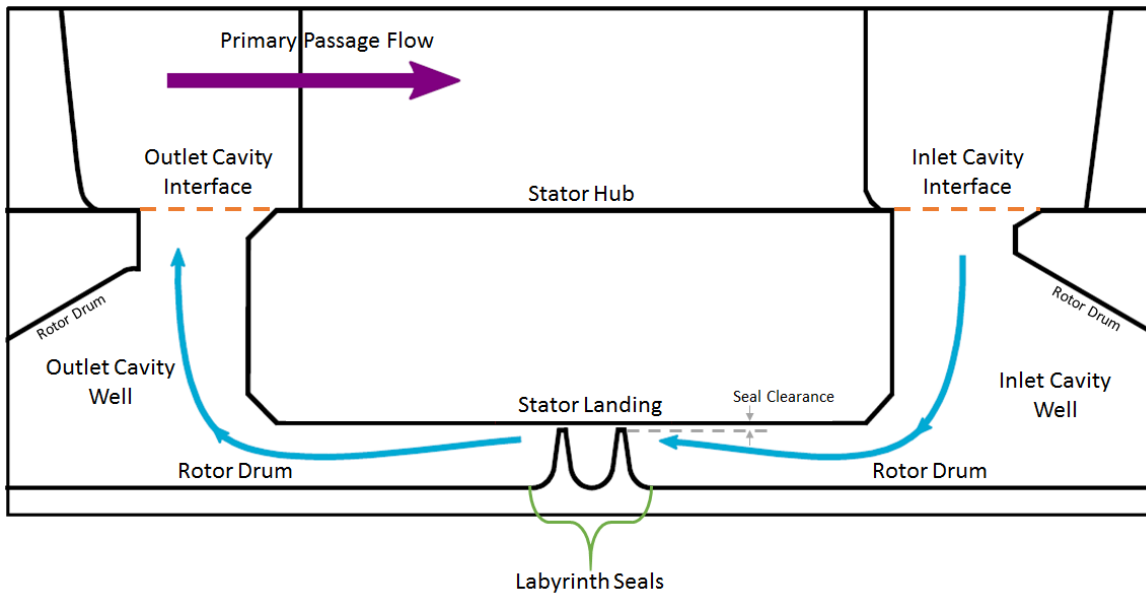


Figure 1.1: Stator Cavity Geometry and relevant terminology.

Static pressure increases through a stator which creates a pressure-driven path through the cavity in the opposite direction of the primary flow. Hence, to minimize the cavity leakage flow, a labyrinth seal is used. The tips of the labyrinth seals, i.e., seal teeth, protrude from the rotor shaft radially outwards towards the landing. However, the seal teeth must avoid physical contact to avert any type of failure or damage. Consequently, between the seal teeth and stator landing there must still exist a clearance, through which some flow recirculation in the direction opposite of the primary flow is possible. The function of the labyrinth seals is to dissipate energy by a sequence of constrictions and expansions. As the air flows across the seal teeth and landing, the potential energy is converted into kinetic energy, which is dispersed through turbulence and viscous dissipation in the cavity that follows, therefore increasing the resistance on the flow and, in turn, reducing the leakage flow rate. What sets a compressor stator labyrinth seal apart from a regular labyrinth seal is the inlet and outlet rotor-stator disc cavities (wells) and the long rotating walls. The flow structure, swirl characteristics, and windage heating in these stator wells can have a significant impact on the leakage characteristics of the labyrinth seal.

Lewis (2002) classified the typical dimensions and parameter ranges encountered by a compressor cavity. Table 1.1 tabulates the typical dimensions of an individual stator well that influence cavity leakage flow characteristics and windage heating. These dimensions are defined in Figure 1.2.

Table 1.1: Typical dimensions and parameters ranges for axial compressor cavities.

Parameter	Typical Range
Annulus Passage Height	1 to 2.5 in.
Hub Radius (from centerline)	10 to 13 in.
Seal Flow (fraction of annulus flow)	0.1% to 0.4%
Seal Clearance (% of span)	0.3% to 2.0%
Stator Well Depth	0.75 to 1 in.
Stator Inlet V_θ (fraction of U_{hub})	0.50 to 0.60
Stator Outlet V_θ (fraction of U_{hub})	0.05 to 0.08

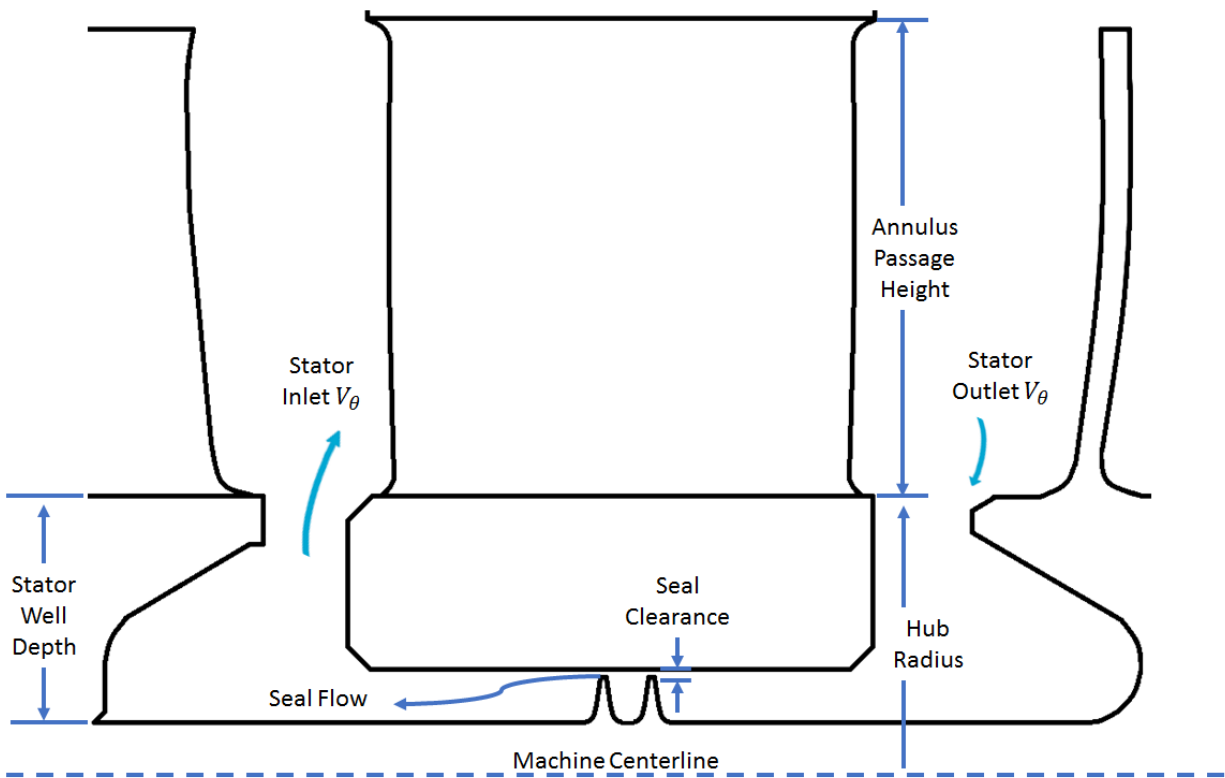


Figure 1.2: Typical cavity parameters.

Wellborn and Okiishi (1999) performed experiments on a low-speed multistage axial-flow compressor to assess the effects of shrouded stator cavity flows on aerodynamic performance. Their experiments showed that increasing seal clearance increased mass flow recirculating through the seal cavity. Similarly, Heidegger et al. (1997) computationally analyzed the 8th stage stator seal cavity of a 10-stage compressor with an aggressive pressure ratio. Heidegger's seal clearance study showed that the increase in leakage mass flow rate through the cavity with increasing seal clearance was approximately linear for a geometric configuration of a relatively large radius where annular area varied approximately with the seal clearance. Heidegger also varied the stator well depth in the cavity geometry but found that the cavity depth had no influence on the leakage flow characteristics.

1.2.2 Interactions with Primary Flow

The pressure differential across the stators and the rotor drum speeds will continue to rise as axial compressor designers continue to pursue more aggressive designs, leading to adverse flow conditions and increased leakage through the cavity. Over the years, research has confirmed that shrouded stator cavity flows can have a significant impact on the performance of multistage axial-flow compressors. Wellborn and Okiishi (1999) showed in a low-speed multistage compressor that efficiency can be degraded 1 point for every 1 percent increase in the seal-tooth clearance-to-span ratio. Moreover, the seal teeth hold very small clearance, which increases due to operational wear and, in turn, results in increased leakage flow through the cavity. Such flows induce additional aerodynamic losses by mixing with the primary flow at the stator blade hub.

For instance, the leakage flow inside the cavity consists of low momentum fluid which gets entrained in to the primary flow upstream of the stator and causes excessive near-hub blockage adversely affecting the compressor performance (Wellborn, 1999). The cross-passage pressure gradient also drives this low momentum fluid to the stator suction side. Consequently, when low momentum fluid collects near the hub, the suction side boundary layer deteriorates due to the hub corner separation, possibly leading to hub corner stall, flow blockage and higher total pressure loss.

Demargne and Longley (2000) performed experiments on a linear cascade with a slot machined along the hub upstream of the stator leading edge. By controlling the amount of leakage flow re-entering the primary passage, the performance of the blade row was observed to become

largely insensitive to the amount of leakage flow as the circumferential velocity of the leakage flow approached wheel speed. Rotational speed was also found to be another parameter influencing the circumferential velocity. The increase in rotational speed showed increase in circumferential velocity, suggesting that cavity flows at part-speed might differ from those near design speed. More importantly, the data showed that as exit flow angles increased, the change in circumferential velocity decreased. Therefore, the main parameters dictating the interaction of cavity leakage and primary flows are thought to be the leakage mass flow rate and circumferential velocity of the leakage flow.

1.2.3 Cavity Flow Structure

To optimize the near-hub stator performance and minimize the detrimental effects of interactions between the cavity leakage flow and primary flow, the flow structure within the cavity must be thoroughly analyzed. Although becoming increasingly important, the literature on details of the characteristics of cavity leakage flow near the cavity and primary flow interface, or the flow path and vortical structures within the cavity geometry is scarce because majority of the investigations are carried out using linear cascades that lack the presence of the inlet and outlet cavity wells.

Wellborn (2001) experimentally and numerically investigated cavity geometry in a low-speed axial-flow compressor and found vortical flow structures near the inlet and outlet cavity interfaces. The study revealed that the majority of the flow entered or exited the cavity near the downstream face of the inlet and outlet cavity interfaces, respectively. Heidegger's (1997) numerical investigation revealed that the hub region blockage created by the seal cavity vortical flow shifted the radial profiles higher, up to 5 percent at the leading edge in the highest seal cavity mass flow rate case. Demargne and Longley's (2000) linear cascade experiment revealed vortical flow structures at the cavity interface at low leakage fractions but disappear at leakage fractions greater than 0.66 percent. These vortical structures were found to play an important part in the exchange of fluid and flow properties between cavity and the primary passage at low leakage fractions.

These vortical structures are thought to be a general feature of flow at the inlet and outlet cavity interfaces. While these papers present some details of the vortical flow structure near the hub-cavity interface, no known literature addresses the mechanisms that generate these vortical

flow structures because the inlet and outlet cavity wells are not included in the investigations. More importantly, how these vortical flow structures change in shape or size and how they affect the path of the cavity leakage flow with changes in seal clearance is largely unaddressed. Therefore, comparing cavity flow structure, not just at the hub-cavity interface, but also in the cavity wells across seal clearances allows for a deeper understanding of the characteristics that cause additional losses when mixing with the primary flow path at re-entry to the stator inlet.

1.3 Windage Effects

1.3.1 Cavity Heating

Generally, literature regarding aerodynamic performance does not include many details concerning temperature variations through the cavity, let alone the cavity wells, because majority of the models used for analysis are adiabatic in nature. In addition to primary flow aerodynamic degradation near the hub, cavity leakage flow controls under-platform heating, which is an important mechanical design consideration for component life and high metal temperatures. Under-platform and cooling flows have been studied extensively in turbines but have now become important in compressors as designers pursue aggressive designs to operate compressors at higher speeds while still using economical materials. Moreover, higher operating pressure ratios lead to higher temperatures making thermal analysis of the components important. As the leakage flow drives through the cavity geometry, shearing work is done on the flow between the rotating and stationary wells of the cavity. This shear work causes a rise in temperature of the fluid inside the cavity known as windage heating. Therefore, the flow affected by windage must be purged or ventilated by allowing some air, driven by the pressure gradient across the stage, to enter the inlet well and flow through the labyrinth seal into the outlet well to emerge back into the primary flow.

Ozturk et al. (1998) numerically investigated leakage flow and windage generation within an axial compressor stator well. The authors reported highest temperatures at the rotor drum surface. Moreover, the temperature increases were observed at the throttling regions of the labyrinth seal and decrease after throttling, stating that the labyrinth seal tips are subjected to heating and thermal stresses. The reduction of leakage through the cavity was also explored in this study. Here, a circumferential ring or ledge was added to the downstream rotor surface within the well, which resulted in a 9 percent reduction in mass flow through the labyrinth seal and a 9 percent

reduction in the windage heating. Most importantly, this study revealed that too little flow through the cavity results in high air temperatures which, in turn, produces high metal temperatures and reduces component fatigue life.

Moreover, this viscous drag on rotating component, i.e., the windage effect, depicts both a direct loss of power from the cycle as well as an input of energy in the form of heat into the system causing the effect of windage on performance to be compounding. As mentioned in the previous section, there must exist a clearance between the stator landing and seal teeth to avert any type of failure or damage. This rise in temperature due to windage heating and higher compressor speeds would both contribute towards thermal and centrifugal growth of the seal teeth which, in turn, would have a significant impact on the leakage characteristics of the labyrinth seals.

1.3.2 Re-ingestion of Hot Fluid

The majority of the recirculating leakage flow exiting the cavity upstream of the stator dwells near the hub. Ozturk's (1998) numerical study of leakage flow within an axial compressor stator cavity showed that the air that has passed through the well, i.e., undergone a temperature rise due to windage heating, mixed with the primary passage flow and raised the near-hub temperature. The authors showed that as the flow progressed through the stator blade row, the temperature near the hub remained high, adding weight to the possibility of re-ingestion of hot fluid for further windage heating. Bayley and Childs' (1994) investigations revealed additional peak temperature rises of up to 30 °C with lower circulation rates for tight clearance case, further postulating the possibility of re-ingestion. Therefore, re-ingestion could intensify the windage and the stator cavity well heating problem. In severe circumstances, continued recirculation could lead to cavity temperatures rising continuously to high levels. Although, there is no known literature addressing re-ingestion because majority of the thermomechanical research has been performed on standalone labyrinth seals or linear cascade models that do not couple the stator passage with the cavity. Therefore, investigating the possibility of re-ingestion in a coupled stator cavity analysis and correlating re-ingestion with the corresponding seal clearance and leakage flow rate is important and is explored in this study.

1.3.3 Interdependence of Leakage Flow and Windage Heating

Aerodynamic considerations of cavity flow suggest that labyrinth seal teeth and cavity geometry should be required to minimize gas recirculation through the cavity (Wellborn, 1996). The majority of the literature predicts that the emerging flow from an outlet well will reduce the compressor stage performance (Wellborn, 1996 and Heidegger et al., 1996). On the contrary, thermo-mechanical considerations of the cavity suggests that too little flow through the cavity will result in high air temperature which, in turn, produce high metal temperature and reduce component fatigue life. In engine experimental or coupled stator-cavity numerical investigations of windage heating of air passing through a labyrinth seal cavity are quite scarce in the open literature. Although, albeit few, there are articles that investigate standalone labyrinth seals.

Waschka et al. (1992) obtained heat transfer and leakage loss measurements for compressible flows in a standalone straight-through labyrinth seals test section at high rotational speeds. This study found large decreases in leakage flow rates at higher rotational speeds. The authors also revealed an upper limit of the leakage flow rate due to rotational effects, with the upper limit increasing with larger seal clearances. Moreover, the results showed an increase in circumferential velocity lead to a decrease in leakage rate and increased heat transfer. Most importantly, the local heat flux was observed to be the highest at labyrinth seal teeth.

Millward and Edwards (1996) reported experimental results in a standalone test section accommodating various stepped and straight-through labyrinth seal geometries. This study revealed that a clear relationship exists between windage heating and leakage flow, which is largely independent of clearance over the range tested. More importantly, windage heating increased exponentially with increasing rotational speeds. The authors also showed a decrease in leakage flow rate with increasing number of labyrinth seal teeth. Denecke et al. (2005) numerically investigated a parametric study of an inclined labyrinth seal geometry with an inlet and outlet duct to analyze the total temperature rise and circumferential velocity development across the rotating seals. This study, like Millward and Edwards', showed an increase in windage heating at higher rotational speeds. Moreover, the results revealed that windage heating increases with increasing number of labyrinth seal teeth. Most importantly, the author reported that both inlet and outlet circumferential velocity can significantly affect windage heating. A higher inlet circumferential velocity leads to higher outlet circumferential velocity and less windage heating.

Li et al. (2006) numerically investigates a straight-through labyrinth seal geometry with seven teeth and found that the reduction of leakage flow rate would depend on the ratio of circumferential velocity to axial velocity. The authors observed that when this ratio was greater than 5, leakage flow reductions of more than 20 percent were observed. These examples illustrate that the seal leakage, circumferential velocity development, and windage heating in the labyrinth seal have strong interdependency. Nevertheless, all these studies involve a standalone labyrinth seals with inlet and outlet ducts used to feed airflow at relevant operating conditions. While these investigations reveal flow and windage characteristics in a standalone labyrinth seal, this work is unique in the sense that it accounts for the inlet and outlet cavity wells inside a coupled stator-cavity model to numerically investigate the development of windage heating as the leakage flow passes through the cavity. The inlet and outlet rotating cavity wells and the long rotating walls set the compressor stator labyrinth seal apart from a regular labyrinth seal. These conditions determine the sealing characteristics of the labyrinth seals in a compressor stator well. Therefore, investigating the labyrinth seal characteristics with the rotating inlet and outlet cavity wells in a coupled stator-cavity model would reveal more representative results regarding the compressor cavity performance.

1.4 Research Objectives

Although becoming increasingly important, very few papers have detailed the structure of compressor cavity flows in the stator wells and how the cavity wells affects the leakage flow path as well as the windage heating. Majority of the open literature presents limited details about only a portion of the cavity flow phenomenon making it difficult to understand the interdependence of flow parameters and thus, lacks a wholesome understanding of the cavity flow and the windage heating effect. The flow in shrouded stator cavities can be quite complex with axial, radial, and circumferential variations. These complexities are in addition to other expected cavity flow characteristics such as leakage due to seal clearance, temperature increases due to windage, and circumferential velocity changes due to momentum transfer and shear work. Therefore, including the stator cavity wells in a coupled stator cavity investigation provides a more accurate representation of the influence of cavity leakage flow.

This work consists of a series of numerical simulations aimed at determining the effects associated with cavity leakage flows, in particular that of the flow field within the cavity and its

interdependence with windage heating. Instead of analyzing flow structure near the hub-cavity interface or windage heating in a standalone labyrinth seal geometry, this study numerically investigates a coupled stator-cavity model with a cavity that possess labyrinth seals and the rotating wells to better represent compressor geometry and conditions. Shrouded stator cavity is analyzed using 3D CFD for the 1st stage cavity in the Purdue 3-Stage Axial Compressor (P3S) model. A parametric model is created for the stator cavity which allows for variation in seal-teeth clearance. A sensitivity analysis is performed by varying the seal clearance to understand and quantify the impact of varying clearance on compressor performance and windage heating.

Therefore, the principal objective of this work is to characterize the interdependence of parameters such as a cavity leakage flow, circumferential velocity development, windage heating, etc. by investigating the flow structure details in the cavity wells and understanding the flow path of the cavity leakage fluid through the cavity as well as through the primary passage. Analysis of the results will reveal the mechanisms through which cavity leakage flows affect the stator passage aerodynamics as well as the windage heating within the cavity, both regarding their bulk effect on the compressor performance and regarding the details of the flow path within the cavity wells. In turn, this understanding of the mechanism involved will provide insight into how these cavity leakage flow effects might influence the design considerations for optimizing stator passage aerodynamics as well as minimizing stator cavity heating. More importantly, the data and trends will give aerodynamic, mechanical, and secondary flow system designers an indication of the complexities of the flows within shrouded stator cavities and provide them a comparison datum for other more complex geometries and flow conditions as well.

CHAPTER 2. CONFIGURATION DETAILS

2.1 Experimental Configurations

To investigate the effects of cavity leakage flow and windage heating, the ANSYS CFX solver is used as the primary CFD simulation tool. A parametric model of the Purdue 3-Stage Compressor Facility (P3S) is used to allow for rapid geometric modifications to the seal clearance in a coupled stator and cavity system. Measurements performed by the previous investigators on the P3S facility provide the initial and boundary conditions for the parametric model. Moreover, these in-compressor measurements also act as a datum for comparison of the primary passage flow characteristics and the overall performance of the compressor. Therefore, the following sections describe the ANSYS CFX Solver, the details about the P3S Compressor Facility and the stator cavity geometry, as well as the resembling parametric model used for investigations in this work.

2.1.1 Facility Overview and Compressor Test Section

The investigations presented in this work were performed on a parametric CFD model that replicates the P3S Research Facility. The P3S is an open circuit facility, shown in Figure 2.1. While multiple compressor configurations can be integrated in the P3S Compressor facility, this work was conducted on the PAX100 geometry, which models the rear stages of a Rolls Royce high-pressure compressor. More importantly, this configuration is operated at engine-representative Reynolds and Mach Numbers to depict real engine flow physics. Furthermore, the stages in this configuration are geometrically scaled up to aid in detailed flow measurements. Overall, the multistage design of the facility creates a unique opportunity to analyze an “embedded” stage and complex multistage flow effects. Such characteristics make it possible to capture boundary conditions essential for creating a high-fidelity computational model as well as provide datasets to improve the confidence in the computational models.

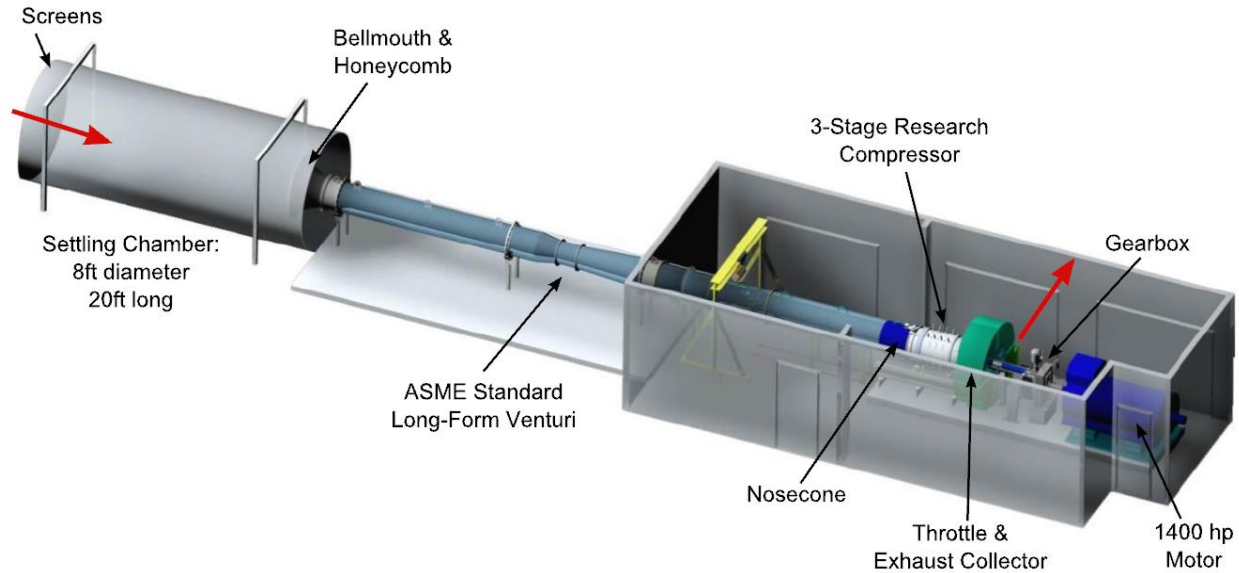


Figure 2.1: Purdue 3-Stage Axial Compressor Research Facility.

The working fluid is unconditioned, atmospheric air drawn from outside the facility. Air travels through an 8 ft. diameter screen into a 20 ft. long settling chamber, which mitigates atmospheric variations, before passing through a reducing bellmouth into a 2 ft. diameter duct. Downstream of the bellmouth, flow travels through an ASME Standard Long-Form venturi that accurately measures the compressor mass flow rate, which will be used as one of the boundary conditions in the CFD model. In all, the atmospheric air travels approximately 20 duct diameters, i.e., 40 ft., between the bellmouth and the compressor test section. As the flow reaches the compressor test section, a semi-elliptical nosecone gradually directs the flow into a constant annulus flow path, which is defined by a 2 in. primary passage height with a 2 ft. outer diameter. Lastly, once the air passes through the compressor test section, it exits outside the facility directed by a large cylindrical scroll collector. Additional details of the existing facility layout can be found in Talalayev (2011) and Ball (2013).

The flow path of the P3S PAX100 test section and the blade count is shown in Figure 2.2. Once the flow passes the nosecone, it encounters four airfoil struts. Then, the flow encounters an Inlet Guide Vane (IGV) followed by three rotor-stator stages. The rotor blade count decreases by three as flow progresses downstream: 36, 33, and 30, respectively. The IGV, Stator 1, and Stator 2 rows each have four vanes, and Stator 3 has 50 vanes. As mentioned before, the primary passage has a constant 2 in. annulus height with a 2 ft. outer diameter. The rotors and IGV are standard

double circular arc (DCA) designs, and the stators are NACA 65-series airfoils. The rotor drum constitutes three individual blade integrated disks (blisks) compressed together by two endplates mounted to the shaft. The IGV and Stators are shrouded both at the hub and tip. Consequently, there is a cavity present with the rotor blisks consisting the labyrinth seals positioned towards the center of the stator platform. Lastly, specific geometric parameters for the blading in the P3S PAX100 facility can be found in Berdanier and Key, 2015b.

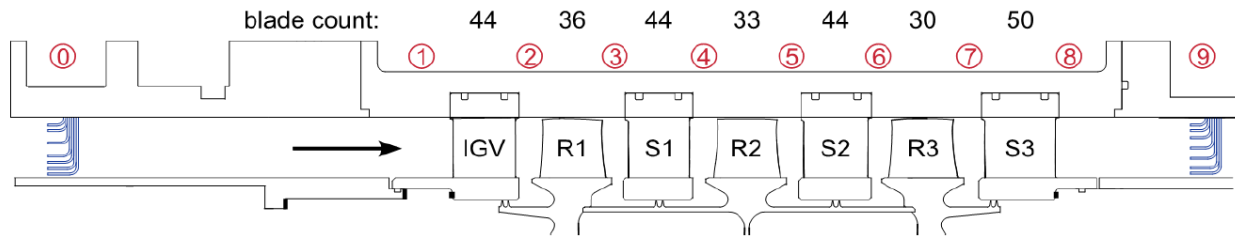


Figure 2.2: Cross Section of PAX100 Compressor Flow Path, Axial Location of Instrumentations, and Individual Blade counts.

Along with the P3S flow path geometry specifications, additional relevant parameters are also required to accurately build a computational model. Namely, the static labyrinth seal clearance under the stator platform were designed for cold values of: 0.019 in. for the IGV, 0.02 in. for Stator 1 and Stator 2, and 0.019 in. for Stator 3. However, currently measured cold values are: 0.022 in. for the IGV, 0.035 in. for Stator 1, 0.037 in. for Stator 2, and 0.024 in. for Stator 3. Operating “hot” clearance for these seals have not been measured. Both, design and measured, cold values are taken into consideration while designing the parametric study. Moreover, all the stator vanes have a 3/32 in. fillet radius at both the hub and shroud end walls, while the rotors have a fillet radius of 0.15 in. at the hub. The rotor blades have an elliptically shaped leading edge, while the stator have circular leading edges. A past analysis used an optical scan to compare the design intent geometry of the rotor blisks with the manufactured geometry and confirmed all dimensions to be within specified design tolerances making these geometry parameters valid for use while building the CFD model. Lastly, the operating rotor tip clearances have also been measured during experiments. Since a nominal 1.5 percent tip clearance (0.03 in.) height as a fraction of total span represents the baseline compressor configuration, the average operating tip clearance from the experimental data is used while developing the rotors in the CFD model.

2.1.2 Steady Compressor Performance Measurements and Instrumentation

2.1.2.1 Primary Passage

A compressor performance map is used to define the performance characteristics and compressor operating point, as shown in Figure 2.3. Here, the rotational speed and the mass flow rate can be utilized to describe the compressor performance, characterized by the total pressure ratio (TPR) achieved by the compressor. Since both parameters can be affected due to changes in ambient temperature, pressure and humidity, they must be corrected to standard day conditions to consider fluctuations in inlet conditions. This promotes a proper comparison with other experimental and computational data ensuring consistency in performance measurements attained regardless of inlet conditions. Hence, the boundary conditions obtained from previous experiments are corrected to standard day conditions before incorporating them in the CFD model. The corrected rotational speed is determined by

$$N_c = \frac{N_{mech}}{a_{o,act}/a_{o,ref}}, \quad (2.1)$$

where N is the rotational speed in rpm and a is the speed of sound, while the correct mass flow rate is determined by

$$\dot{m}_c = \dot{m}_{act} \left(\frac{\rho_{a,ref} a_{o,ref}}{\rho_{a,act} a_{o,ref}} \right), \quad (2.2)$$

where \dot{m} is the mass flow rate and ρ is the density of air. Moreover, the P3S compressor is driven from the rear by a 1400 HP AC motor and controlled by a liquid-cooled variable frequency driven (VFD) with a magnetic encoder located on the motor shaft providing feedback to maintain shaft speed within 0.01 percent of the desired speed, thereby allowing a consistent rotational speed and allowing the resulting passage flow field a direct comparison when validating CFD simulations at the same speed. For the P3S compressor, the conditions used to calculate the corrected speed and corrected mass flow rate were measured at the Aerodynamic Interface plane (AIP), designated axial location zero in the flow path shown in Figure 2.2. Here, bulk thermodynamic properties are calculated using measurements from a mid-span element of a total pressure and total temperature rake. In addition to these rakes at the AIP, 13 circumferentially-distributed static pressure taps at the outer diameter of the flow path at axial location zero had been incorporated to establish circumferentially uniform pressure and temperatures of the incoming flow, as measured by Ball (2013). Therefore, great care had been incorporated by previous investigators to measure detailed boundary conditions essential for the computational analysis.

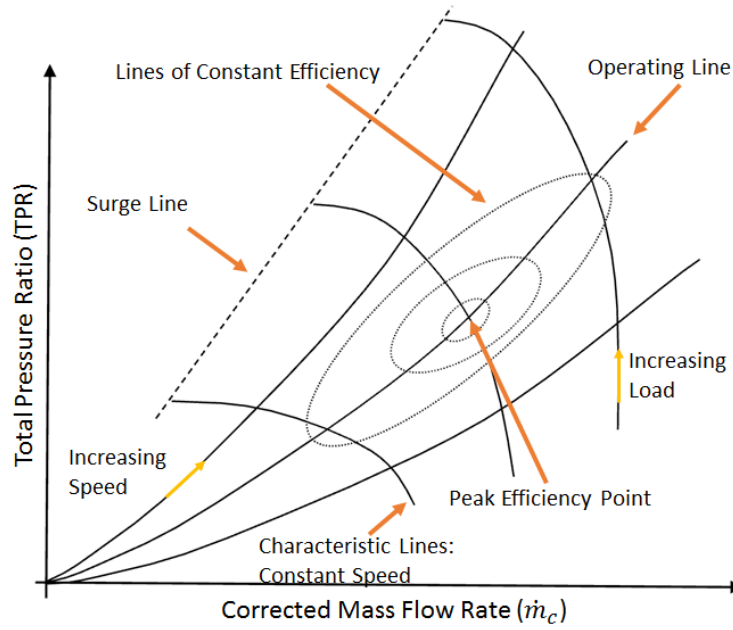


Figure 2.3: Generic Compressor Map.

Furthermore, the seven-element Kiel-head total pressure and total temperature rakes located at each of the axial positions, labeled in Figure 2.2, allowed measurements before and after each blade row. The combination of measurements at positions 1 through 9 provided the opportunity to define the overall compressor performance and relative performance of each individual blade row. The labeled stations in Figure 2.2 are axially midway between the blade rows based on the mid-span geometry. Most importantly, the seven elements of each rakes are radially biased towards the hub and tip to grant increased resolution in regions where secondary flows are significant. The radial locations of probes are summarized in Table 2.1. Additionally, IGV and stators are all independently traversable in the circumferential direction for two stator passages to capture pitchwise data. To further improve spatial resolution and attain a more thorough distribution of measurements closer to the end walls, a miniature Kiel head total pressure probes was traversed in small radial increments downstream of each of the stator vane rows. Additionally, hot-wire anemometry was used to further understand the flow field in the primary passage by obtaining velocity and flow angle measurements throughout the compressor for axial locations 2 through 8. These detailed total pressure, velocity, and flow angle measurements enable the comparison of the stator exit flow field. Details about the instrumentations can be found in Berdanier and Key (2015b).

Table 2.1: Radial Distributions of rake element locations.

Axial Pos.	Total Pressure [% annulus height]							Total Temperature [% annulus height]						
0	12	20	30	40	60	80	88	12	20	35	50	70	80	88
1-8	12	20	35	50	70	80	88	12	20	35	50	70	80	88
9	12	20	35	50	65	80	88	12	20	30	50	70	80	88

In addition to the flow measurements, the outer surface of the casing over each blade row holds a series of surface-mounted thermocouples to generate temperature distribution in the axial direction. These measurements will be applied to the CFD model for the implementation of isothermal boundary condition, instead of an adiabatic boundary condition. Another parameter to consider at the shroud is an accurate representation of the rotor blade tip geometry in the CFD model. The operating rotor tip clearances were measured using capacitance probes and details about the instrumentation can be found in Berdanier and Key (2015b).

2.1.2.2 Stator Cavity

As discussed in the previous chapter, the differential pressure across the stators will cause flow to recirculate upstream through the cavity. The flow path for the cavity leakage flow is displayed in Figure 2.4. Since the focus of this work is the stator 1 cavity, the stator 2 cavity will not be discussed in detail. For reference, Stator 2 geometry is a mirror image about the vertical axis for the PAX100 configuration. Nevertheless, stator 2 cavity will be modeled with the same accuracy as stator 1 in the CFD model to ensure any information propagating upstream or downstream due to the cavities is captured in the model and can be utilized in the future. Measurements near the labyrinth seals had also been acquired by previous investigators with the intention to determine boundary conditions of the flow through the labyrinth seals in the shrouded stator cavity. Therefore, pressure data were available both upstream and downstream of the two seals with the axial position of the sensors displayed in Figure 2.4.

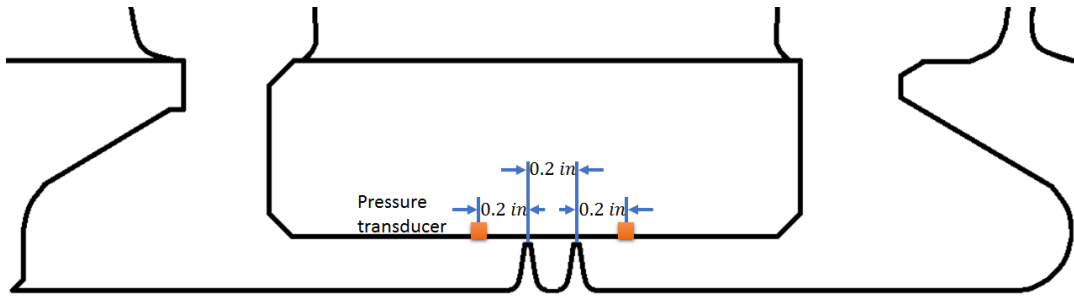


Figure 2.4: Stator 1 Cavity Geometry along with sensor locations.

The flow path in the IGV and stator 3 cavities is different. The air path is sealed at the inlet of the compressor, but a leakage path exists under the Stator 3 labyrinth seals to atmospheric pressure. Therefore, to sufficiently define boundary conditions for the CFD model, the S3 cavity leakage flow rate assessed by previous investigators was used. Ball (2013) considered the stator 3 leakage flow for computational models and concluded that whether the Stator 3 seal flow could exit to ambient pressure, or if the leakage on flow path was plugged, the effect on overall compressor pressure rise was negligible. Nevertheless, due to localized heating of the components in the rear of the compressor, a measurable change in the overall compressor efficiency was noticed. Hence, four tubes in the rear of the compressor had been used to capture the leakage flow for determining the boundary conditions to adequately model the Stator 3 cavity. A schematic of the stator 3 cavity is shown in Figure 2.5.

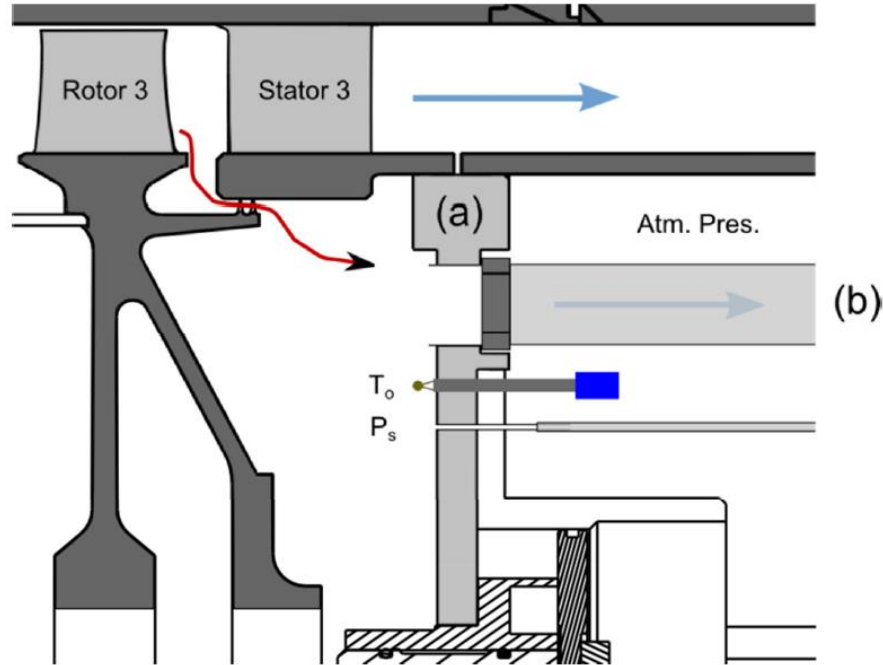


Figure 2.5: Stator 3 Leakage Flow Path and manifold tubes from (a) the rear bearing plate to (b) an orifice plate run from Brossman (2012).

2.1.3 Compressor Operating Conditions and Dataset Selection

Compressor performance data were collected at four corrected operating speeds (100%, 90%, 80%, and 69%). The procedure outlined in Section 2.1.2.1 was used to determine the corrected speed and corrected mass flow. The 100% N_c Speedline is displayed in Figure 2.6 with the four operating points labeled for discussion in this section: a low loading (LL) condition which describes a high flow rate, negative incidence condition; a nominal loading (NL) condition which describes operating conditions with a mass flow rate higher than the peak efficiency point; a peak efficiency (PE) point; and a high loading (HL) condition which describes a low flow rate, high incidence condition. Additional details about the benchmark compressor map data can be found in Berdanier and Key (2015b).

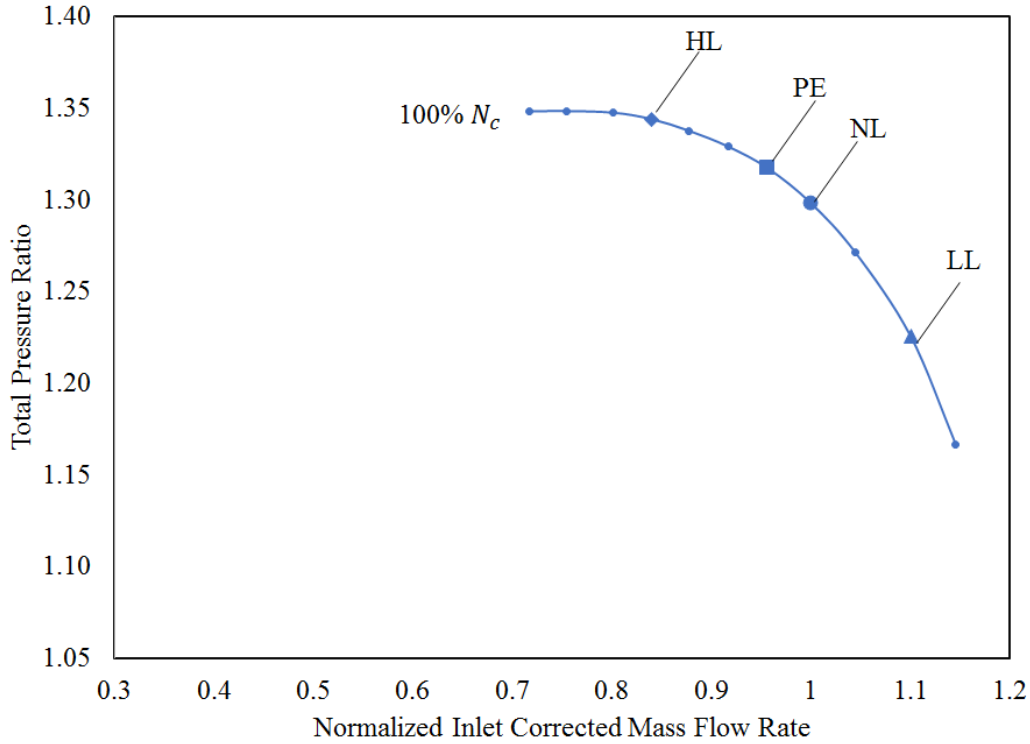


Figure 2.6: Compressor Map with 100% N_c Speedline.

Detailed velocity, flow angle, and total pressure data are available in the primary passage at NL, and this condition is the focus of this CFD work since the flow field at HL has significant boundary layer separation.

2.2 Numerical Configurations

Computational Fluid Dynamics (CFD) is a computer-based tool for simulating the behavior of systems concerning fluid flow, heat transfer, and other similar physical processes. CFD tools solve the set of Navier-Stokes equations which are partial differential equations with no known general analytical solution but can be discretized and solved numerically to characterize the systems involving momentum, and heat and mass transfer. The commercially available tool ANSYS CFX is utilized in this study for investigations.

CFX is based on the most common solution method for the Navier-Stokes equation known as the finite volume method. In this technique, the region of interest is divided into small control volumes, and the equations are discretized and solved iteratively for each control volume resulting in the approximation of the value of each variable at specific points throughout the domain. The

ANSYS CFX Solver is a node centered pressure-based fully implicit finite volume code. A node centered code stores all numerical values and properties at the nodes and control volumes are formed around these nodes. Generally, a fully implicit finite volume method results in a linear system of the Navier-Stokes equations corresponding to each control volume. The CFX Solver solves this linear system of discretized equations using a multigrid accelerated Incomplete Lower Upper (ILU) factorization technique, details of which are available in the documentation provided by ANSYS (CFX Solver Theory Guide, 2018). Therefore, the CFX Solver will iteratively solve the equations, while grid generation tools, ANSYS TurboGrid and ANSYS Meshing, are used for discretizing the P3S PAX100 domain and cavity domains, respectively.

ANSYS TurboGrid is preferred for the primary passage and blades because its grid generation algorithm is specifically tailored to rotating machinery for creating high-quality hexahedral meshes while preserving the underlying geometry. First, the geometry is imported using three .curve files: the hub, blade cross-sections, and the shroud. These .curve files contain the geometry definition in the form of 3D cartesian or cylindrical coordinates. Then, the mesh is generated on the imported geometry using a 2D stacking of the mesh topology at various spanwise locations. Here, a global size factor and a boundary layer refinement value (y^+) along with the 2D stacked topology are used to generate the 3D mesh of the primary passage. Therefore, the mesh generated by TurboGrid can be used in the CFX solver to solve complex blade passage flow physics.

On the other hand, since TurboGrid is specifically tailored to rotating machinery with blades, it does not have the ability to discretize the cavity domain. Since ANSYS Meshing is a more general tool for mesh generation, the cavity domain is discretized using ANSYS meshing. Nevertheless, the cavity mesh is also discretized with hexahedral meshes to enable consistent discretization domains and a similar approach of a size factor and boundary layer refinement is used for mesh generation. While the discretized geometry is presented in the grid convergence analysis section of this chapter, details about these three commercial ANSYS tools can be found in the documentation provided by ANSYS (CFX Reference Guide, 2018; CFX Solver Theory Guide, 2018; Meshing Users Guide, 2018; TurboGrid Users Guide, 2018).

2.2.1 Main Passage Model

2.2.1.1 Discretization and Boundary Conditions

The first configuration of the CFD model consists of the primary passage, as described in Figure 2.3. Figure 2.7 represents the geometric model in TurboGrid before the domain is discretized. First, one of the four front struts are modeled to ensure the IGV receives any of the small flow disturbances that might be present. While the front strut does not cause any major flow disturbances, adding the front strut allows for properly applying isothermal wall boundary conditions at the shroud, which are discussed at the end of this section. The experimental data from instrumentation station 1, directly in front of the IGV, is used to ensure the non-intrusive nature of the front strut by examining the radial total pressure and total temperature profiles ahead of the IGV. The front strut is followed by one passage of each blade row from IGV to Stator 3. The model is constructed based on the parameters discussed in section 2.1.1 along with information about the end wall fillets and tip clearances. The TurboGrid mesh generation method discussed above is used for hexahedral grid generation by defining the grid cell count in the radial, axial, and circumferential directions and scaling them using the global size factor. Details about the generated grid are discussed in the grid resolution analysis section.

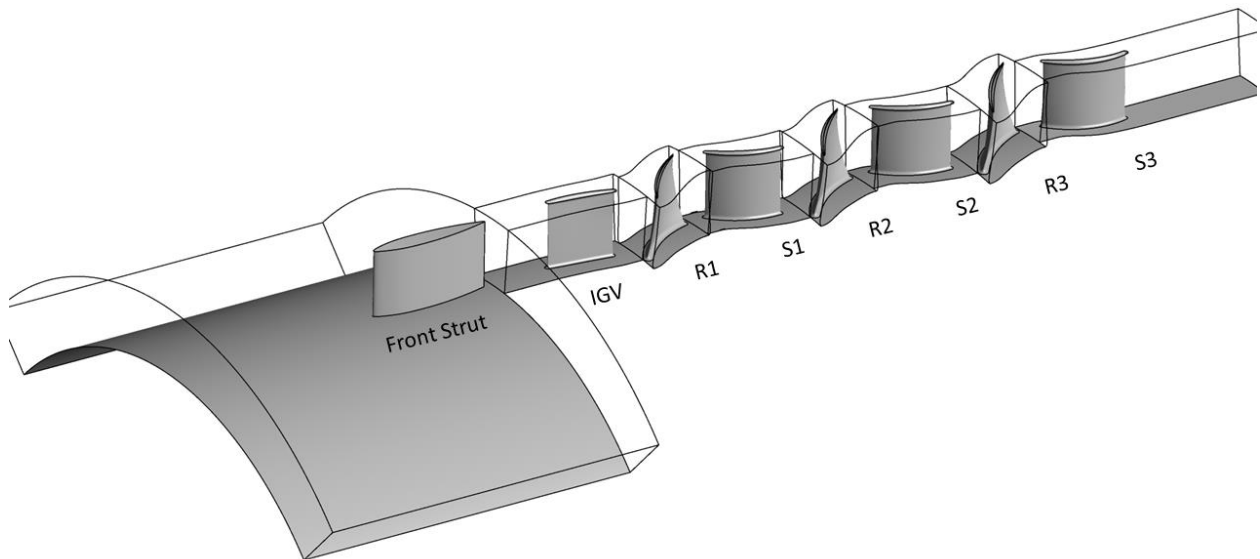


Figure 2.7: Geometric Model prior to model discretization.

Once the domains are discretized, the grids are imported to the ANSYS CFX-Pre for defining boundary conditions, interfaces, and physics models for simulation. While several combinations of boundary conditions are available, the best practice for turbomachinery boundary conditions is to specify the total pressure and total temperature at the inlet and either the mass flow rate, the exit corrected mass flow rate, or the static pressure at the outlet. The availability of detailed total pressure and total temperature profiles from the AIP as well as the corrected mass flow rate information allows the model to calculate the flow based on similar conditions experienced in the experiments. Therefore, total pressure and total temperature profiles are applied as boundary conditions to the inlet of the front strut domain, shown in Figure 2.8, and exit corrected mass flow, for the NL condition, is applied to the exit plane of stator 3. Lastly, the hub and blades are modeled as no slip, smooth, and adiabatic walls. The shroud walls are treated as isothermal walls to increase accuracy of temperature results in the model. The temperatures for the shroud walls of each station are summarized in Table 2.2. To reconcile shroud temperatures from the casing temperature measurements, 1D heat transfer was calculated using energy balance as described in:

$$H(T_{cas} - T_{\infty}) = \frac{k(T_s - T_{cas})}{L}, \quad (2.3)$$

where h is the convective heat transfer coefficient of air, k is the thermal conductivity of the casing, L is the casing thickness, and T_{cas} , T_{∞} , T_s are casing, ambient, and shroud temperatures, respectively. Although, no significant temperature difference between the casing and shroud was observed for any of the measurement stations. Therefore, casing temperature were directly applied to the isothermal shroud walls as boundary conditions in the model. Lastly, the stators are in the stationary domain while the rotors are in the rotating domain with a rotational speed of 5000 rpm to match the compressor map conditions at 100%Nc.

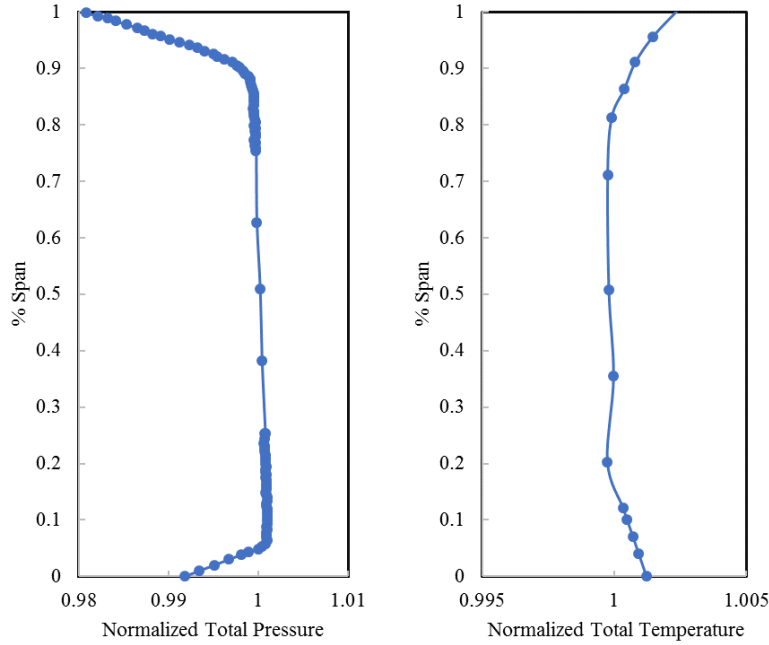


Figure 2.8: Total Pressure and Total Temperature boundary conditions acquired from AIP measurements.

Table 2.2: Casing Temperature for isothermal shroud wall boundary conditions.

Station	FS	IGV	R1	S1	R2	S2	R3	S3
Normalized T_o	1.0083	1.0191	1.0253	1.0342	1.0460	1.0584	1.0693	1.0756

2.2.1.2 Domain Interfaces

Simulations whose characteristics do not change with time and whose steady conditions are assumed to have been reached after a relatively long-time interval are defined as Steady-State simulations. Transient simulations, on the other hand, require information to determine the time intervals for flow field calculations. Transient simulations are generally caused by initially changing boundary conditions at start up or by some inherently unsteady flow characteristics, such that steady-state conditions are never reached, even though all flow conditions are unchanging. To predict such unsteady phenomena that occur because of interaction between adjacent blade rows, blade flutter, or boundary disturbances can be computationally expensive. Moreover, it can be expensive to include more than a few passages per blade row to capture these phenomena

accurately. For many turbomachinery problems, steady-state stage simulations are sufficient to obtain machine performance and analyze flow details.

Therefore, this study utilizes a steady-state solution of one passage per blade row. However, steady-state stage simulations require models to convey information between adjacent blade rows due to changes in the rotation frame, pitch angle, and non-matching grids of the domain. ANSYS CFX defines this connection as a general connection, as shown in Figure 2.9. At a general connection, there are two major frame change/mixing models for steady-state simulations: Frozen Rotor and Stage Mixing Plane. The Frozen Rotor model, as the name suggests, assumes a fixed relative orientation of the components across the interface (ANSYS CFX-Solver Theory Guide, 2018). Therefore, the frame of reference and pitch are changed but the variations in fluxes are largely ignored as the frozen rotor model only takes a snapshot of the flow and largely ignoring circumferential variations. On the other hand, the Stage Mixing Plane model performs a circumferential averaging of the fluxes instead of assuming a fixed relative position, thus enabling the steady-state predictions to be obtained for multi-stage machines by accounting for time averaged interaction effects (ANSYS CFX-Solver Theory Guide, 2018). Hence, Stage Mixing Planes are employed in this model at the inlet and exit of inter-stage domains as shown in Figure 2.10. Moreover, since only one passage needs to be modeled for this investigation, the circumferential walls are two sides of a periodic interface and can be mapped by a single rotational transformation about the rotational axis. This is achieved by using the Rotational Periodicity interfaces, also shown in Figure 2.11.

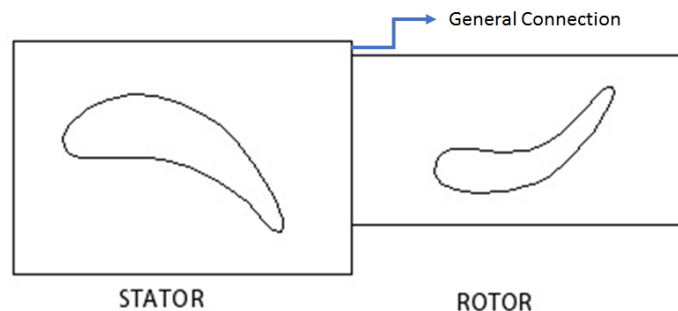


Figure 2.9: A general connection representing Frame Change and Pitch Change Across a stator and a rotor.

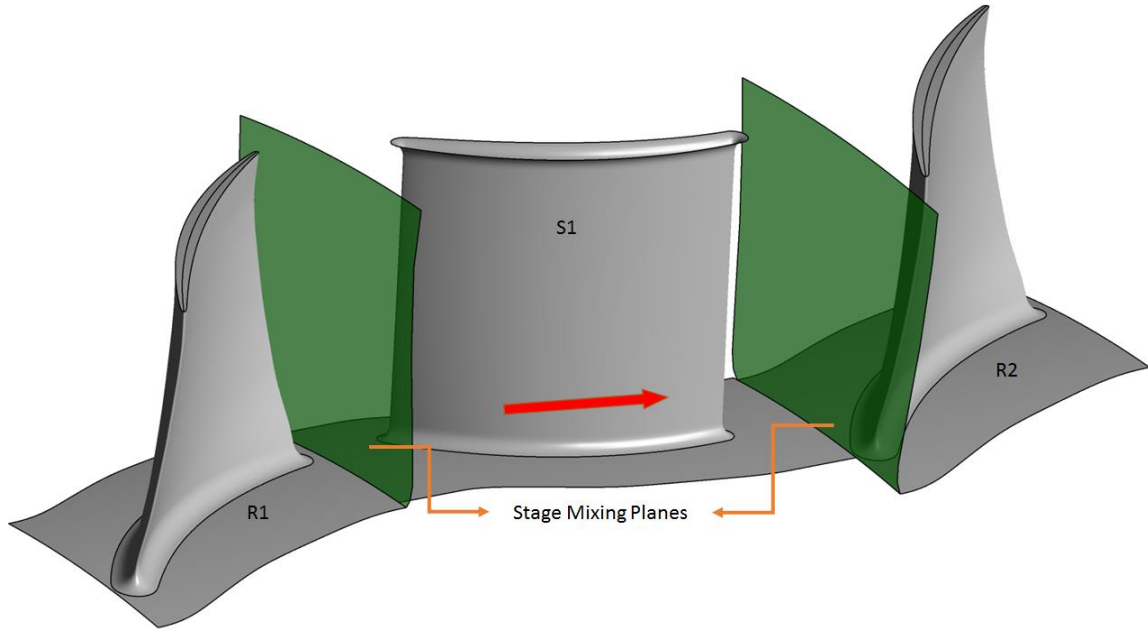


Figure 2.10: Primary Passage model highlighting stage-mixing planes.

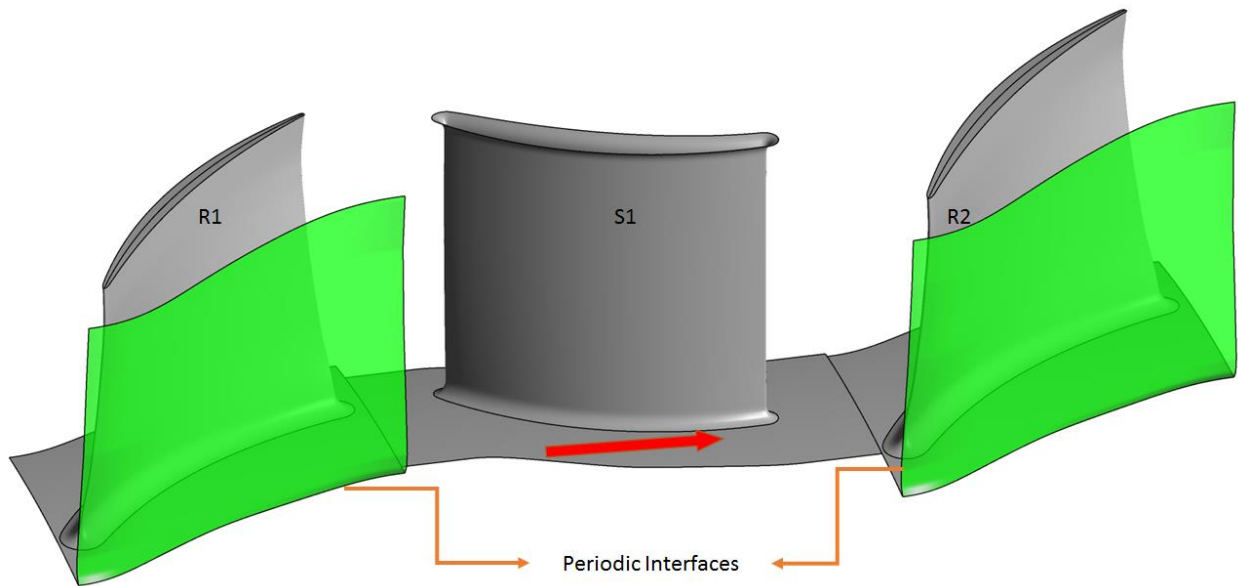


Figure 2.11: Primary Passage model highlighting periodic interfaces.

2.2.1.3 Physics Solver Criteria

Now that the domain is fully defined, the form of the governing equations, turbulence models, and advection scheme are selected. ANSYS CFX solves the set of unsteady Navier-Stokes equations in their conservation form. The continuity equation is described as:

$$\frac{\partial \rho}{\partial t} + \nabla \cdot (\rho \mathbf{U}) = 0 \quad (2.4)$$

where ρ is the density of the fluid, t is the time, and \mathbf{U} is the velocity vector. The momentum equation is described as:

$$\frac{\partial(\rho \mathbf{U})}{\partial t} + \nabla \cdot (\rho \mathbf{U} \otimes \mathbf{U}) = -\nabla p + \nabla \cdot \boldsymbol{\tau} + \mathbf{S}_M \quad (2.5)$$

where p is the pressure, \mathbf{S}_M is the momentum source term, and $\boldsymbol{\tau}$ is the shear stress tensor which is described as

$$\boldsymbol{\tau} = \mu \left(\nabla \mathbf{U} + (\nabla \mathbf{U})^T - \frac{2}{3} \delta \nabla \cdot \mathbf{U} \right) \quad (2.6)$$

where μ is the dynamic viscosity of the fluid, T is the mathematical transpose operator, and δ is the identity matrix. Lastly, the energy conservation equation is described as:

$$\frac{\partial(\rho h_{tot})}{\partial t} - \frac{\partial p}{\partial t} + \nabla \cdot (\rho \mathbf{U} h_{tot}) = \nabla \cdot (\lambda \nabla T) + \nabla \cdot (\mathbf{U} \cdot \boldsymbol{\tau}) + \mathbf{U} \cdot \mathbf{S}_M + \mathbf{S}_E \quad (2.7)$$

where λ is the thermal conductivity, \mathbf{S}_E is the energy source term, and h_{tot} is the total enthalpy which is defined as:

$$h_{tot} = h + \frac{1}{2} \mathbf{U}^2 \quad (2.8)$$

Generally, the continuity equation (Eq. 2.4) and the momentum equations (Eq. 2.5 and 2.6) are standard across solvers for instantaneous mass and momentum conservation. The energy conservation equation (Eq. 2.7 and 2.8) has various forms. For this investigation, Total Energy Equation (Eq. 2.7 and 2.8) is imposed in the CFX solver. The Total Energy Equation includes viscous work terms which represents the work due to the viscous stresses, $\nabla \cdot (\mathbf{U} \cdot \boldsymbol{\tau})$, and models the internal heating due to the viscous forces in the fluid which are significant in this investigation.

Another important criterion to consider is the turbulence model. A study performed by Flores (2014) suggests $k - \omega$ based models are generally more suitable for turbomachinery applications. ANSYS Solver Theory Guide (2018) also recommends using the Shear Stress Transport (SST) model, which is $k - \omega$ based turbulence model, for turbomachinery applications. The SST turbulence model is an eddy-viscosity turbulence model based on the well known Reynolds-averaged Navier-Stokes equations (RANS) that combines the $k - \epsilon$ and $k - \omega$ turbulence models. The $k - \epsilon$ model is used away from the wall and a blending function is used near the wall to blend the two models. To model the flow near the walls, the SST model uses an automatic near-wall treatment developed by ANSYS CFX, which allows for a smooth transition between a low turbulence Reynolds number form to a wall function formulation for

accommodating y^+ values. Scalable wall functions are used for larger y^+ values where low-Reynolds number flows do not exist. Therefore, the $k - \omega$ based Shear Stress Transport (SST) model is selected in the CFX solver due to the model's ability to account for the transport of the turbulent shear stress which results in highly accurate predictions of the onset and the amount of flow separation under adverse pressure gradients. Details about the SST model in CFX can be found in the ANSYS CFX-Solve Theory Guide (2018). Lastly, advection schemes account for the numerical mechanisms for transporting a quantity (velocity, temperature, etc.) throughout the domain. Accuracy and stability are generally the main concerns when selecting an advection scheme. Therefore, a second-order high-resolution scheme is imposed in the CFX-Solver due to its accuracy in recirculating flows, pressure drop predictions, and energy balance stability characteristics. Additional details about the CFX models can be found in CFX-Solver Theory Guide (2018).

In addition to the stability of the physics models, physical timescale is also an important factor in ensuring convergence. Generally, for turbomachinery applications a good estimate of the timestep is in the range of $0.1/\omega$ to $1/\omega$, where ω is the angular velocity of the rotor in radians per sec. For this investigation, the simulation starts with a slightly aggressive physical timestep of $0.2/\omega$, i.e., $3.8E-4$ seconds and progressively reduces to $0.025/\omega$ allowing four full rotor revolutions per timestep. Various cases were analyzed to test the impact this had on convergence. In general, starting with an aggressive timescale allows faster convergence and solution of overall flow characteristics while a conservative timescale allows for more resolution of the complex flow features. Therefore, the technique for this investigation first enables faster convergence of the overall flow and then resolves more complex flow features using a more conservative timescale. Figure 2.12 shows the progression of the physical timestep as a function of iteration number for the primary passage model. The overall comparison of this model along with the convergence of pertinent quantities will be discussed in section 2.3.3 along with Grid Refinement Study.

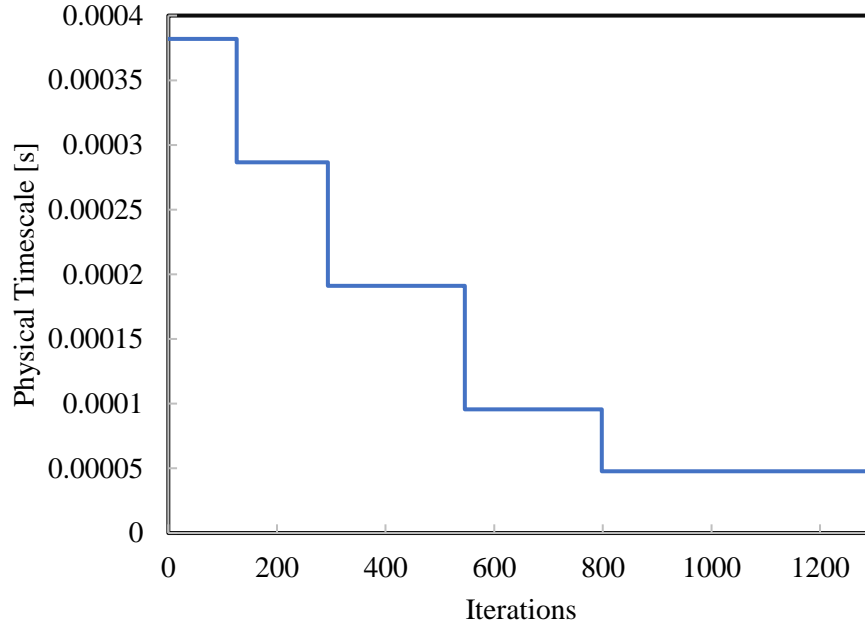


Figure 2.12: Physical Timescale scheme as a function of iterations.

2.2.2 Cavity Flow Model Development

2.2.2.1 Discretization and Boundary Conditions

The second configuration of the CFD model consists of the primary passage as well as the cavities coupled to the primary passage. A section view of the cavities in the PAX100 Configuration is displayed in Figure 2.13. Here, the stator 1 cavity geometry will be used to show the parametric capabilities of the model. As labeled in the Figure 1.1, the cavity geometry is divided primarily into three parts: rotating rotor drum wall, stationary stator landing wall, and the labyrinth seals. For the parametric model, the rotating wall as well as the stator landing are fixed to ensure that changes to the labyrinth seals do not affect the overall cavity geometry. For the labyrinth seals, all the angles and dimensions of the curves are fixed except the dimension of the labyrinth seal, which determines the height of the seals. The parametric capability of this model allows for quick changes to the labyrinth seal clearance and automatic grid generation in that region of the model for quick turnaround time without affecting the overall discretized domain.

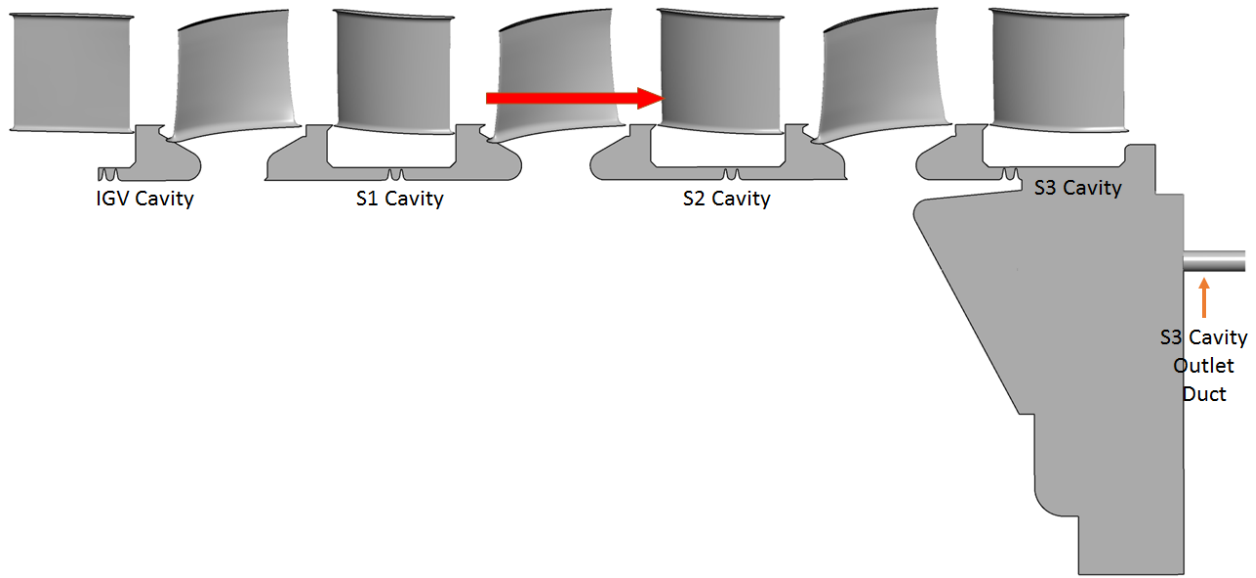


Figure 2.13: Cavities geometry cross sections in the coupled model.

These parametric cavity geometries are coupled with the IGV, Stator 1, Stator 2, and Stator 3 domains of the existing primary passage model, as shown in Figure 2.14. The air paths at the inlet of the compressor are all sealed, but the stator 3 cavity possesses a potential leakage path to atmospheric pressure. Therefore, the IGV cavity is sealed in the coupled cavity model, while the Stator 3 cavity possess a duct that represents the leakage path. The potential leakage path of the Stator 3 Cavity demands a boundary condition which is satisfied with the experimental data available. Hence, at the outlet of the stator 3 cavity, a corrected mass flow boundary condition is applied to ensure the leakage path of the cavity is modeled as accurately as possible. All the stationary domains are subdivided further into inlet and outlet regions where the cavity interfaces can be coupled to the stationary domain at the hub wall. An example of the Stator 1 domain and its regions is shown in Figure 2.15. Instead of the hub surface being a continuous wall, the inlet and outlet hub surfaces act as openings where the cavity leakage flow can enter or exit from the primary flow path.

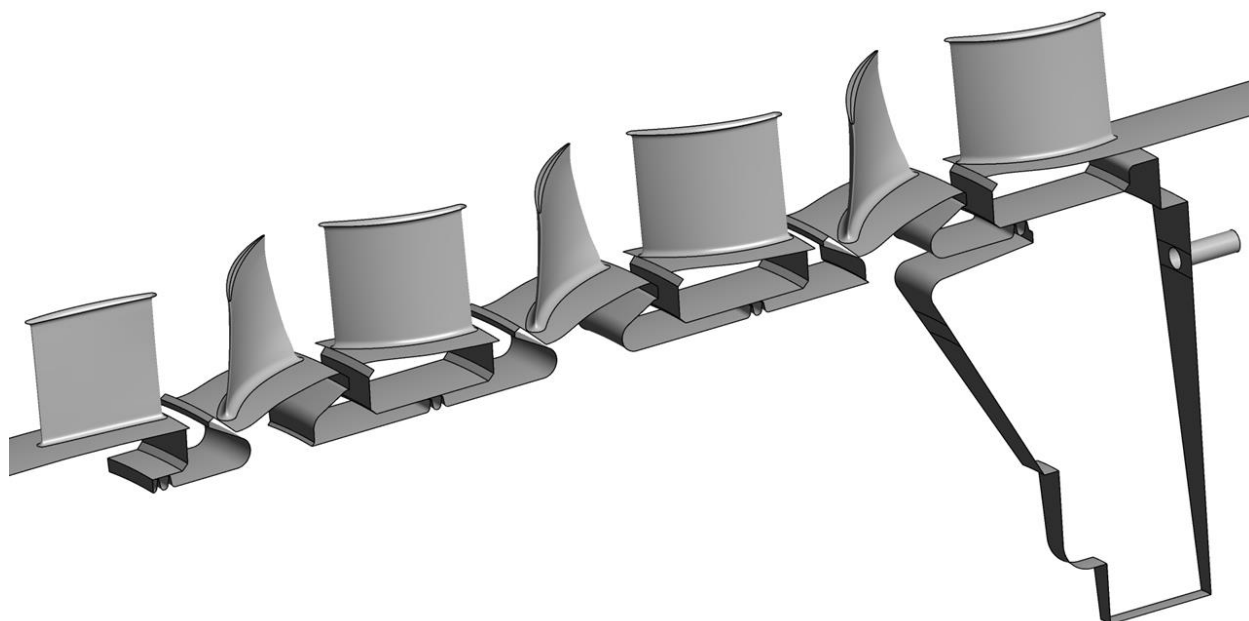


Figure 2.14: Complete coupled model of the PAX100 geometry.

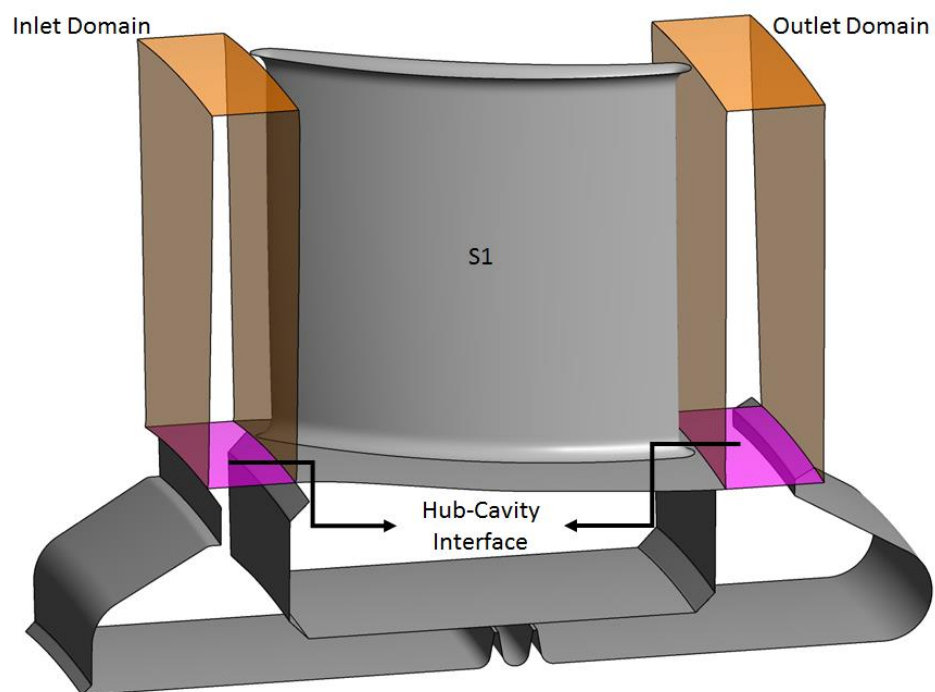


Figure 2.15: Stator domain division into inlet and outlet domains.

2.2.2.2 Domain Interfaces

All the cavities have the same passage size as the corresponding IGV or Stator domains to ensure consistent information transfer at the cavity inlet and outlet interfaces without having to take pitch angle changes into account. The cavities are attached to the stators, and therefore, the walls connected to the stators are stationary no slip walls. However, modeling the rotating rotor drum is an important aspect of this investigation. Hence, the walls connected to the rotor hub walls are subject to the same wall velocity as the rotors so as to model the effects of the rotating rotor drum. Lastly, to complete the coupling of the cavity domain with the stator domain, information transfer at the hub-cavity surfaces as labeled in Figure 2.15 must be defined. In the cavity domain, only the rotor drum wall is rotating while the other walls are stationary. Unlike the rotor-stator domains, both the stator and cavity are in the stationary domain with a fixed orientation. Therefore, a fixed relative orientation assumption is valid at this interface and the Frozen Rotor model is applied between the stator hub and cavity interfaces. At these interfaces, the frozen rotor model will take a snapshot of the flow near the hub in the primary passage and transfer the information to the cavity interface and vice versa to ensure that the cavity leakage flow and primary passage flow interactions are captured in the CFD model. The solver criteria are kept consistent with the previous model to ensure accuracy and stability of convergence as well as consistent comparison across models. A summary of the interfaces and boundary conditions can be found in Table 2.3. The results of the two base cases, primary passage model without any cavities and the cavities model using the measured cold clearance, are discussed in the next section along with the grid resolution study.

Table 2.3: Summary of Boundary Conditions of the coupled model.

Model		
Surface	Boundary Conditions	
Inlet	P_o and T_o Profiles	
Outlet	\dot{m}_c	
S3 Cavity Outlet	\dot{m}_c	
Periodic Surfaces	Rotational Periodicity	
Cavity Domains		
Surface	Boundary Conditions	
Hub-Cavity Interface	Frozen Rotor	
Stator Landing	Stationary No-Slip Adiabatic Wall	
Rotor Drum	Rotating No-Slip Adiabatic Wall	
Primary Passage Domains		
Surface	Rotor BC	Stator BC
Inlet	Stage-Mixing Plane	
Outlet		
Hub	Stationary No-Slip Adiabatic Wall	Rotating No-Slip Adiabatic Wall
Blade		Counter-Rotating No-Slip Adiabatic Wall
Shroud		

2.3 Case Study and Analysis

2.3.1 Case Study

The windage heating, circumferential velocity development, and near-hub stator performance are all a strong function of leakage flow rates. Therefore, varying the cavity leakage flow rate allows the investigation of all major parameters affected. Cavity leakage flow can be varied by changing the total pressure rise across the stator, changing the rotor rotation speed, or varying the labyrinth seal clearance, among other options. Although, changing the total pressure rise across the stator or the rotor rotation speed greatly affects the primary passage flow characteristics. Therefore, the parametric model's ability to vary the seal clearance while holding the operating conditions constant is utilized to investigate the impact of varying seal clearance of cavity leakage flow and windage heating. This allows for a relatively constant performance of the primary passage except changes in performance near the hub.

The last column of Table 2.4 shows where this case study lands in the parameter ranges classified by Lewis (2002). These parameters are defined in Figure 1.2 for the cavity geometry investigated in this case study. The cases investigated in this study range from 0.250 percent span

to 2.500 percent span clearance at increments of 0.375 percent span. While the running hot clearance was not measured during the experiments, the design cold clearance and the measured cold clearances are known. Therefore, two cases are designed to capture the flow characteristics at these known seal clearances, as well.

Table 2.4: Typical dimensions and parameter ranges along with the range studied in this work.

Parameter	Typical Range	Range Studied
Annulus Passage Height	1 to 2.5 in.	2 in.
Hub Radius (from centerline)	10 to 13 in.	10 in.
Seal Flow (fraction of annulus flow)	0.1% to 0.4%	near 0.1%
Seal Clearance (% of span)	0.3% to 2.0%	0.25% to 2.50%
Stator Well Depth	0.75 to 1 in.	0.95 in.
Stator Inlet V_θ (fraction of U_{hub})	0.50 to 0.60	0.55 to 0.80
Stator Outlet V_θ (fraction of U_{hub})	0.05 to 0.08	0.10 to 0.25

2.3.2 Data Extraction and Analysis

Similar to the rakes and detailed measurements in the experiments, rake-like lines, called turbolines, are generated using a post processing code to replicate the measurement locations in the experimental setup. Like Figure 2.2, Figure 2.16 shows the corresponding rake locations in the computational domain generated using the post-processing code. The post-processing code is constructed such that it ensures direct match with the experimental data available in the primary passage. The essential parameters of interest extracted using the post-processing code include:

1. Static Pressure, P , and Stagnation Pressure, P_o , to investigate the effect cavity clearance has on the performance of the stator.
2. Static Temperature, T , and Stagnation Temperature, T_o , to investigate the heating near the walls as well as to track the emergence of hot cavity leakage flow into the primary passage.
3. Absolute flow angle, α , to investigate the extent of flow disturbance near the hub due to the primary flow's interactions with the cavity interface.
4. Radial, V_r , Circumferential, V_θ , and Axial Velocity, V_x , to investigate the impact of the cavity on the near-hub momentum of the primary passage flow.

The pressure and temperature data are normalized with reference to ambient conditions while the momentum data is normalized with the hub velocity, U_{hub} .

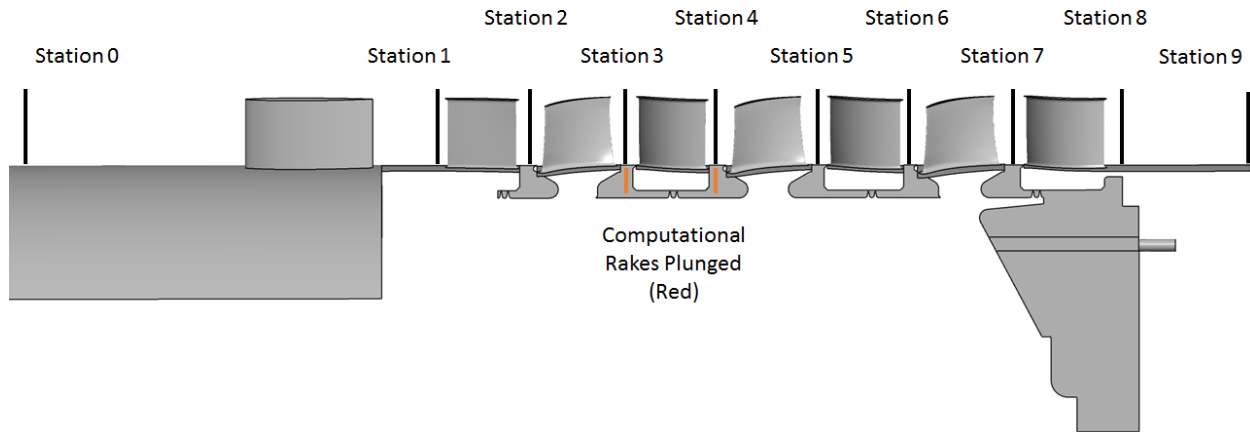


Figure 2.16: Representation of rakes in the computational domain.

In addition to matching the rake placement in the primary passage, the computational rakes are further plunged into the cavity to further understand the flow characteristics as cavity draws air from the primary flow at the stator exit domain and introduces air into the primary passage as the stator inlet domain, Figure 2.16. The post-processing code also generates area-averaged results at the inlet and outlet cavity interfaces as well as directly before and after the labyrinth seals. The surfaces used to generate the area averaged results of the bulk cavity leakage flow are the same as the hub-cavity interfaces displayed in 2.15. Lastly, to understand the details of the flow in the outlet and inlet cavity wells, radial surfaces are used. Some of the radial surfaces are displayed in Figure 2.17. They allow for the investigation of the cavity leakage flow as well as the windage heating development as the leakage flow progresses through the cavity.

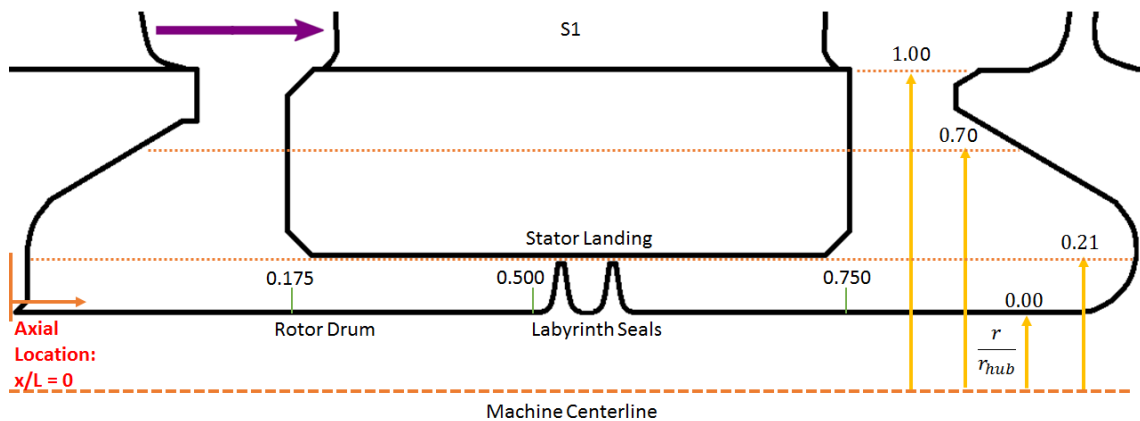


Figure 2.17: Representation of radial measurement planes in the cavity well.

One of the objectives of this investigation is to establish the overall heat generated in the flow as it enters the inlet cavity well, passes through the labyrinth seals, into the outlet cavity well and exits into the primary passage. Since no heat transfer knowledge is available for the rotor drum or the stator landing, the boundary conditions of these walls are assumed to be adiabatic. Therefore, for an adiabatic system, all windage power absorbed in a rotor/stator system must be dissipated into the cavity leakage flow as heat. Thus, to stay consistent with literature, windage heating is quantified as the total temperature rise due to the internal losses and heat generated in the seals:

$$W = \dot{m}c_p\Delta T_o, \quad (2.9)$$

where W is windage heating, c_p is the specific heat of the fluid, and T_o is the stagnation temperature.

2.3.3 Grid Convergence Study

The grid determines the spatial resolution of the flow field which is crucial in accurate predictions of recirculating flow, vortex formation, etc. Conducting a grid convergence study (GCS) is, therefore, essential and unconditionally agreed upon in the CFD community, before venturing into full analysis of the solution. Just representing the geometry and respecting the physics does not guarantee whether the CFD prediction is near the true solution. Therefore, when the degree of accuracy of the predicted results is in consideration, it is vital to determine whether the grid is fine enough. Nevertheless, the question still endures whether the degree of accuracy is worth the time and computational resources spent. In general, a fine grid tends to generate more accurate results than a coarse grid, but a fine grid leads to larger grid generation and computing time, increased computational hardware requirements, and more required processors.

First, the primary passage model was subjected to a grid convergence study in each direction, axial, radial, and circumferential individually. This grid convergence study methodology allowed for assessing the effect of grid refinement in each direction, which not only reduced the amount of computational resources required but also produced a robust grid by understanding the importance of grid refinement in each direction. For instance, this methodology revealed that more refinement is necessary in the circumferential and radial direction than in the axial direction. Therefore, following the traditional methodology of refining the entire domain with a factor of 2 would impose unnecessarily finer grid in the axial direction and required additional computational resources and time to reach convergence. Once the primary passage model refinement was

established in each direction, the cavity domains were subject to the same methodology. Table 2.5 presents a summary of the discretized domains for each grid convergence study performed.

Table 2.5: Grid Convergence Study for the isolated Stator 1 and Cavity.

	Spanwise GCS	Circumferential GCS	Inlet Outlet GCS	Cavity GCS
	Domain Cell Count in Millions			
Coarse	0.73	0.53	1.94	1.02
Medium	1.43	1.91	2.15	1.99
Fine	2.85	3.61	2.35	3.87
Finer	5.68	6.05	2.55	7.86

First, Figure 2.18 shows the convergence achieved by the CFD model after the completion of the grid convergence study. The grid resolution in the circumferential direction is observed to be the most crucial following the grid convergence study investigations. Figure 2.19 shows the results of the grid resolution study in the circumferential direction consisting of the total pressure, total temperature, and absolute flow angle at the stator 1 exit location. The experimental data available at the exit of stator 1 is also incorporated in the figure for comparison. The mid-span region shows good agreement across grids and is observed to be the least sensitive to changes in the grid resolution. On the other hand, hub and shroud end walls are observed to be more sensitive and require more resolution which is evident by the changes in total pressure and absolute flow angle profiles. Most of the improvements in resolution are observed between coarse and medium grids. Less improvements are observed between medium and fine grids, while almost no improvements are seen between fine and finer grids indicating sufficient spatial resolution of the predicted results. Therefore, the fine grid is selected to proceed with the case study. The fine grid in the stator passage is displayed in Figure 2.20, while the stator leading edge near-hub grid is displayed in Figure 2.21.

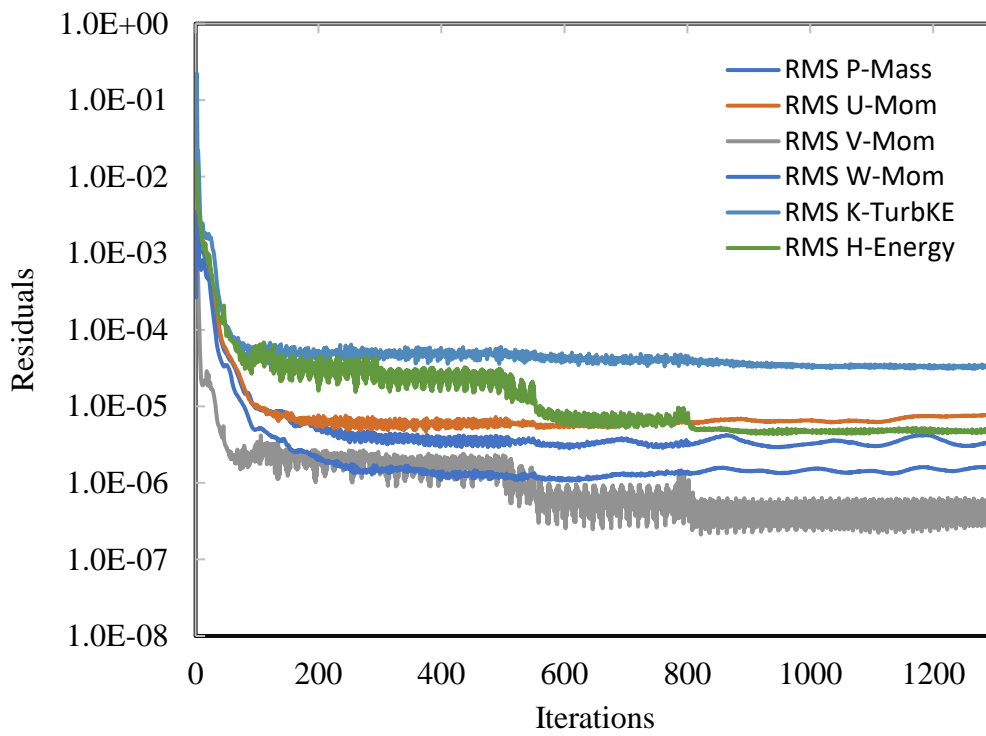


Figure 2.18: Residuals of the coupled model following the grid convergence analysis.

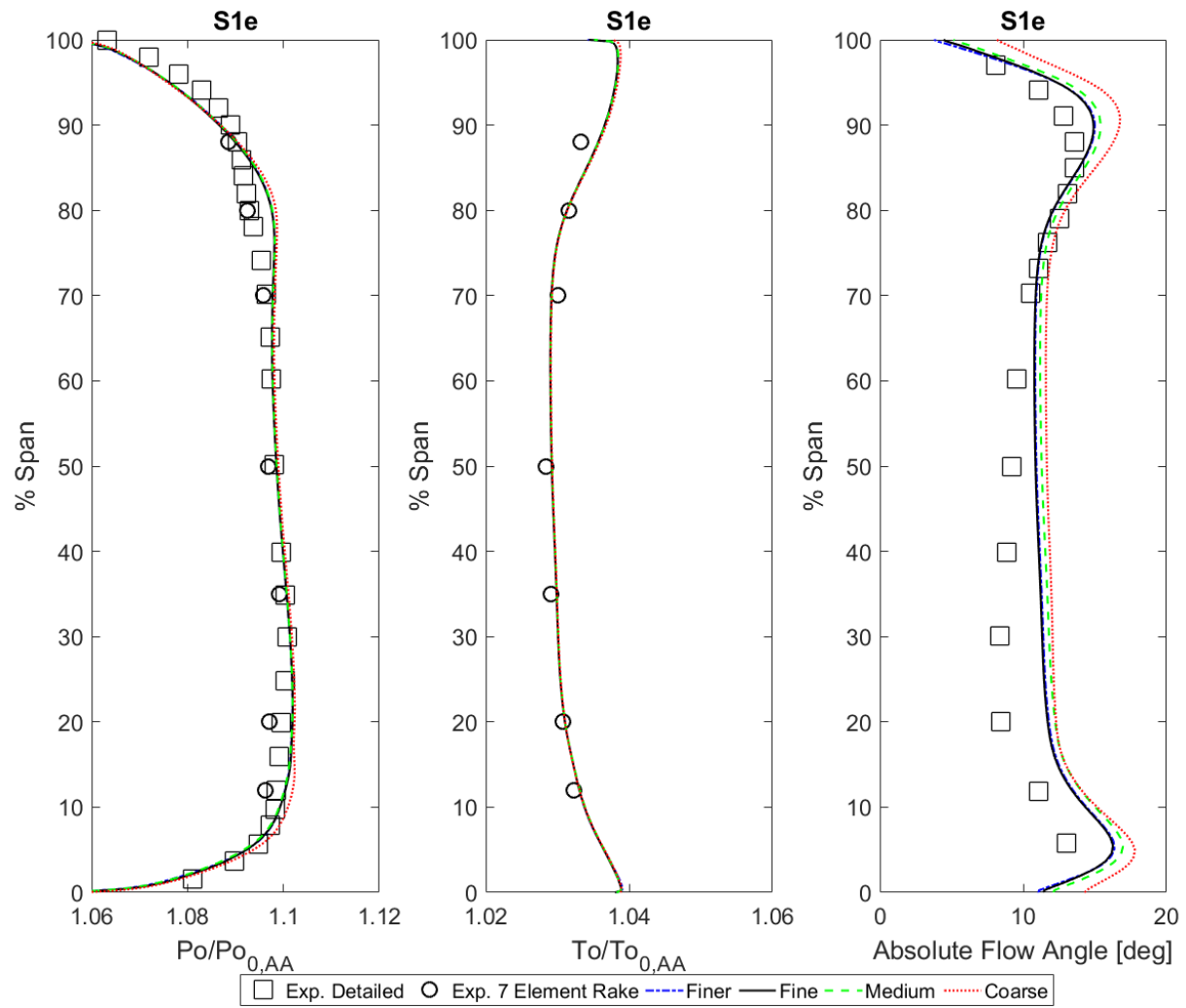


Figure 2.19: Results of grid convergence study in circumferential direction.

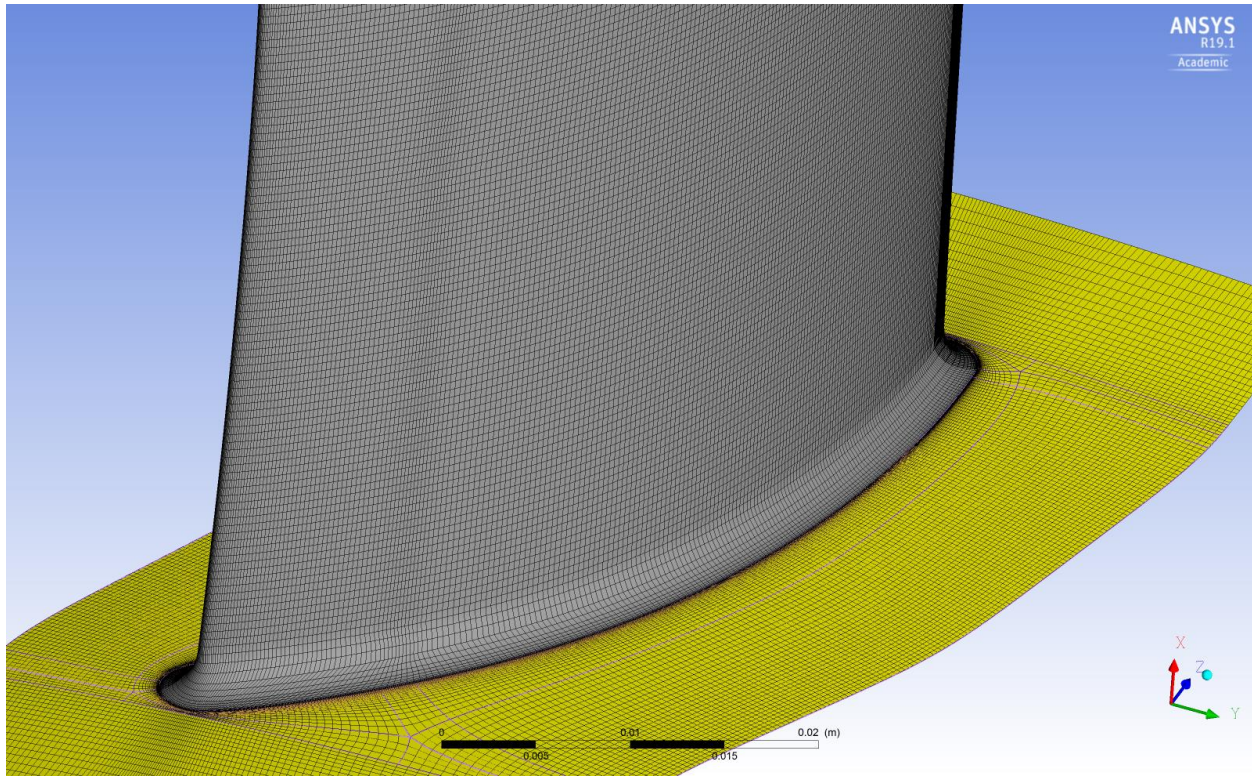


Figure 2.20: Discretized fine grid in the stator passage domain.

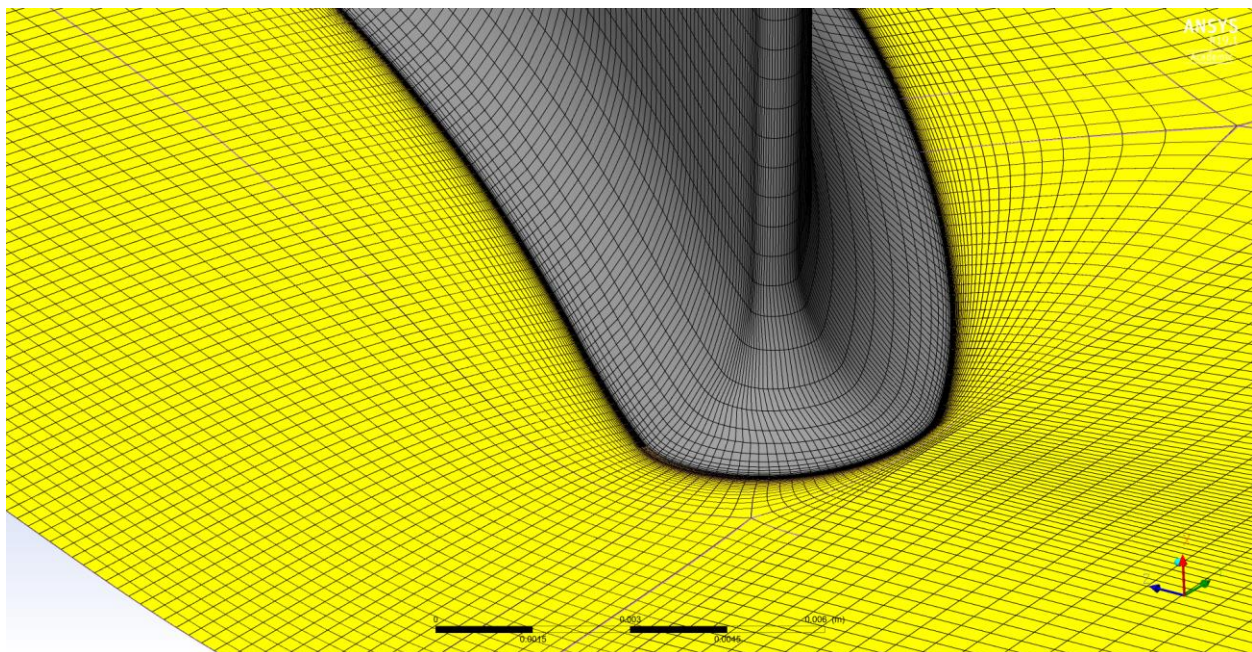


Figure 2.21: Discretized fine grid at the stator leading edge near-hub.

CHAPTER 3. INFLUENCE OF CAVITY LEAKAGE ON PRIMARY PASSAGE FLOW

After the completion of the grid convergence study, the performance of both the standalone and coupled cavity model are compared with experimental data before proceeding with the seal clearance study. Then, the results of the parametric study with varying seal clearance are presented in this section. First, the overall impact on the compressor performance is investigated to determine how the seal clearance influences the compressor's total pressure ratio, and efficiency. Stage 1 performance is also presented qualitatively using contours to gain a global understanding of the disturbances caused by the changes in cavity clearance to the primary passage flow. Then, the impact on the primary flow is quantitatively investigated using radial profiles. These are compared with the experimental results available: the standalone primary passage model and the coupled cavity model with cavity clearance. Lastly, cavity flow recirculation is investigated by analyzing the hub-cavity interfaces and tracking 3D streamlines, emerging at the stator leading edge, as they travel through the stator passage.

3.1 Standalone and Coupled Cavity Model Comparison

First, Figure 3.1 shows the performance of the CFD models on the compressor map following the grid convergence study. The performance of the standalone model on the compressor map shows that excluding the cavity can lead to an overprediction in performance, which is indicated by a higher total pressure ratio on the compressor map. Furthermore, Figure 3.2 shows the comparison of experimental data with the CFD models using inter-stage radial total pressure profiles for both, stage 1 and stage 2. The coupled cavity model shows a deterioration in near-hub performance of the stators which is not observed in the standalone model. Similarly, Figure 3.3 shows radial total temperature profiles. While the majority of the passage shows good agreement with experimental data, the standalone model underpredicts the near-hub temperatures for both stages. Lastly, Figure 3.4 shows absolute flow angle profiles. Here, the coupled cavity model shows much more deviation for the near-hub profiles at stator exit than the standalone model. Therefore, these radial profiles indicate that not modeling the cavity results in underpredicted hub temperatures, flow deviation, and overestimated performance.

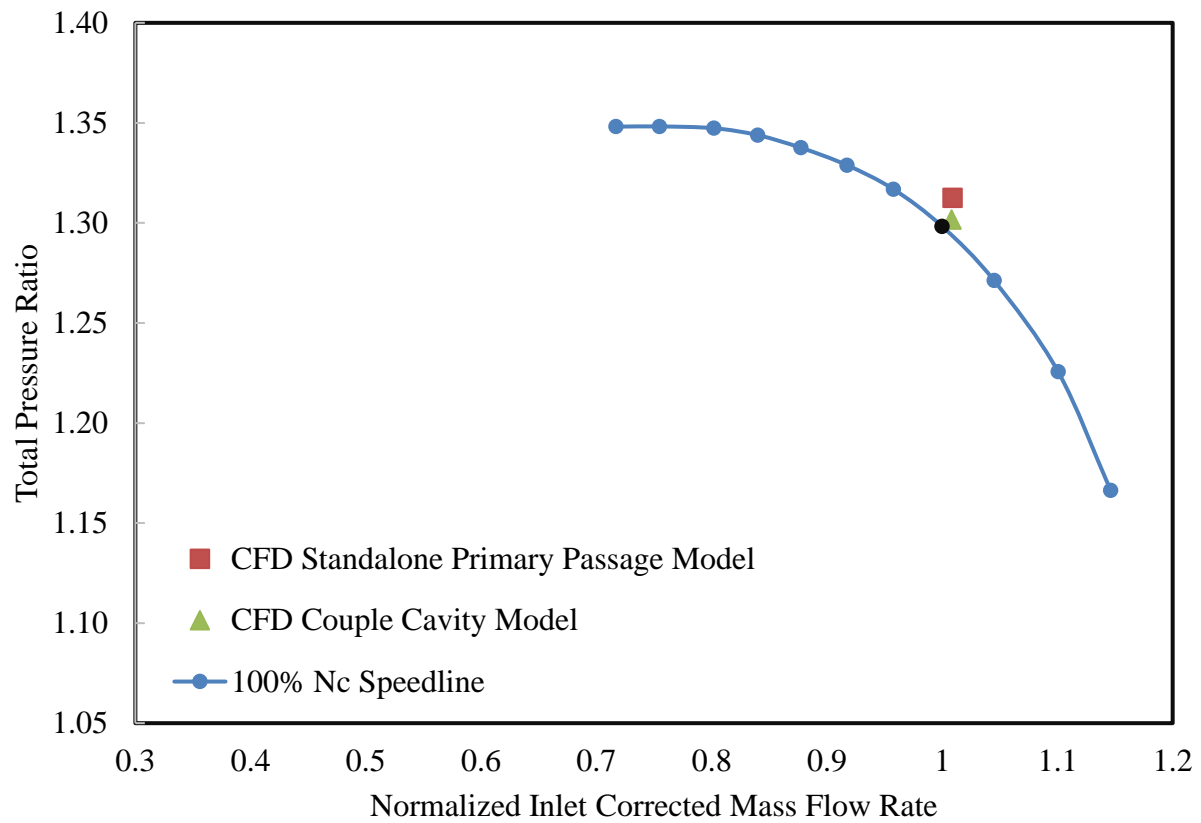


Figure 3.1: Computational model accuracy on the compressor performance map with the black dot representing the experimental operating conditions for NL.

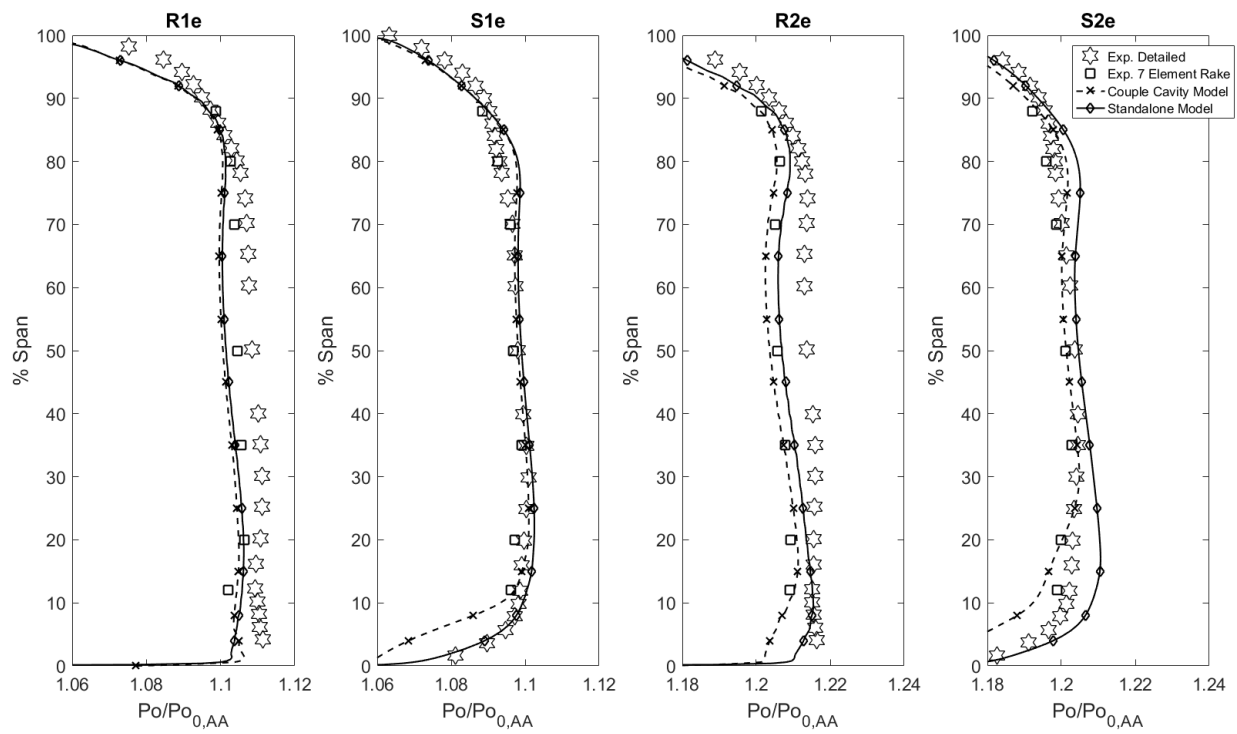


Figure 3.2: Total Pressure Radial Profiles comparing the standalone and coupled model with experimental data following GCS analysis.

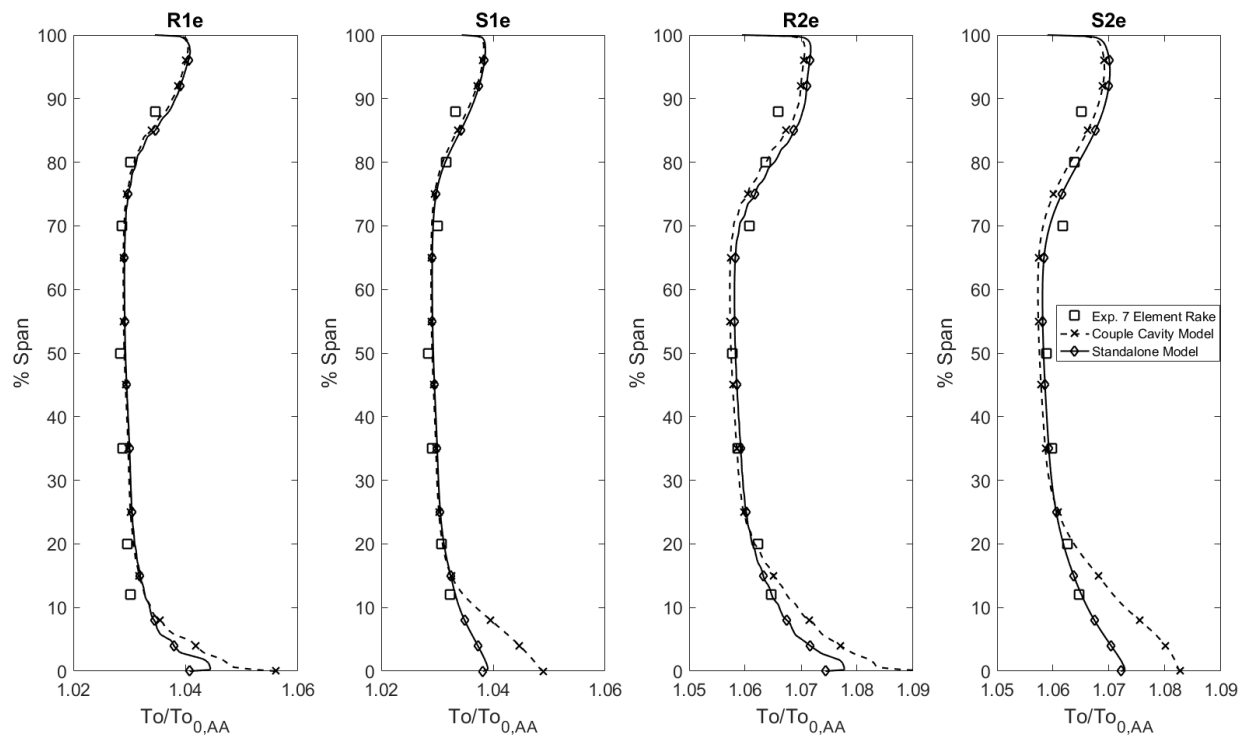


Figure 3.3: Total Temperature Radial Profiles comparing the standalone and coupled model with experimental data following GCS analysis.

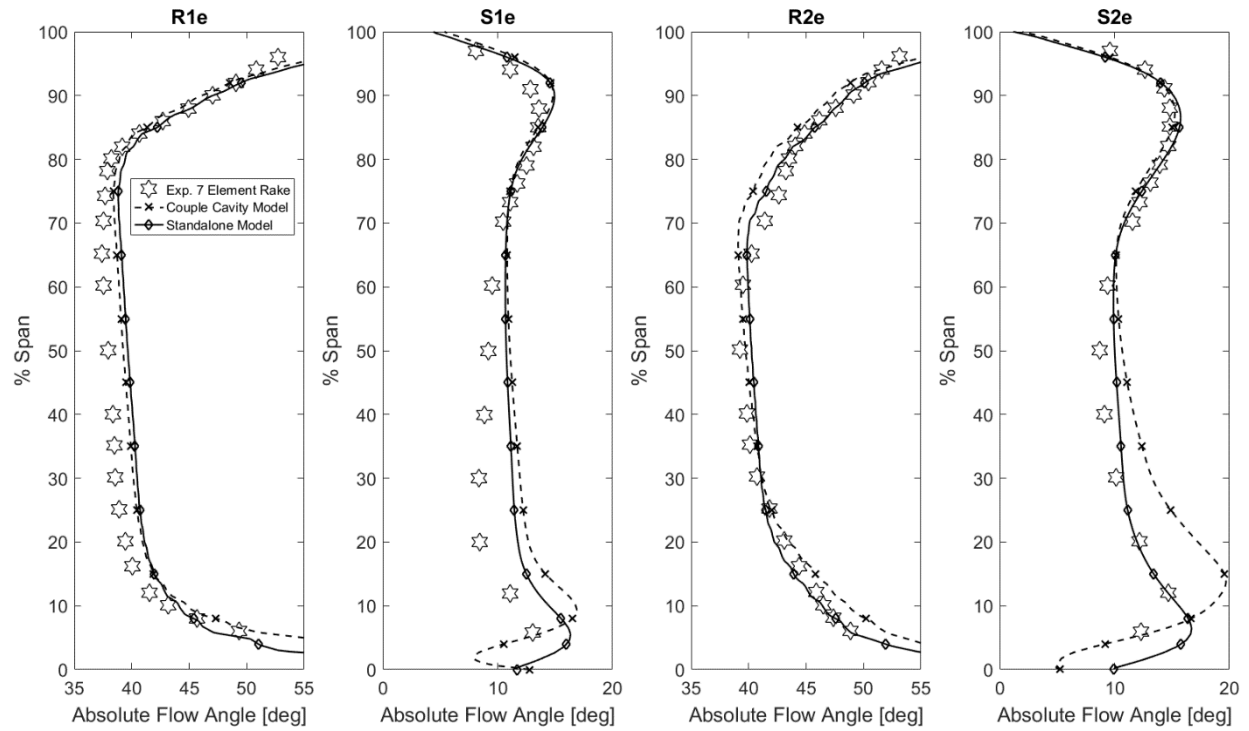


Figure 3.4: Absolute Flow Angle Radial Profiles comparing the standalone and coupled model with experimental data following GCS analysis.

3.2 Impact on Stage-wise and overall Compressor Performance

3.2.1 Overall Compressor Performance

For the seven seal clearances investigated, the effects on compressor performance are presented in Figure 3.5. Figure 3.5 shows that as the seal clearance increases, the leakage mass flow rate across the labyrinth seals increases causing a decrease in compressor performance indicated by a decrease in the efficiency and total pressure ratio delivered by the compressor. By changing only the stator 1 cavity seal clearance, every 1 percent increase in labyrinth seal clearance-to-percent span indicates an approximate 0.50 percent increase in cavity leakage flow, 0.60 percent decrease in total pressure ratio, and 0.50 point decrease in efficiency. This performance degradation is lower compared to Wellborn and Okiishi's (1999) observation of 1 percent increase in seal clearance-to-percent span, the decrease in pressure rise was 3 percent and the reduction in efficiency was 1 point. However, Wellborn and Okiishi made changes to the cavities of four stages simultaneously as opposed to making changes to cavity of a single stage, resulting in a higher performance degradation. Nevertheless, these penalties in compressor performance suggest the importance of accounting for the effects of shrouded cavity leakage when attempting to predict overall performance of a multistage compressor correctly.

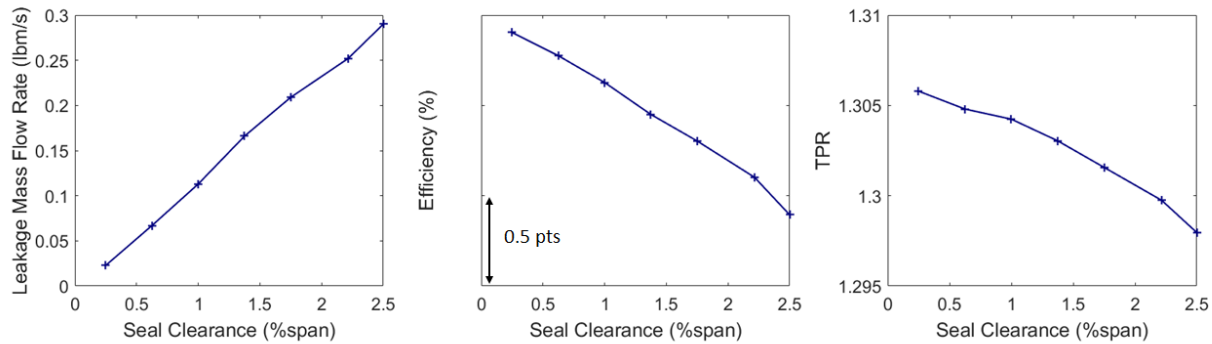


Figure 3.5: Impact of varying stator 1 seal clearance on compressor performance parameters.

3.2.2 Stator 1 Exit Performance

Stator exit contours are presented in Figures 3.6 – 3.8 to understand the primary passage flow disturbances caused by varying seal clearance. As expected, the cavity leakage disrupts the stator flow field, which, in turn, produces deteriorated stator exit flow conditions. First, the total

pressure contours, Figure 3.6, show that increasing the cavity leakage directly deteriorates the near-hub stator performance. The total temperature contours, Figure 3.7, show increasingly hot fluid exists near the hub with increasing cavity leakage flow indicating hot cavity fluid's tendency to remain near the hub and increasing possibility for re-ingestion. Lastly, Figure 3.8 shows the flow angle when increasing leakage produces additional flow blockage, deviation, and total pressure loss near the hub. As the cavity leakage flow increases, the blockage shifts radially outwards towards the shroud. In addition, data acquired near the hub suggest that the circumferential deficit in axial and circumferential momentum caused by the stator wake diminished, and instead, a radial momentum decrease was the controlling gradient. Hence, further proving the potential for re-ingestion which is discussed in detail later in this chapter.

The total pressure and total temperature contours also show a cross-passage migration occurring. Tracking the percent vane passage location of the blue and red zones in total pressure and total temperature contours, respectively, indicates that the cross-passage pressure gradient is more dominant for larger clearance. The low total pressure zone in blue for the tighter clearance, albeit very small, tends to stay closer to the pressure side while it is on the suction side for larger clearance. The total temperature contours indicate the same behavior with the hot cavity leakage fluid indicated in red. In order to ensure the fluid migrating cross-passage is, in fact, the cavity leakage fluid, various axial locations are analyzed in the next section to track the cavity leakage fluid emerging at the stator leading edge.

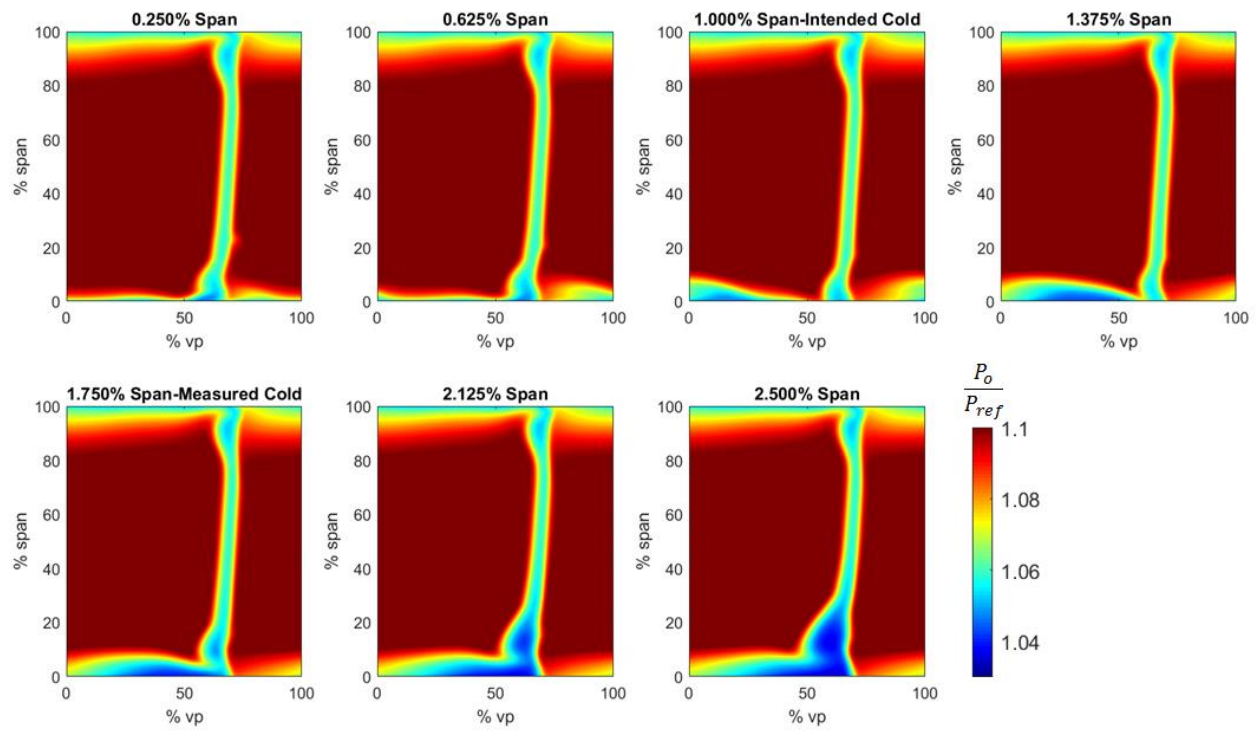


Figure 3.6: Comparison of Total Pressure contours at stator 1 exit for varying seal clearance.

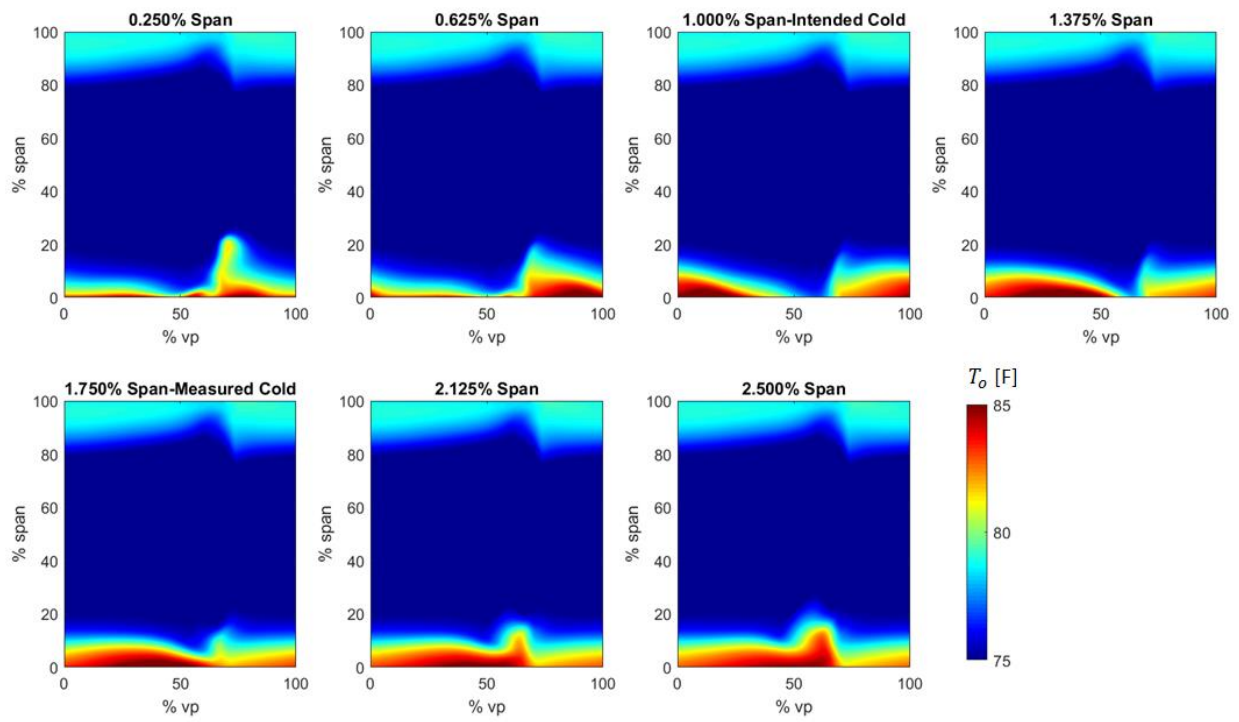


Figure 3.7: Comparison of Total Temperature contours at stator 1 exit for varying seal clearance.

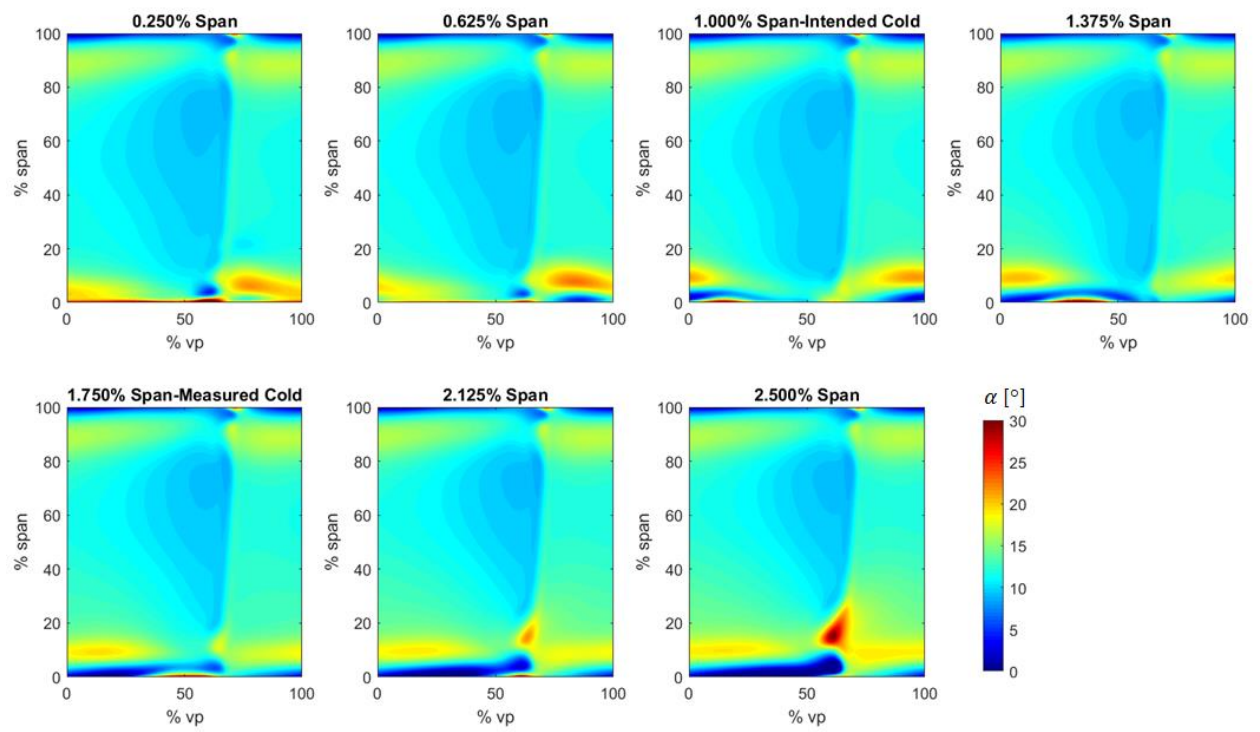


Figure 3.8: Comparison of absolute flow angle contours at stator 1 exit for varying seal clearance

3.2.3 Cross-Passage Migration of Leakage Flow

Total pressure and total temperature contours at various axial locations are presented in this section to observe the cross-passage migration of the cavity leakage fluid for the 1.75 percent span clearance case. The total pressure contours in Figure 3.9 show the cross-passage migration of the fluid as the flow moves downstream in the stator passage. More importantly, the total temperature contours in Figure 3.10 show the hot cavity leakage fluid emerging at the stator leading edge and migration towards the stator suction side as the flow progresses downstream. As the cavity clearance increases, the severity of this cross-passage migration increases, and therefore, increases the possibility of the hub corner separation. Nevertheless, for tighter clearances, the cross-passage migration is prevented due to less amount of cavity leakage fluid and higher near-hub circumferential velocity, which is discussed next.

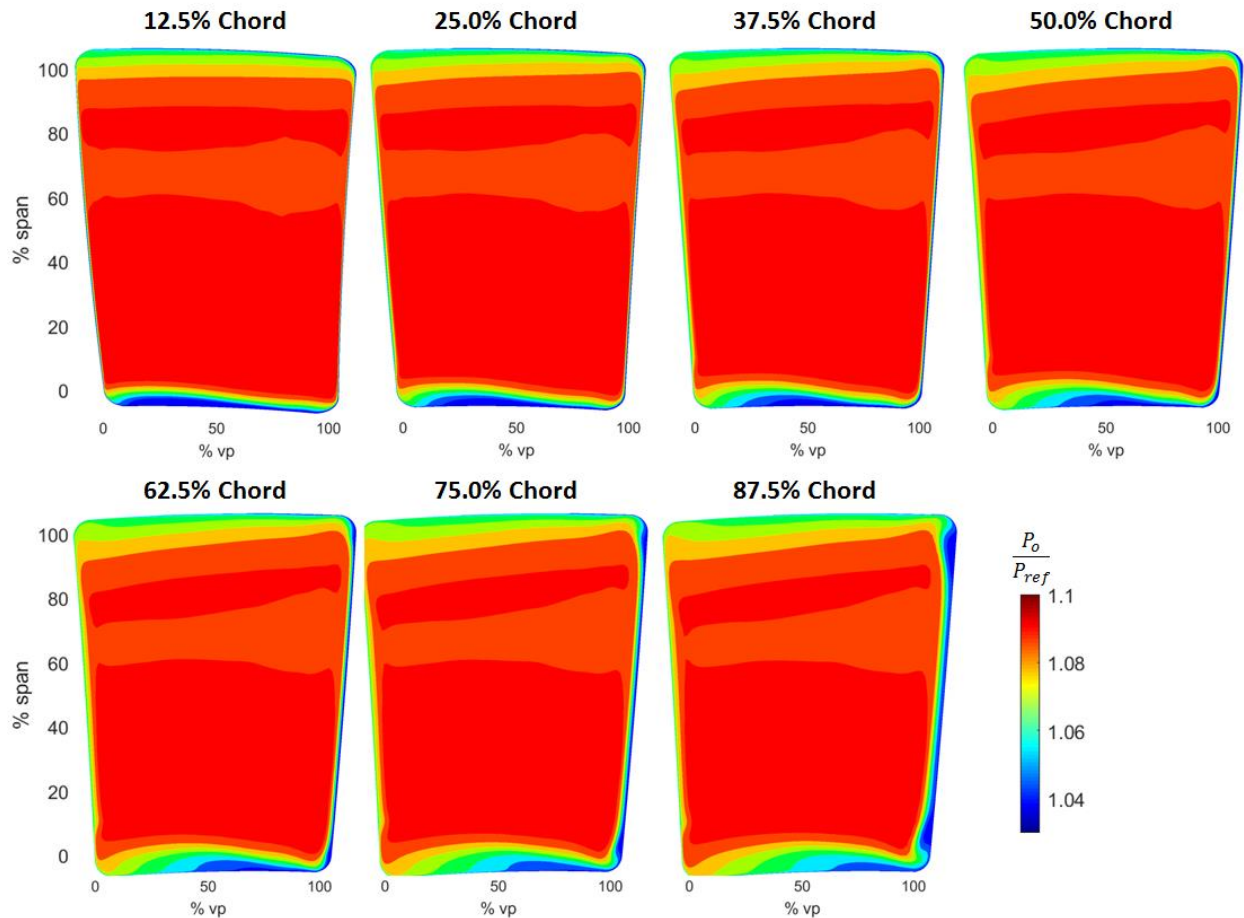


Figure 3.9: Total Pressure contours at various axial locations indicating cross-passage migration of cavity leakage fluid.

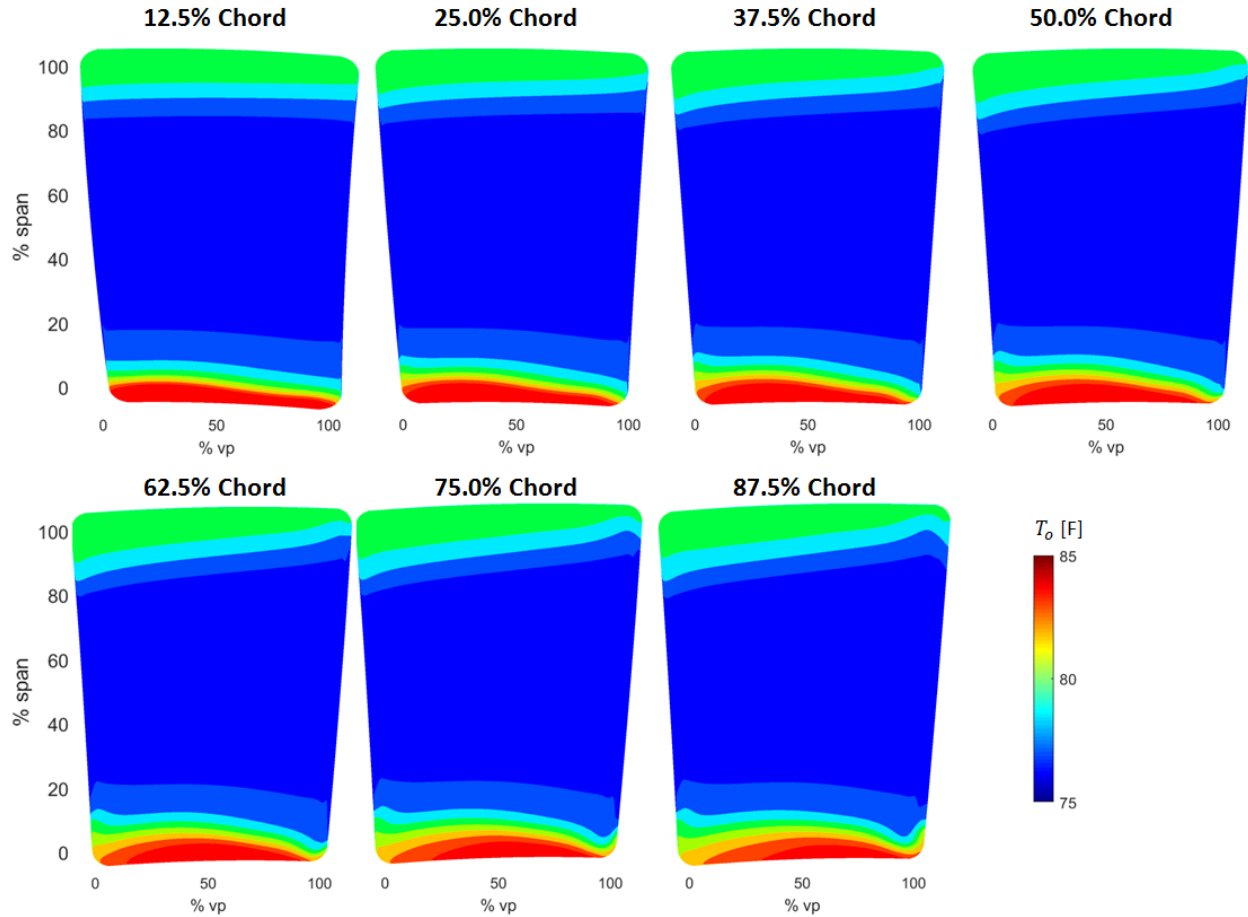


Figure 3.10: Total Temperature contours at various axial locations indicating cross-passage migration of hot cavity leakage fluid.

Figures 3.11 – 3.13 show axial, radial, and circumferential velocity contours at the stator exit. In particular, the circumferential velocity contours suggest that near-hub flow tends to move with higher momentum than primary flow in circumferential direction for tighter clearances. Therefore, a shear layer in the radial direction must exist to adjust this difference in velocity near the primary flow and hub interface. Evidently, the higher near-hub circumferential velocity prevents the cross-passage migration of the cavity leakage fluid. Although, when the near-hub fluid velocity is low, it fails to stop the cross-passage pressure gradient which drives this low momentum fluid from the pressure side of the stator to the suction side. If the suction side boundary layer is deteriorated by the cavity leakage fluid, hub corner stall, flow blockage, and higher total pressure losses are imminent. Furthermore, from the total pressure and total temperature contours, it is evident that the cavity leakage fluid tends to remain near the hub. Therefore, the fluid

originating at the stator leading edge must be responsible for controlling the circumferential momentum near the hub. If the cavity circumferential momentum is low, then the cavity leakage fluid will collect on the stator suction surface aggravating the hub corner separation and deteriorating the stator performance. Otherwise, the high cavity circumferential momentum will restrict the cavity leakage flow on the stator pressure side.

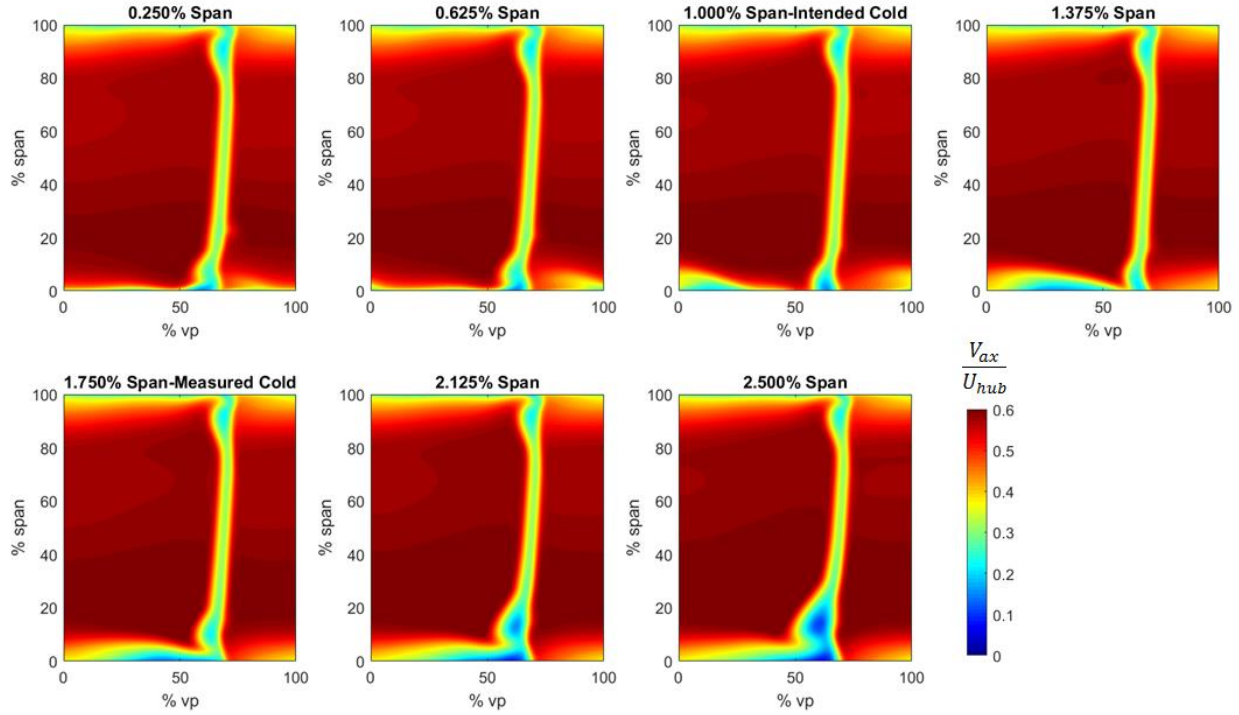


Figure 3.11: Comparison of axial velocity contours at stator 1 exit for varying seal clearance.

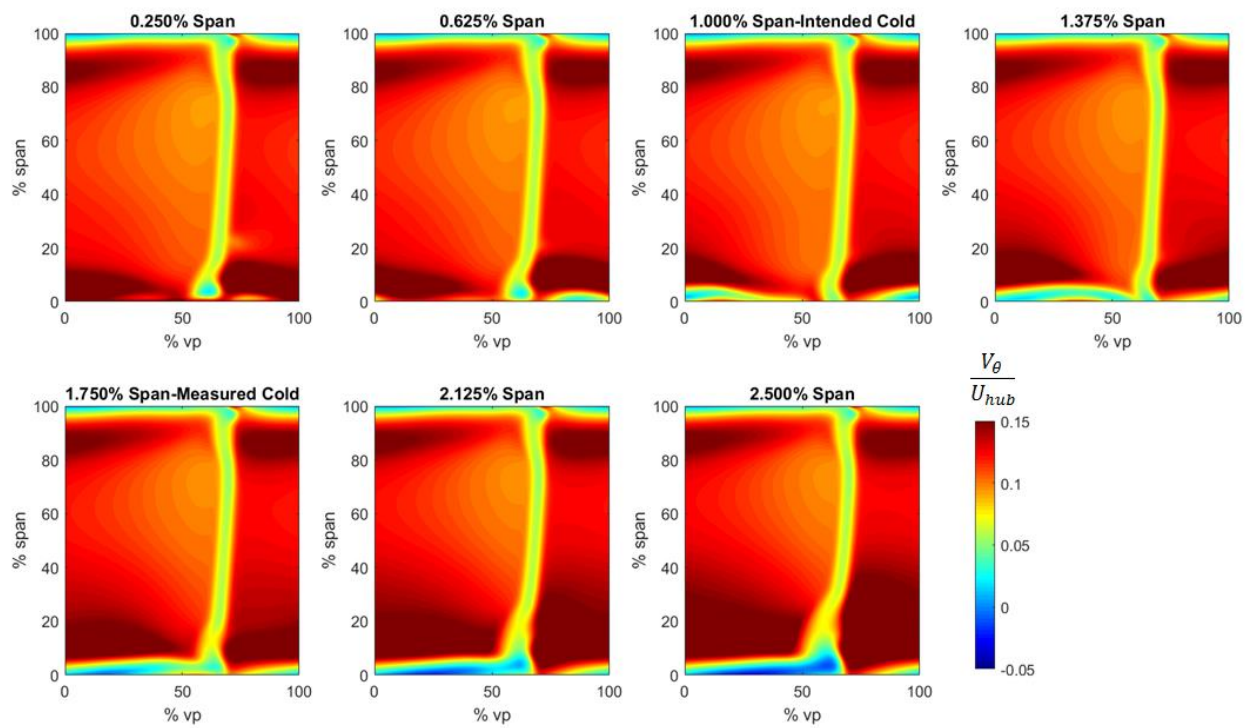


Figure 3.12: Comparison of circumferential velocity contours at stator 1 exit for varying clearance.

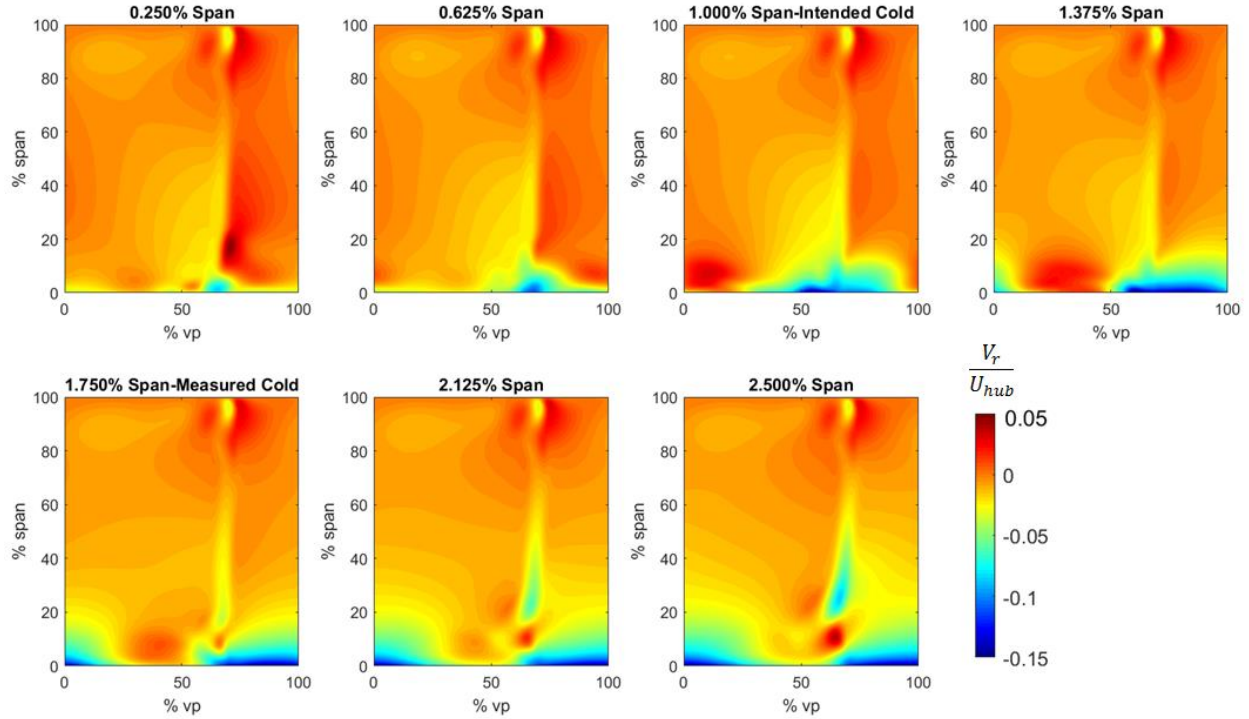


Figure 3.13: Comparison of radial velocity contours at stator 1 exit for varying seal clearance.

Examining the total pressure, total temperature and circumferential velocity contours shows that tighter labyrinth seal clearance leads to a higher circumferential momentum near the hub, which restricts the hot cavity leakage flow on the pressure side. A larger labyrinth seal clearance leads to lower circumferential momentum near the hub leading to cavity leakage flow collecting on the stator suction surface and aggravating the hub corner separation. The severity of the hub corner separation is investigated in the next section by investigating the stator suction side streamlines.

These contours provide a qualitative understanding of the impact labyrinth seal clearance and cavity leakage flow have on stator exit performance. The cavity leakage disrupts the primary passage flow and deteriorated the stator exit conditions suggesting the downstream stages will likely suffer more degradation as the deteriorated flow reaches the rotor in the next stage. Moreover, the size and depth of the hub corner separation are dependent on the cavity leakage flow, with increasing leakage showing increased separation. Also, since the cavity leakage flow originates at the upstream cavity interface, these results show that the stator primary passage flow near the hub is most sensitive to the cavity leakage flow rate and the injection temperature encountered by the stator leading edge.

3.2.4 Stator 1 Corner Separation

As mentioned in the previous section, the cross-passage pressure gradient is responsible for driving the low momentum fluid to the suction side of the stator. The accumulation of low momentum fluid will likely worsen the suction side boundary layer and cause hub corner flow separation. Most importantly, the size and depth of the hub corner separation increased with the cavity leakage flow rate. Figure 3.14 show the streamlines on the suction side of the stator vane for investigating the hub corner separation. For the cases with small cavity clearance (≤ 0.625 percent span), the stator vane showed minor separation along the hub corner starting at near 75 percent chord and extending radially to 20 percent span near the trailing edge. When the cavity clearance was larger (≥ 1.75 percent span) the hub corner separation was worsened as more flow could pass through the cavity starting at nearly 50 percent chord and extending radially as high as 30 percent span. Surprisingly, two cases, (1 and 1.375 percent span) showed improvements for the separation on the suction side with the hub corner starting at nearly 80 percent chord and extended radially to only 15 percent span near the trailing edge. These results suggest that for this combination of stator-cavity geometry and the corresponding operating conditions, there exists an optimum cavity clearance and flow rate with respect to the leading-edge incidence which is not zero leakage flow. Therefore, there exists a configuration where the hub corner stall, flow blockage, and total pressure loss can be reduced to optimize the stator exit performance.

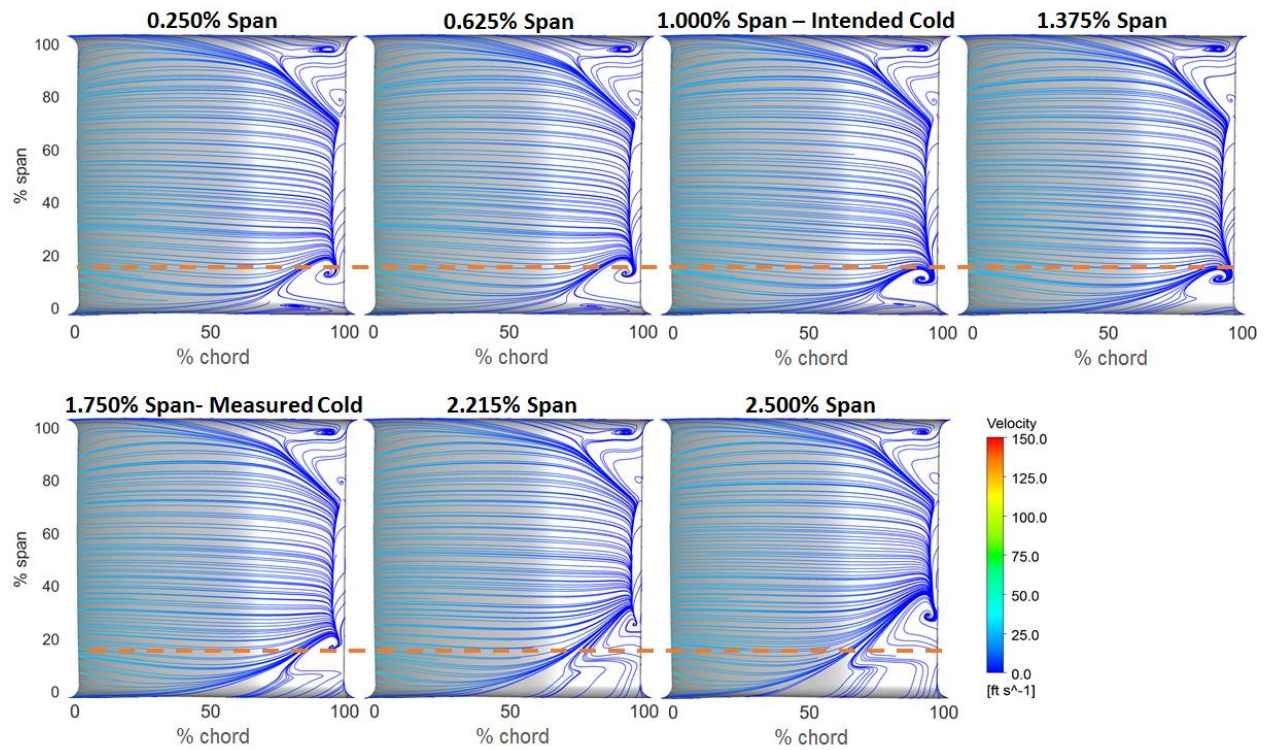


Figure 3.14: Comparison of suction side streamlines on stator 1 vanes for varying seal clearance.

3.3 Inter-Stage Flow Profiles

3.3.1 Total Pressure and Total Temperature Profiles

Figures 3.15 and 3.16 show the circumferentially averaged total pressure and total temperature radial profiles of stages one and two to investigate the effects of cavity leakage flow on the corresponding upstream and downstream blades. Again, only the labyrinth seal clearance under stator 1 is varied while the other cavity clearances are set to the measured cold clearance values. First, the radial total pressure profiles show that the rotor 1 exit total pressure profiles are not affected by the downstream stator cavity leakage flow. This is because majority of the cavity leakage flow exits the cavity on the downstream face of the cavity, i.e., near the stator leading edge. While this is not evident from these profiles, section 3.4 analyzes the near-hub flow upstream of the stator leading edge, which proves that the downstream stator cavity leakage, in fact, does not hinder the upstream rotor performance.

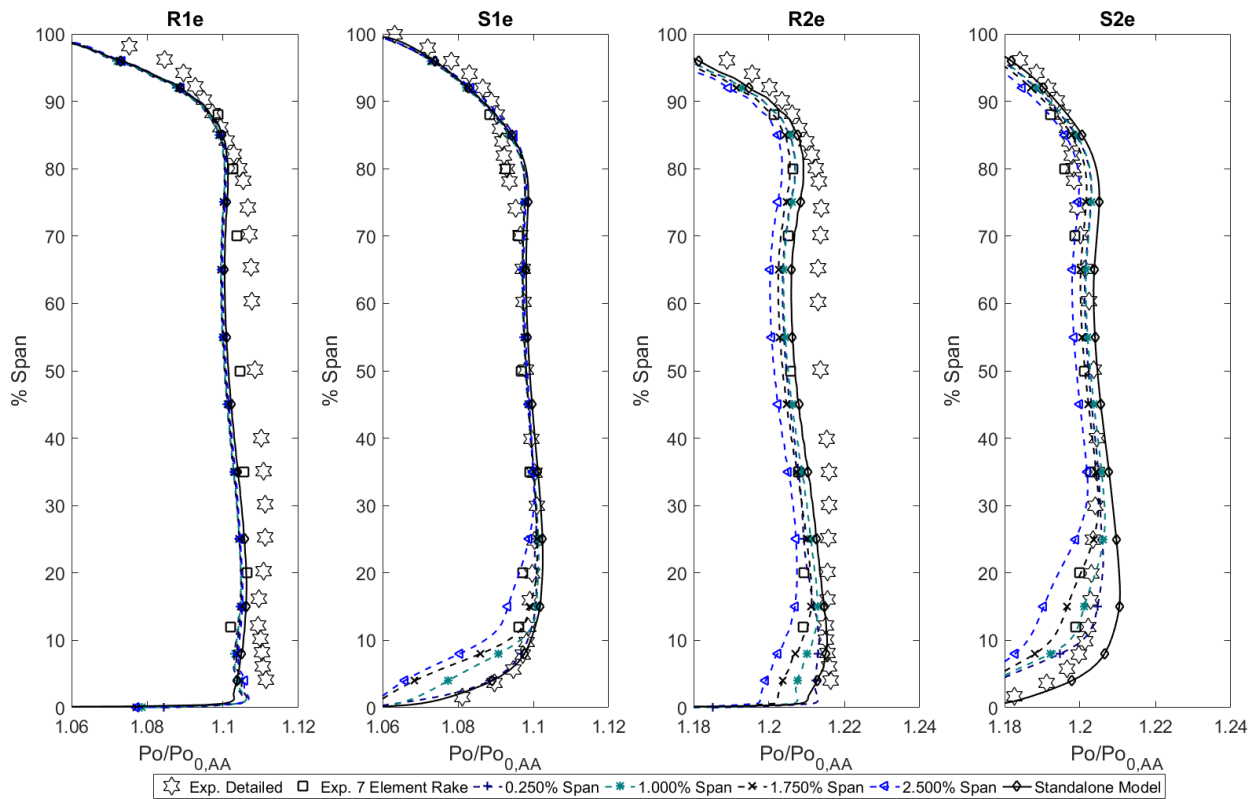


Figure 3.15: Total Pressure Radial Profiles comparison of varying seal clearance with experimental data.

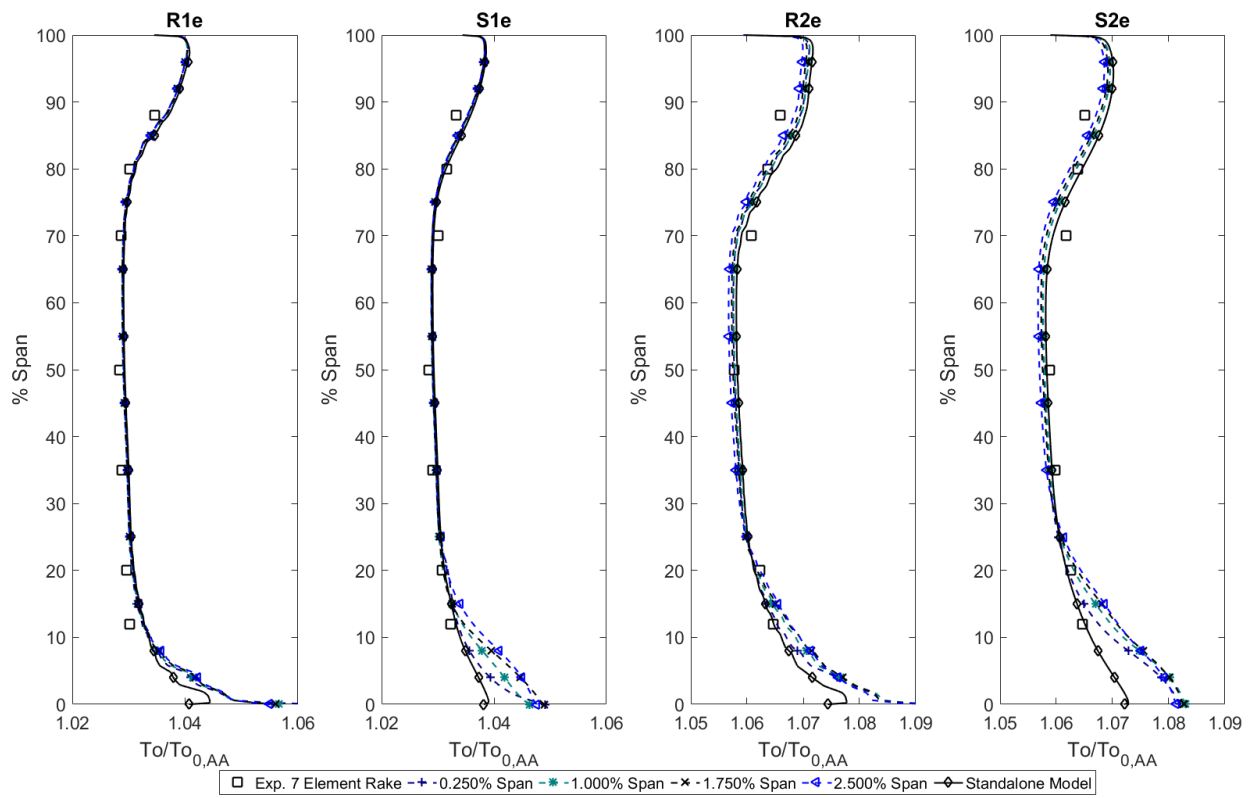


Figure 3.16: Total Temperature Radial Profiles comparison of varying seal clearance with experimental data.

Nevertheless, the cavity leakage flow influences the performance of the stator in the same stage as well as both the stator and rotor performance in the downstream stages. Radial profiles at stator 1 exit show that the cavity leakage flow hinders the stator performance by increasing the total pressure loss and higher total temperature delivered due to the hub corner flow separation analyzed earlier. Consequently, the cavity leakage flow also indirectly affects the downstream rotor performance because the disrupted stator primary flow field produces deteriorated stator exit flow conditions. The downstream rotor is not able to improve the degraded incoming flow as seen from the near-hub total pressure profiles at rotor 2 exit. As a consequence, the cavity leakage flow indirectly influences the stator 2 performance as well. Therefore, as the altered flow moves downstream and encounters the next stator, the near-hub performance would continue to deteriorate. Similar observations were examined by Wellborn and Okiishi (1999) in concluding that the designer must not only account for the influence of seal-tooth leakage in the design of the stator in which cavity leakage occurs but also consider the impact on downstream blade rows.

3.3.2 Absolute Flow Angle and Momentum Variations

Figures 3.17 – 3.20 represent the variations observed in the absolute flow angle and the axial, radial, and circumferential velocity variations due to the changes in labyrinth seal clearances. These profiles help further explain the mechanisms affecting the stage performance. The rotor 1 exit circumferential velocity profiles show that the fluid near the upstream cavity interface exists at a higher circumferential velocity than the primary flow. Due to this, the incidence on the stator blade near the hub is higher than the mid-span as depicted in the absolute flow angle profiles of rotor 1 exit (R1e). The increase in incidence near the hub region increases the chance of blockage and result in hub corner separation. This extra blockage near the hub forces flow radially outwards, towards the shroud and unloads some portion of the stator span. Nevertheless, the total pressure loss related to the midspan region of the stator remains largely unchanged. Below 50 percent span, the cavity seal clearance dictates the amount of radial mixing occurring in the primary passage. Tighter clearances limit radial mixing below 10 to 15 percent span as seen from the radial profiles. However, larger clearances can deteriorate performance as much as up to 30 percent span.

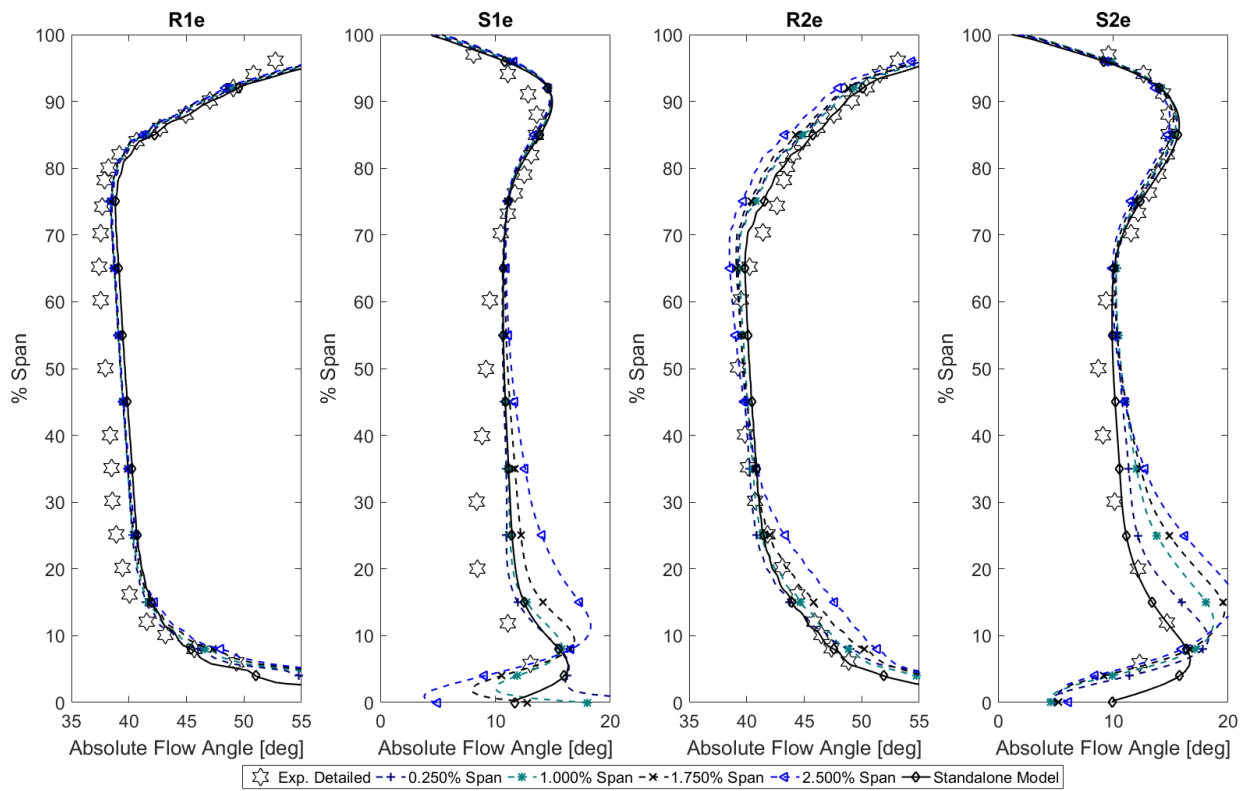


Figure 3.17: Absolute Flow Angle Radial Profiles comparison of varying seal clearance with experimental data.

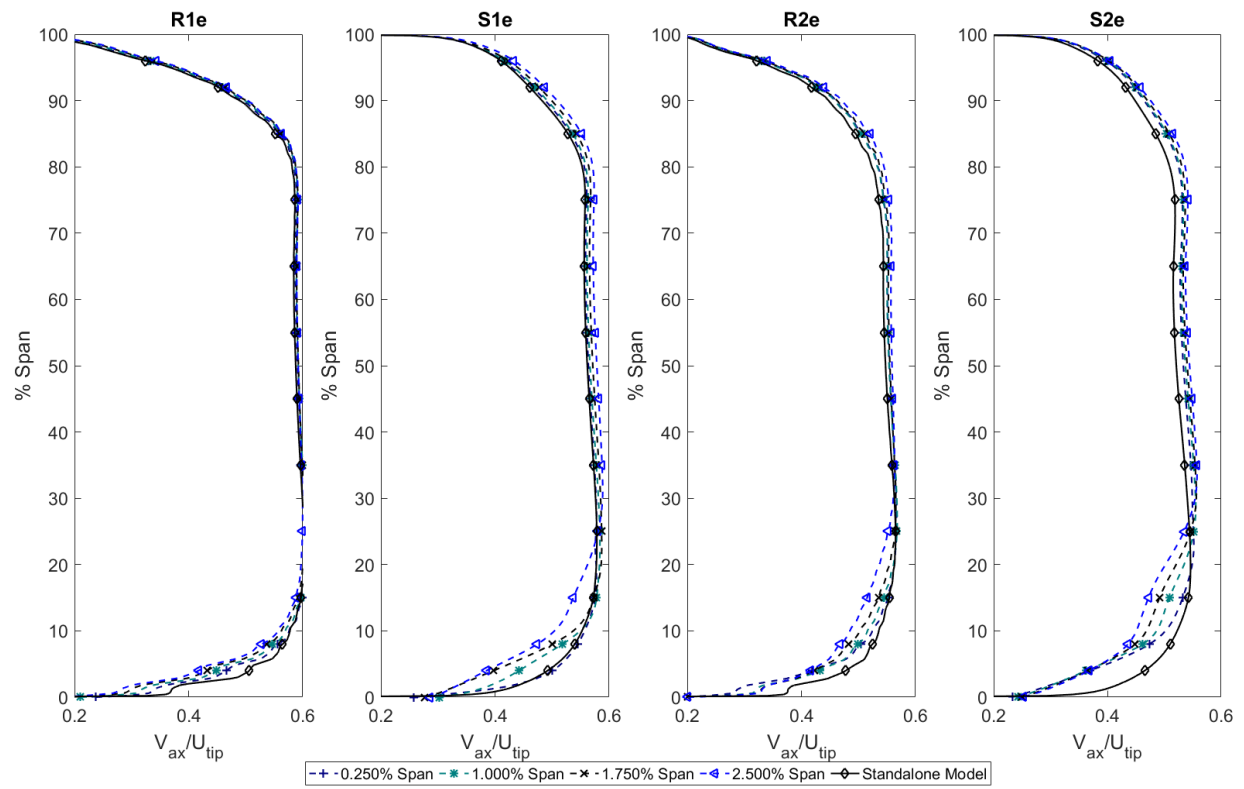


Figure 3.18: Axial Velocity Radial Profiles comparison of varying seal clearance with standalone model.

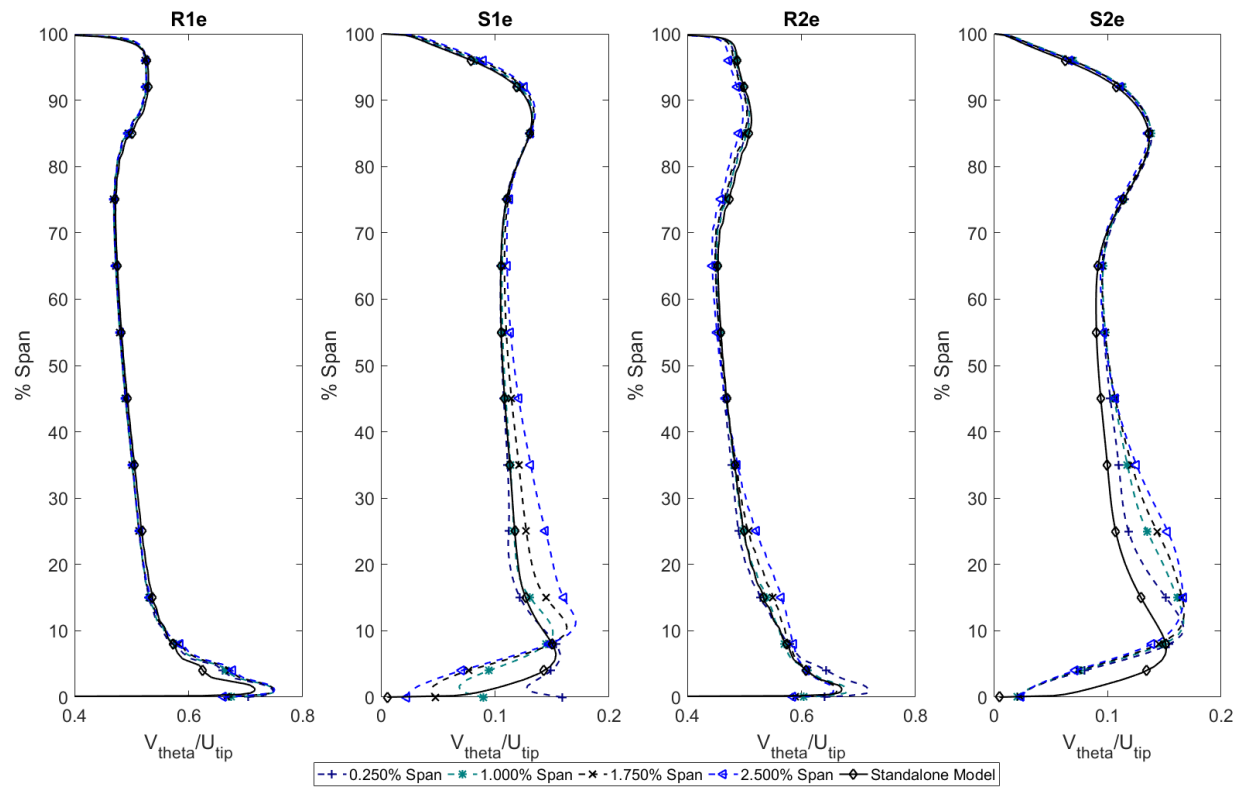


Figure 3.19: Circumferential Velocity Radial Profiles comparison of varying seal clearance with standalone model.

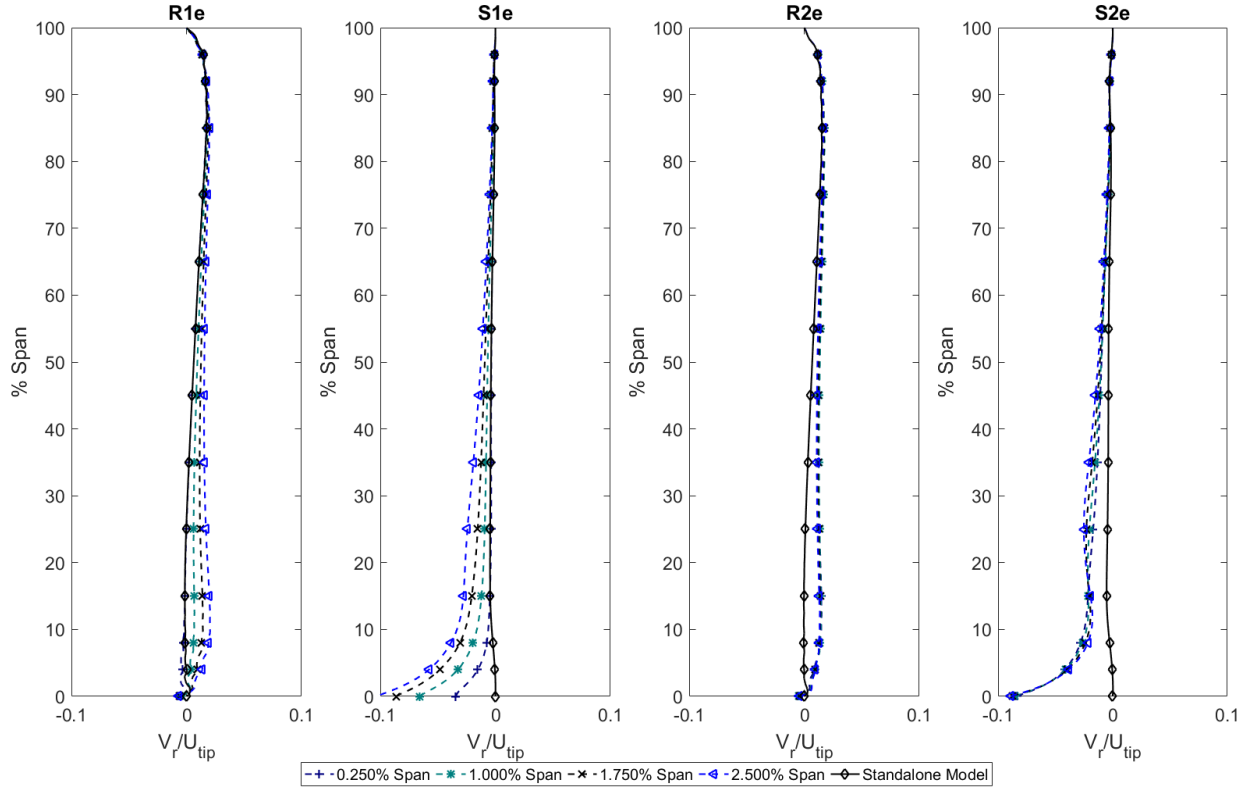


Figure 3.20: Radial Velocity profiles comparison of varying seal clearance with standalone model.

More importantly, the stage one profiles confirm that the increase in hub corner separation, observed in the contour plots, with increasing clearance is associated with lower circumferential velocity fluid near the hub. Low near-hub circumferential velocities also coincide with low axial velocities. This not only strengthens near-hub secondary flows but also increases the hub corner separation. On the other hand, for high near-hub circumferential velocities above primary passage values, excess momentum in the circumferential direction offsets low near-hub axial momentum by preventing the cross-passage pressure gradient from worsening the hub corner separation. Stator 1 exit circumferential profiles show that the large clearances possess lower circumferential velocity than tighter clearances reinforcing that the cross-passage flow increases when more leakage or lower tangential velocity fluid is introduced at the upstream cavity interface. Hence, increasing the cavity circumferential velocity, i.e. tighter clearance, will significantly diminish the development of the hub corner separation. As the cavity circumferential velocity increases the near-hub portion of the stator experiences increased flow turning, while flow turning is decreased for the flow forced radially outwards. However, the majority of the differences observed in the

parameters for the cavity clearance range of 0.25 to 2.5 percent span was near the 1 percent span clearance. The profiles depict less sensitivity with varying cavity clearance near the ends of the range, namely 0.25, 0.625, 2.125, 2.5 percent span, but more sensitivity near 1 percent span clearance suggesting that the aerodynamic design considerations can be narrowed down to a range for optimization purposes. On the other hand, if the labyrinth seals tend to operate near the more sensitive range, then experimental data collection and processing could prove to be extremely difficult without knowing the operation (hot) clearance values for the labyrinth seals.

As discussed in the section above, the altered stator exit flow conditions continues to deteriorate the performance of the downstream stages which is apparent by observing the distortion of primary passage flow from the rotor 2 exit (R2e) and stator 2 exit (S2e) radial profiles. The performance of stator 2 exit is especially deteriorated for the largest labyrinth seal clearance with flow disturbances lasting as high as 40-50 percent span. Lastly, stator 1 exit radial profiles also show increasingly negative radial momentum with increasing cavity clearance, confirming the cavity drawing more fluid from the primary flow with increasing labyrinth seal clearance. Similar observations about the important of circumferential and radial momentum on stator performance were observed by Demargne and Longley (2000). Therefore, radial profiles along with the detailed contour plots classify the major mechanisms affecting the primary passage performance due to the changes in labyrinth seal clearance. The next section explores the mechanisms near the hub-cavity interface to understand the interactions between the primary passage flow and the cavity leakage flow as the leakage flow enters and exits the cavity.

3.4 Cavity Flow Recirculation

First, to examine cavity flow recirculation, the radial momentum at the inlet and outlet cavity interfaces must be investigated. Therefore, in this section, the circumferential variations at the inlet and outlet cavity interfaces are presented using qualitative radial momentum contour plots. Then, 3D streamlines emerging from the cavity at the stator leading edge are traced across the stator passage to investigate whether the emerging cavity leakage flow is re-ingested at the cavity outlet interface.

3.4.1 Circumferential Variations at hub-cavity interfaces

Figure 3.21 shows the radial momentum at the outlet and inlet cavity interfaces, respectively. The radial velocity contour at the outlet cavity interface shows that the potential field established by the stator vane dictates where the cavity leakage flow exits, and as the seal clearance increases the fraction of the cavity outlet interface allowing flow to exit continues to increase suggesting more leakage flow entering the primary passage. Nevertheless, majority of the fluid egresses near the downstream surface of the cavity, i.e., near the stator leading edge. At the inlet cavity interface, negative radial momentum is denoted by blue to indicate the flow being ingested into the cavity. While the magnitudes are different for all cases, the negative radial momentum region spans the entire vane passage for all cases except for 1.000 and 1.375 percent span clearance cases which show almost no negative radial momentum in the middle of the passage. These contours suggest that the possibility of cavity leakage flow re-ingestion exists if the heated flow from the outlet cavity well dwells in the primary passage boundary layer and arrives at the negative radial momentum region at the inlet cavity interface. On the other hand, if the heated efflux from the outlet cavity well happens to avoid the negative radial momentum region at the inlet cavity interface, the possibility of re-ingestion diminishes. This conjecture is investigated by tracing the heated efflux from the outlet cavity well in the next section.

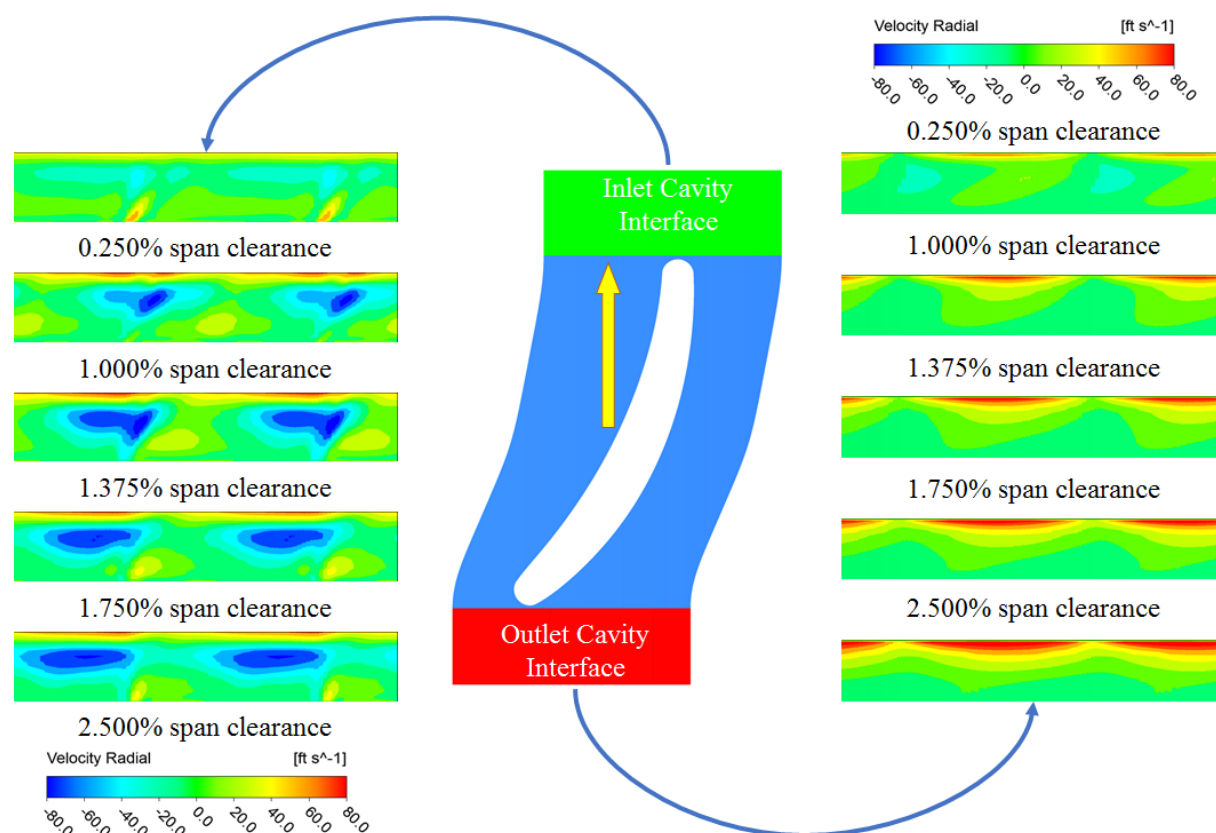


Figure 3.21: Radial velocity contours at the inlet and outlet cavity interfaces.

Circumferential pressure and velocity variations are also presented to quantitatively explain the flow interactions near the hub-cavity interface with the cavity leakage flow incoming or leaving the primary passage, and specifically whether the primary passage potential field plays any role in these interactions. Figure 3.22 shows the circumferential variations at the upstream and downstream hub-cavity interfaces. Near the upstream interface, the circumferential variations in the flow properties exist due to the potential field established by the stator. The profiles suggest that the cavity leakage flow is driven radially inwards relative near the leading edge of the stator due to the stagnation point, while the leakage flow entered the primary passage away from the leading edge. Moreover, the circumferential variations at the upstream interface, circumferential velocity for varying clearances along with nearly constant axial velocity, gave rise to a significant variation in the flow angle which was apparent in the radial profiles presented earlier.

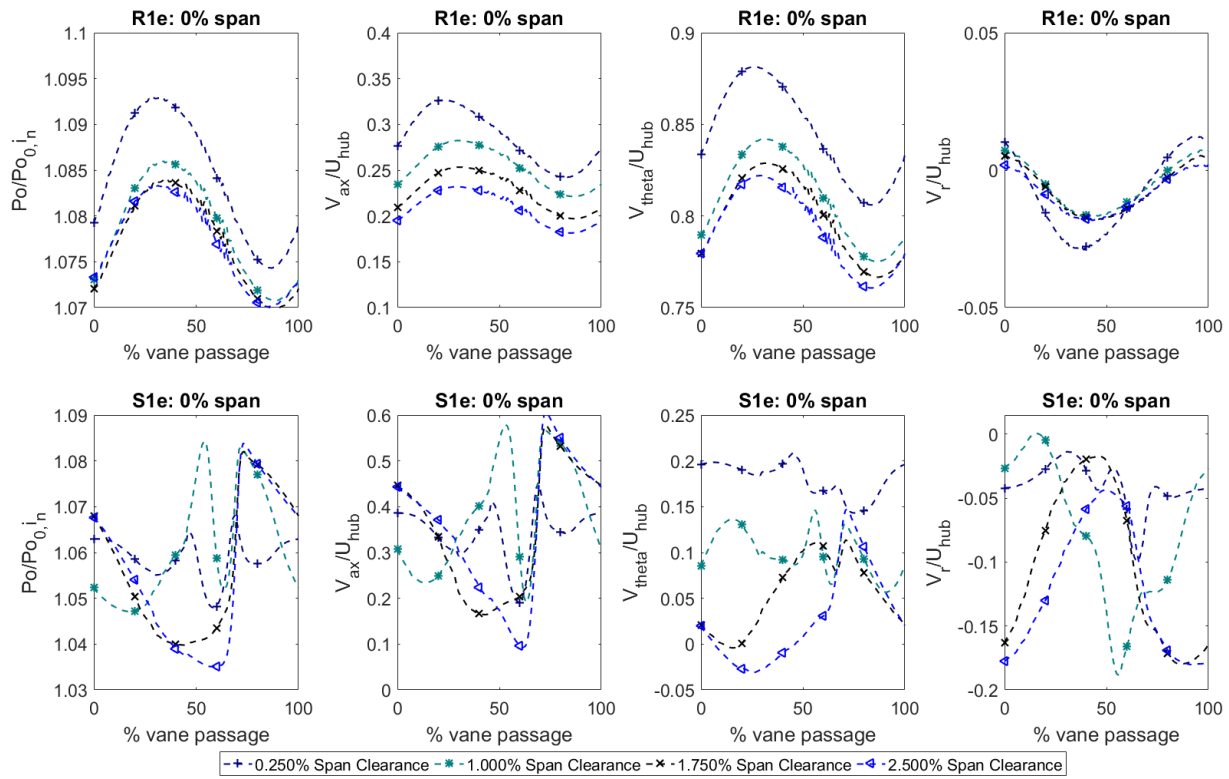


Figure 3.22: Circumferential variations of Total Pressure, Axial, Circumferential, and Radial Velocity profiles for varying seal clearance at hub-cavity interface.

For the downstream cavity interface, the most apparent variations were caused by the secondary flow, namely the stator wakes and hub corner separation, if any, present in the primary passage. These secondary flows governed, across the stator pitch, which fluid particles are ingested in the cavity. This is shown in the total pressure profiles along with radial profiles. For tighter clearance values, there is little to no hub corner separation. Therefore, the majority of the high radial momentum, an indication of flow being ingested, is at the same circumferential location as the stator wake, namely near 60-65 percent vane passage. However, as the hub-corner separation starts to dominate, the majority of the flow being ingested is dictated by the size of the hub corner separation. Moreover, these circumferential variations in radial velocity disappear by -10 percent span (data not shown here), further enforcing that the spanwise secondary flows in the primary passage dictate flow ingestion along which circumferential portion of the passage. Similar observations were observed by (Wellborn, 2001; Heidegger, 1996) regarding both the upstream and downstream interfaces being influenced by the primary passage flow.

3.4.2 Streamlines Indicating Re-ingestion

Figures 3.23 – 3.27 shows the 3D streamlines of the heated efflux emerging from the outlet cavity well and traveling downstream towards the inlet cavity interface. For the tight clearance case, 0.25 percent span, the emerging cavity leakage flow arrives at the negative radial momentum region and part of the leakage flow is shown to be re-ingested in the cavity. For the 1.0 percent span case, the emerging cavity leakage flow manages to avoid the negative radial momentum region completely and passes through the stator domain without being re-ingested. Lastly, for the large clearance case, 2.5 percent span, the emerging cavity leakage flow manages to partly avoid the negative radial momentum region. Comparatively, for large clearance cases, the leakage mass flow is much higher, and part of the flow gets entangled in the hub corner separation which allows only a portion of the heated leakage flow to be re-ingested. This phenomenon could potentially lead to extremely high temperatures in the cavity for the tight clearance cases, which is observed when investigating the cavity wells in Chapter 4. Nevertheless, this analysis also advocates for the existence of an optimum case. In general, tighter clearance seems to improve aerodynamic performance but also show high cavity temperatures with the possibility of excessive cavity heating due to re-ingestion. However, there exists a range of seal clearance, namely 1.0 and 1.375

percent span in this investigation, that prevents the heated cavity leakage flow from traveling to the negative radial momentum zone at the inlet cavity interface and avoid re-ingestion.

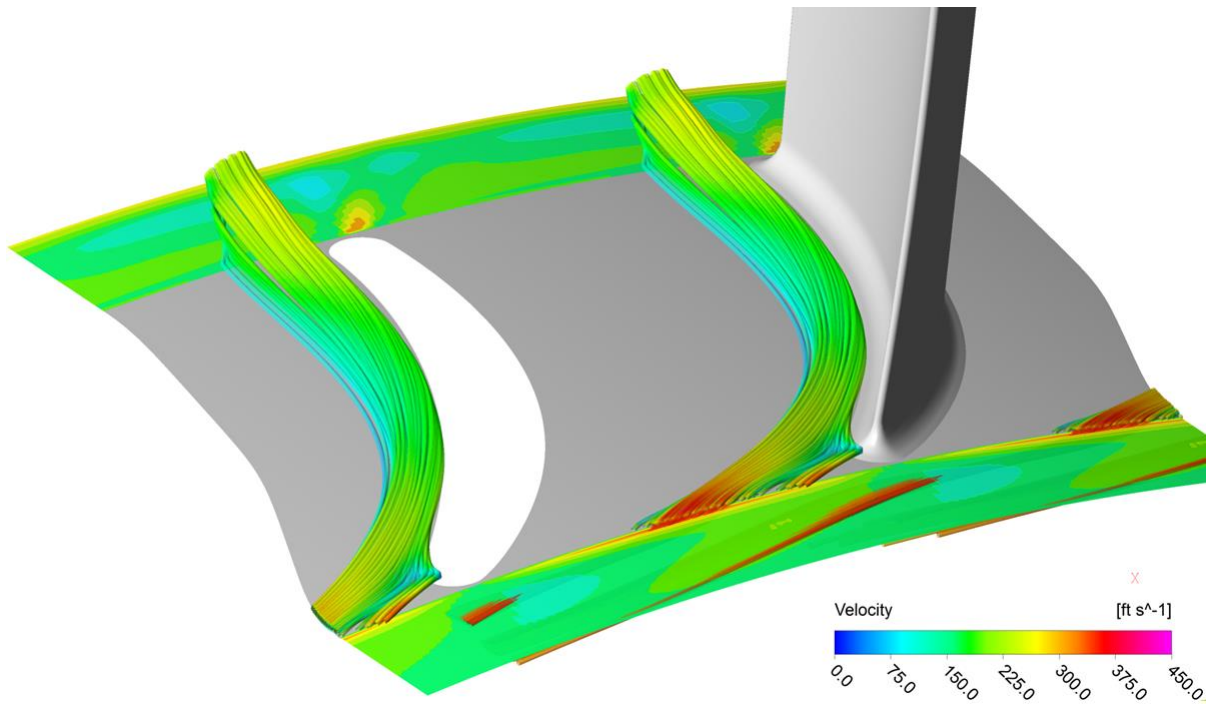


Figure 3.23: Velocity streamlines emerging from cavity outlet well and progressing through the stator passage for 0.250% span clearance case.

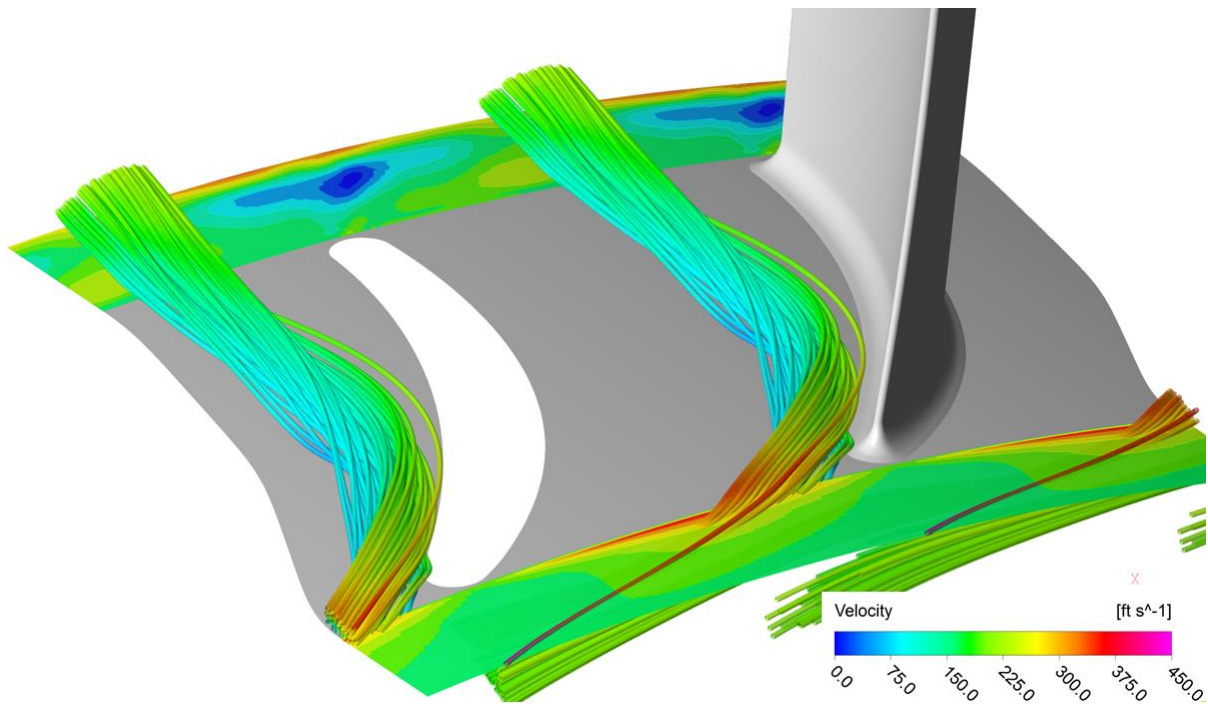


Figure 3.24: Velocity streamlines emerging from cavity outlet well and progressing through the stator passage for 1.000% span clearance case.

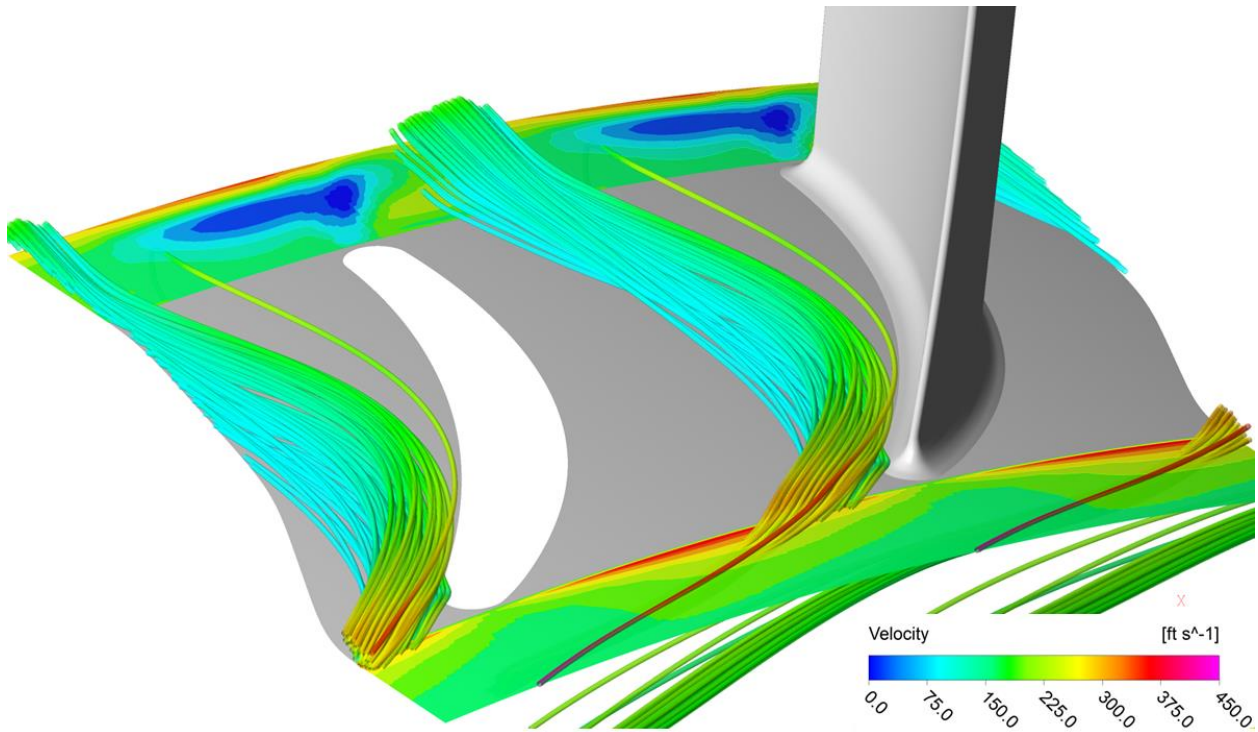


Figure 3.25: Velocity streamlines emerging from cavity outlet well and progressing through the stator passage for 1.375% span clearance case.

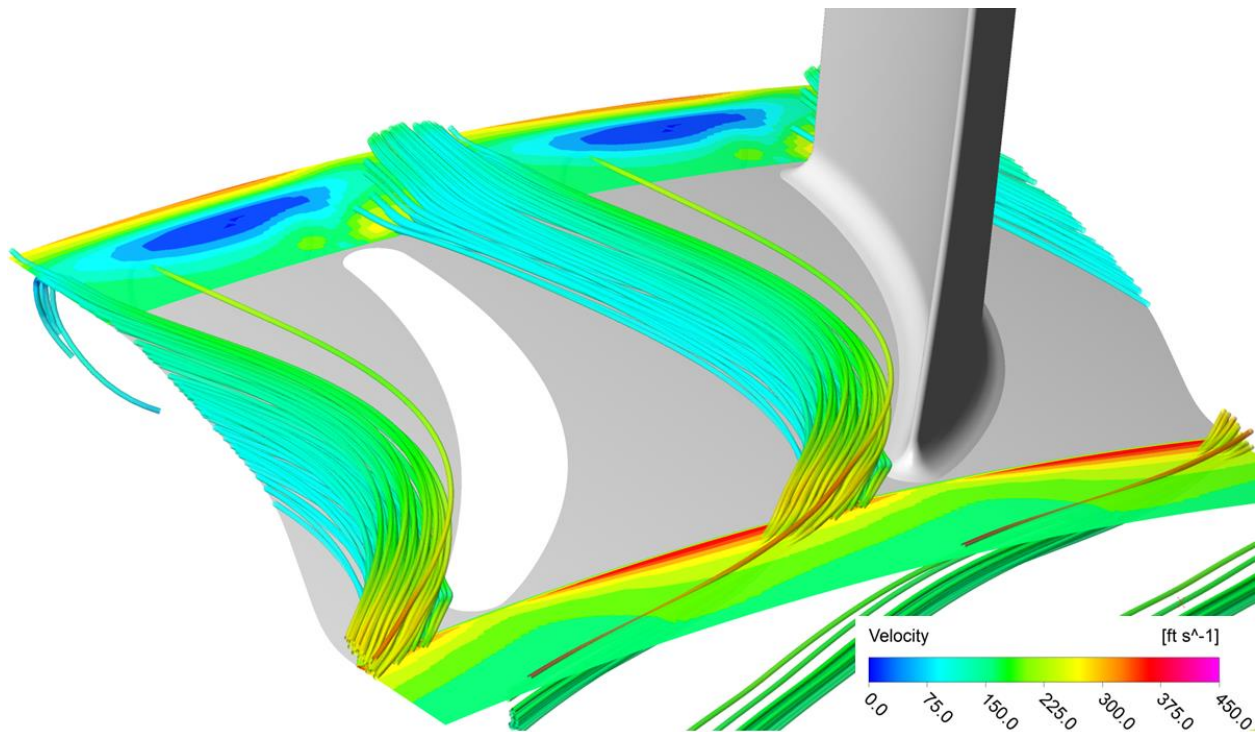


Figure 3.26: Velocity streamlines emerging from cavity outlet well and progressing through the stator passage for 1.750% span clearance case.

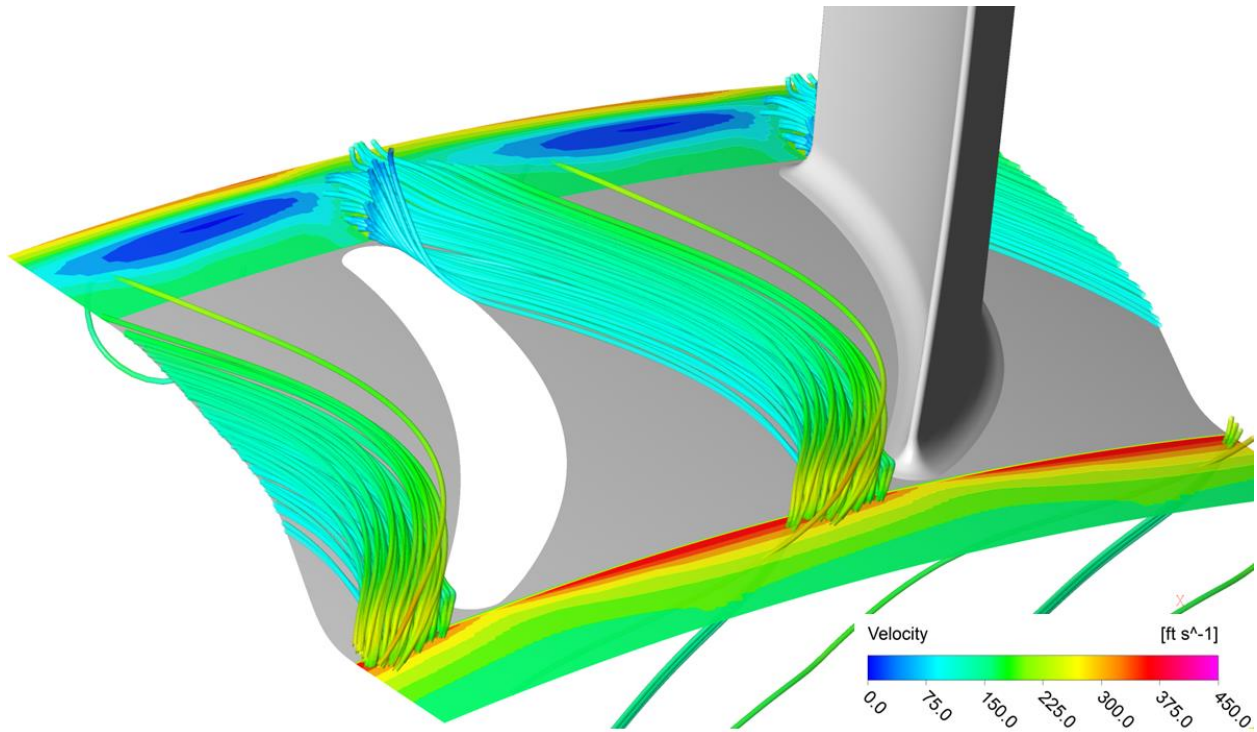


Figure 3.27: Velocity streamlines emerging from cavity outlet well and progressing through the stator passage for 2.500% span clearance case.

Hence, these studies show the importance of cavity leakage flow rate, total pressure, and circumferential velocity on the primary passage flow field and the compressor performance. These mechanisms allow for the aerodynamic optimization, but, in practice, must be balanced by the increase in windage heating associated with reduced cavity leakage flow rate and higher circumferential velocities. In the next chapter, the details of these flow parameters along with the momentum exchange mechanisms are utilized to investigate the flow structure and the windage effect in the cavity wells.

CHAPTER 4. CAVITY LEAKAGE FLOW CHARACTERISTICS IN STATOR WELLS

In order to fully understand the influence of leakage flow characteristics, cavity wells are analyzed further. Here, the stator cavity inlet and outlet wells are investigated to understand the cavity leakage flow path by exploring the meridional streamlines as well as axial, circumferential, and radial momentum variations in the cavity wells. The results of the parametric study with varying cavity seal clearance are extended to understand the windage effect as well. The stator cavity wells are analyzed individually first, then the rise in temperature and windage work as the flow progresses from the cavity inlet interface to the outlet interface are presented. Lastly, bulk cavity leakage flow parameters at the inlet and outlet cavity interfaces are summarized and linked with the re-ingestion analysis to explore the potential of excessive windage heating and its role in optimization.

4.1 Near-hub Flow Variations

4.1.1 Radial Variations

In this section, results acquired from the cavity are presented to understand the flow characteristics near the hub-cavity interfaces, especially the cavity and primary flow interactions as the flow is drawn into and pushed out of the cavity wells. Figures 4.1 and 4.2 show the radial variations in major parameters near the hub-cavity interface. The total pressure profiles in Figure 4.1 indicate a loss in total pressure across the labyrinth seals as the level of total pressure in the upstream cavity was less than in the downstream cavity. Moreover, the circumferential velocity profiles in Figure 4.2 show that tighter clearances have a higher circumferential velocity as air enters the cavity. As observed in the previous section, large clearances increase the amount of blockage and loss near the hub. These radial profiles further suggest that large clearance indicate an increase in the mass flow rate through the cavity and a reduction in circumferential velocity. This injection of slow circumferential momentum near the hub reduces the incidence at the stator leading edge as seen from the absolute flow angle profiles. Therefore, the circumferential velocity, which is inherently dependent on the labyrinth seal clearance, has a major influence on the primary passage flow field near the hub and can greatly influence the aerodynamic design. The cavity

leakage fluid for the 1.75 percent span clearance case increases from 0.05 to 0.15 circumferential velocity ratio as the flow travels past the rotor ledge and radially inwards from 0 to -15 percent span. The leakage fluid exits at 0.30 circumferential velocity ratio as observed in the rotor 1 exit profile at -15 percent span, which is double the circumferential velocity from the stator 1 exit profile. Therefore, the magnitude of the circumferential velocity at -15 percent span at stator 1 exit shows that nearly half of the energy added to the injected fluid by the rotor drum is performed by the downstream rotor ledge before the flow reaches the downstream cavity volume as observed by the magnitude of the circumferential velocity at -15 percent span at rotor 1 exit. The remaining work input is divided by the downstream cavity well and the labyrinth seal teeth. The circumferential profiles show that almost no energy is added to the flow by the upstream cavity well until the flow encounters the mirrored rotor ledge at the upstream location. This phenomenon has been observed a few times in literature (Wellborn, 2001; Heidegger, 1996) but the mechanism causing this effect are largely unexplored. Due to the importance of circumferential momentum on aerodynamic design, the mechanism behind the development of circumferential velocity as the cavity leakage flow progress through the cavity is important to understand for aerodynamic optimization of the stator blade as well as the cavity geometry. This mechanism is an effect of the flow path chosen by the cavity leakage flow and is explored in detail in the axial variations section of this chapter.

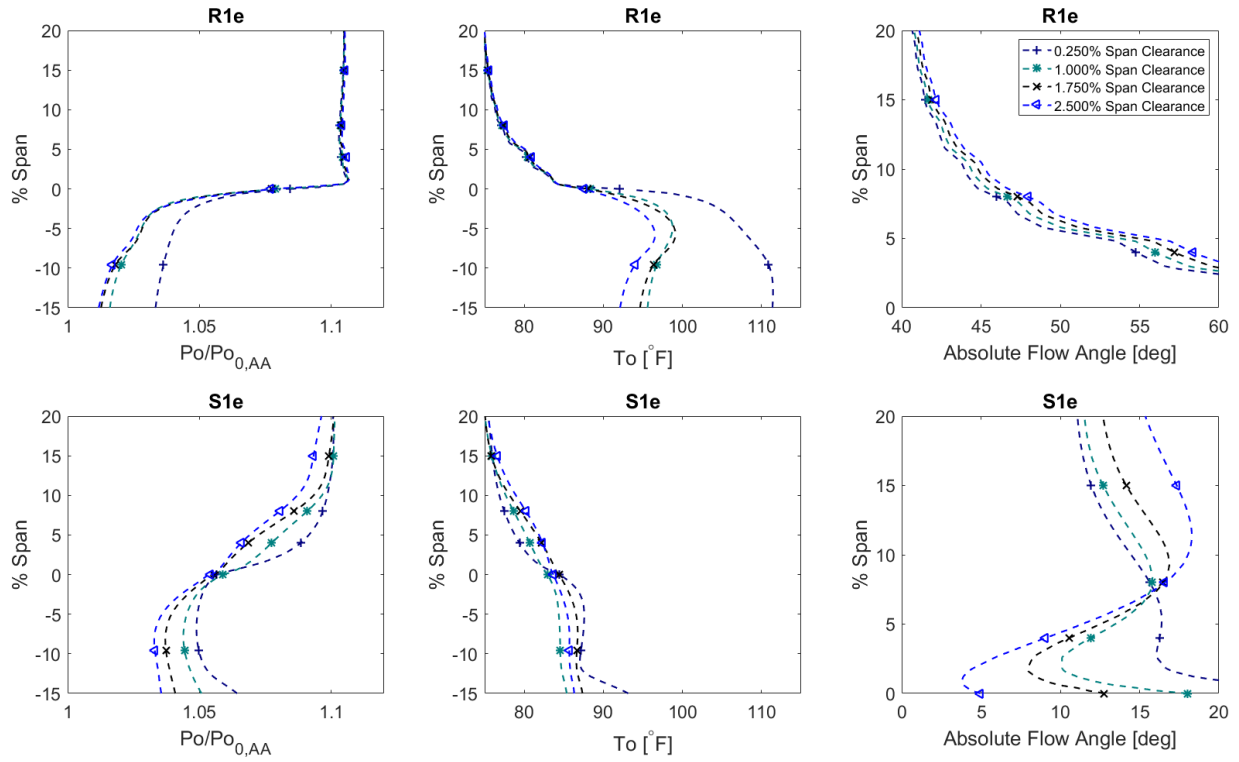


Figure 4.1: Total Pressure, Total Temperature, and Absolute Flow Angle radial profiles comparison of varying seal clearance near-hub and plunged into the cavity wells.

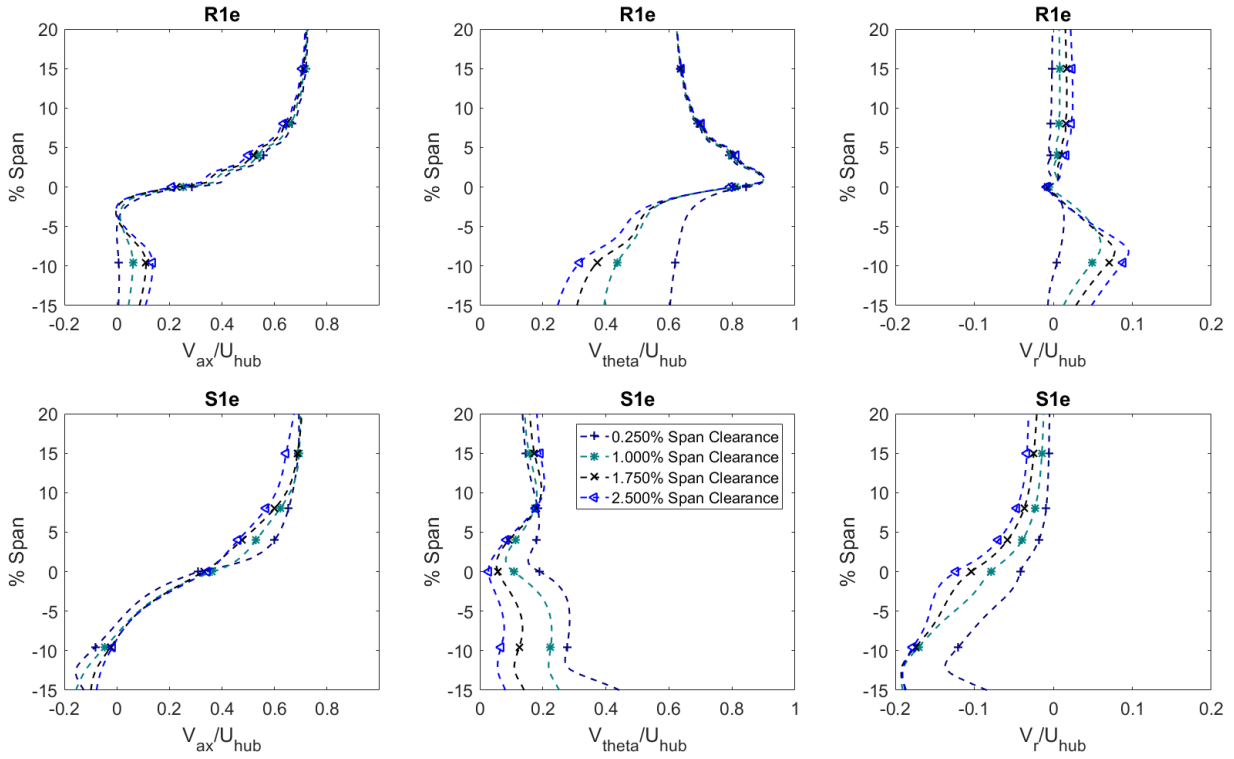


Figure 4.2: Axial, Circumferential and Radial Velocity profiles comparison of varying seal clearance near-hub and plunged into the cavity wells.

Here, axial and radial velocity differences have little significance for understanding the flow physics of the cavity leakage flow as the bulk flow is changing its direction by rotating 180 degrees to flow in the direction of the pressure differential. Therefore, the flow entering at stator 1 exit exchanges almost all axial momentum to radial momentum as it rotates 90 degrees to flow into the cavity and then exchanges radial momentum back for axial momentum for the remaining 90-degree rotation. Nevertheless, the differences in circumferential velocities along with a combination of the amount of leakage flow rate for varying labyrinth seal clearance coincide with large differences in the cavity temperature. Therefore, these combinations can heavily influence mechanical design which is discussed in the windage heating section. Overall, the data suggest, and as observed in literature (Wellborn and Okiishi, 1999; Wellborn 2001; Heidegger, 1996), that as the leakage mass flow rate increases, the rise in total temperature also increases despite a decrease in the circumferential velocity acceleration.

4.1.2 Axial Variations

In addition to radial profiles, meridional streamlines show interactions at the hub-cavity interface. Figure 4.3 shows near-hub streamlines of all the cases. The simulations imply that the bulk of the flow enters or leaves the cavity near the downstream face of the gap. Moreover, the vortical flow structures at the inlet and outlet interfaces dominate the axial flow variations in the cavity wells. First, Figure 4.3 reinforces circumferential variations observed in the previous section. At the downstream cavity interface, flow enters the cavity at vane passage locations where hub corner separation and wakes are present. Therefore, reinforcing the observation that the secondary flows in the primary passage governed which fluid particles are ingested in the cavity. Furthermore, the existence of a large vortex at the upstream face of the downstream cavity interface causes majority of the flow to enter the cavity near the downstream face of the gap. At the upstream cavity interface, flow enters the primary passage at all circumferential locations except near the leading edge. While the vortical structure is small relative to the downstream cavity, there exists a vortical structure on the upstream face of the upstream cavity interface forcing the flow to exit near the downstream face of the cavity.

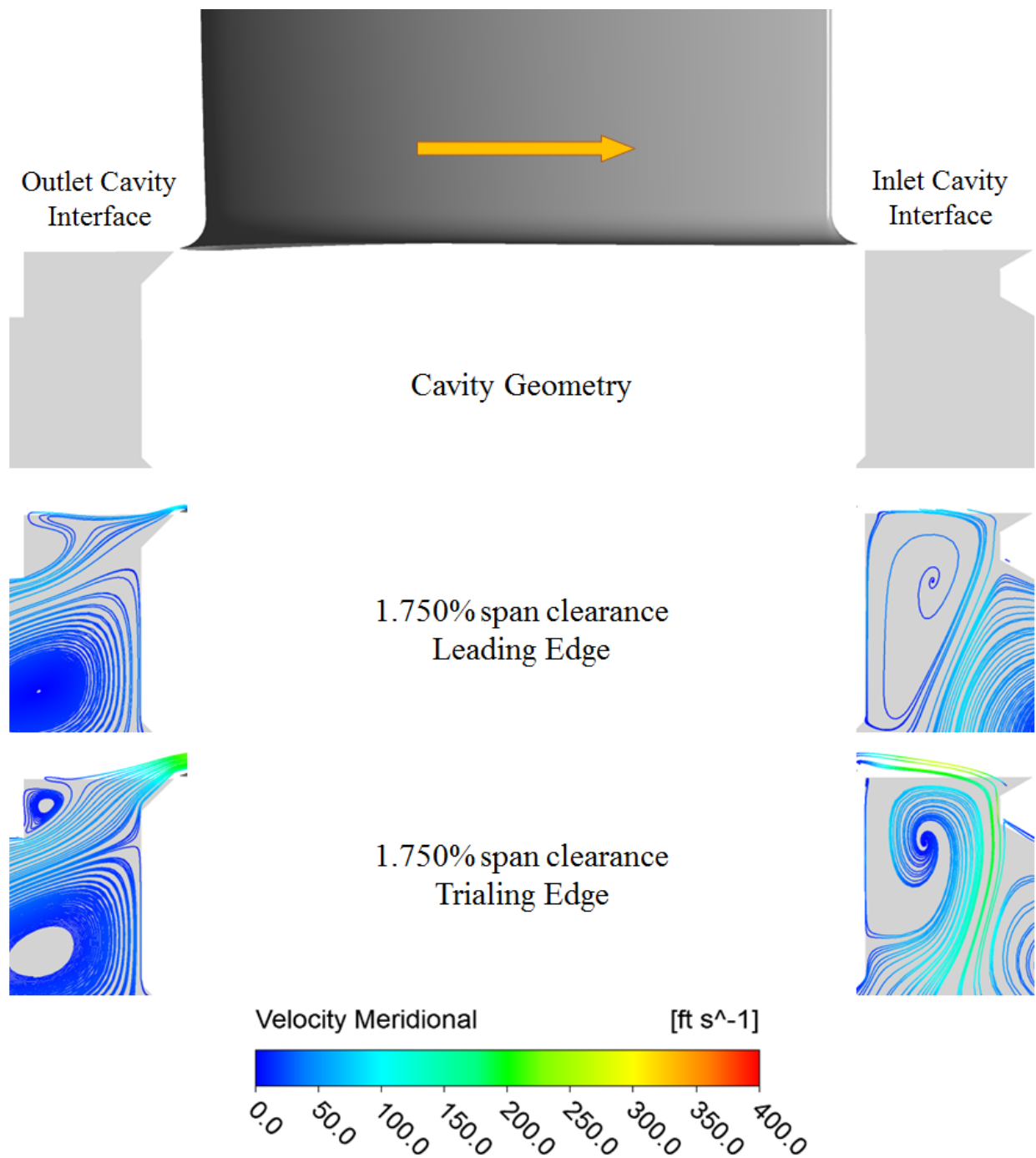


Figure 4.3: Meridional Streamlines near the inlet (right) and outlet (left) cavity interfaces of the 1.750 percent span clearance case at Leading Edge (Top) and Trailing Edge (Bottom).

Secondly, comparing seal clearance cases in Figure 4.4 and 4.5 provide insight into the position of the vortical structures as the varying labyrinth seal clearance allows different amounts of cavity leakage flow. At the downstream cavity interface, the vortical structure stretches across the gap as seal clearance becomes tighter allowing for less flow to enter the cavity. A similar observation is noticed at the upstream cavity interface, with the vortical structure on the upstream face increasing in size to restrict the exiting flow. Lastly, as observed in the radial profiles, large seal clearances tend to have a higher radial momentum which pushes the exiting flow more radially outwards compared to tighter seal clearance cases. High radial momentum along with more leakage flow and lower circumferential momentum for loose seal clearance cases all contribute to worsening near-hub performance and increasing the potential for hub corner separation.

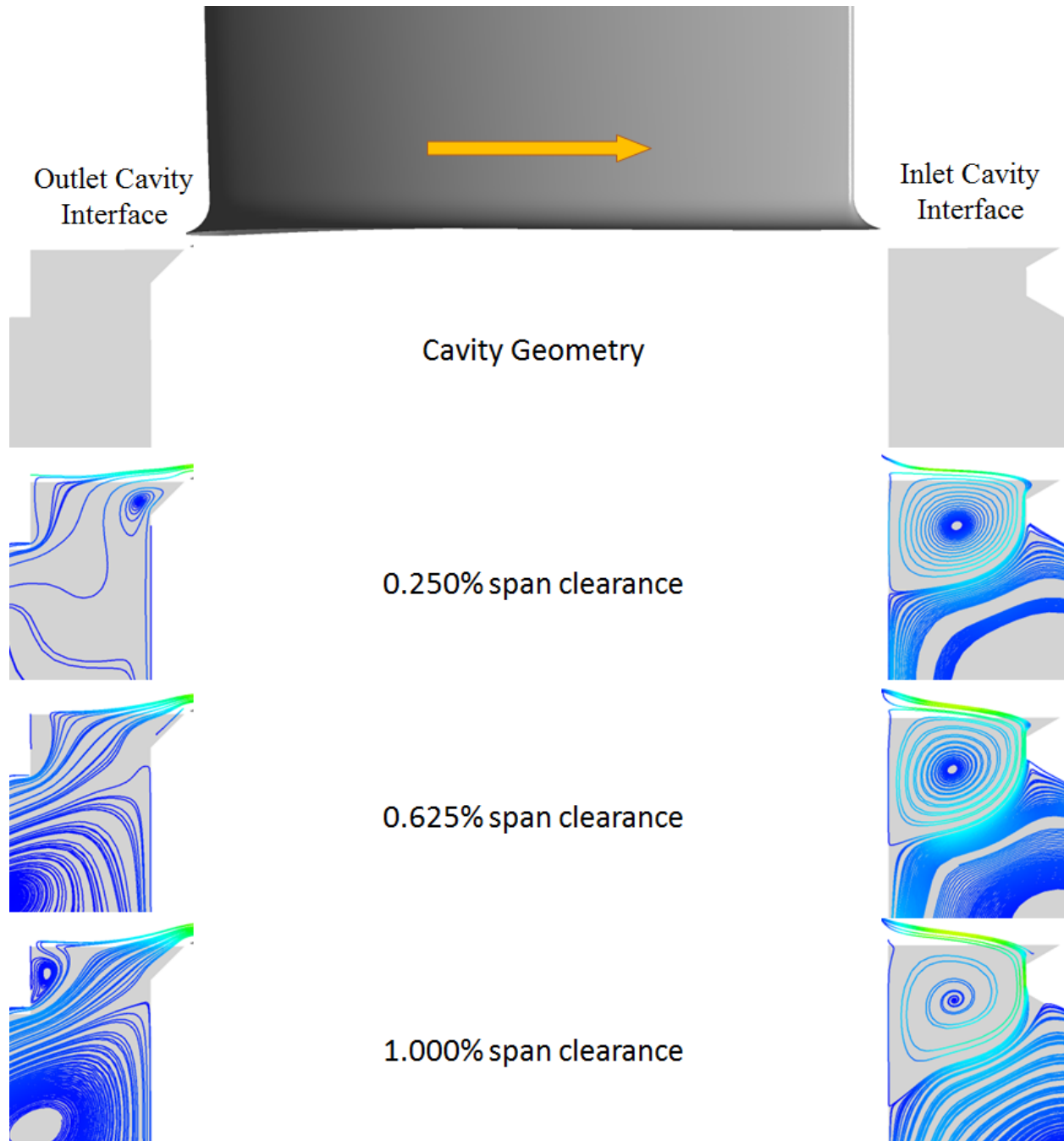


Figure 4.4: Meridional Streamlines near the inlet (right) and outlet (left) cavity interfaces for varying seal clearance cases at the trailing edge of the stator.

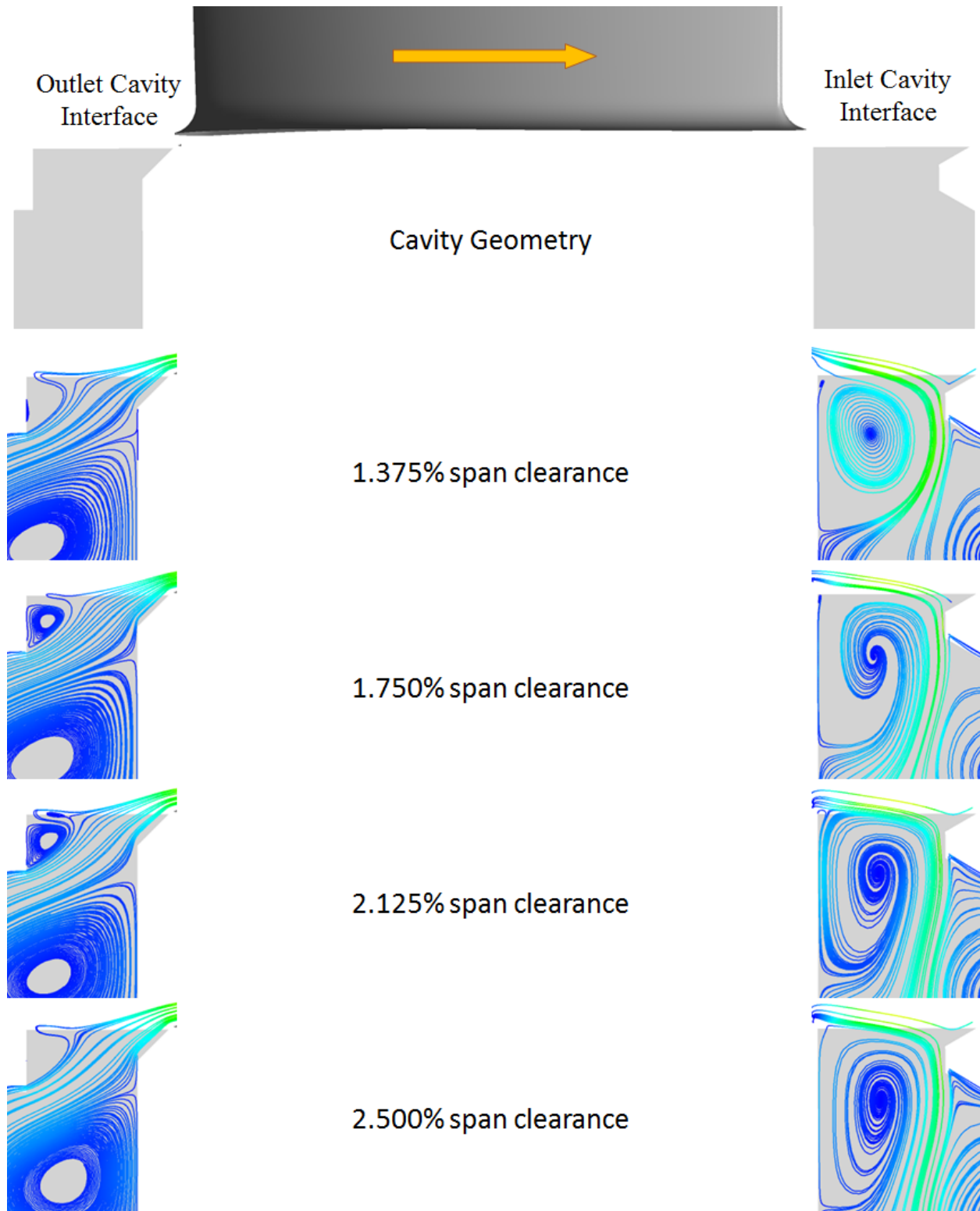


Figure 4.5: Meridional Streamlines near the inlet (right) and outlet (left) cavity interfaces for varying seal clearance cases at the trailing edge of the stator.

4.2 Cavity Leakage Flow Path

While overall variations near the hub-cavity interface investigations of linear cascades or standalone labyrinth seals have been presented in literature, flow path details of the cavity leakage flow have largely been unexplored. This section investigates the flow path details and its impact on the overall cavity leakage flow characteristics by separately examining the cavity inlet and outlet well.

4.2.1 Cavity Inlet Well

4.2.1.1 Meridional Velocity Streamlines

Here, the meridional streamlines presented earlier are extended to the entire cavity inlet well and displayed in Figure 4.6. In addition to the vortical structure at the upstream face, which causes the flow to enter near the downstream face of the inlet well, a larger vortical structure exists on the downstream face near the rotor landing. This vortical structure is larger when less flow, i.e. tighter clearance, is passing through the cavity. Moreover, this vortical structure along with the amount of leakage flow primarily determine the cavity leakage flow path as the flow progresses through the inlet well. In general, the simulations suggest that the size of both vortical structures in the inlet cavity well increase with tighter clearance creating a more arduous path for the cavity leakage flow to navigate. Most importantly, the vortical structures cause the flow to interact with the rotor drum near the hub-cavity interface where the flow enters and after the flow reaches the rotor landing. Here, interactions with the rotor drum determine the development of the circumferential velocity of the cavity leakage flow which is a crucial parameter in influencing the near-hub performance as previously discussed in the previous chapter. First, the quantitative details of the flow parameters are discussed for the baseline-cold clearance case to understand the variations in flow as the cavity leakage flow proceeds radially inwards into the cavity inlet well. Then, the effect of labyrinth seal clearance on these flow parameters is investigated to further understand cavity leakage flow characteristics in the cavity inlet well.

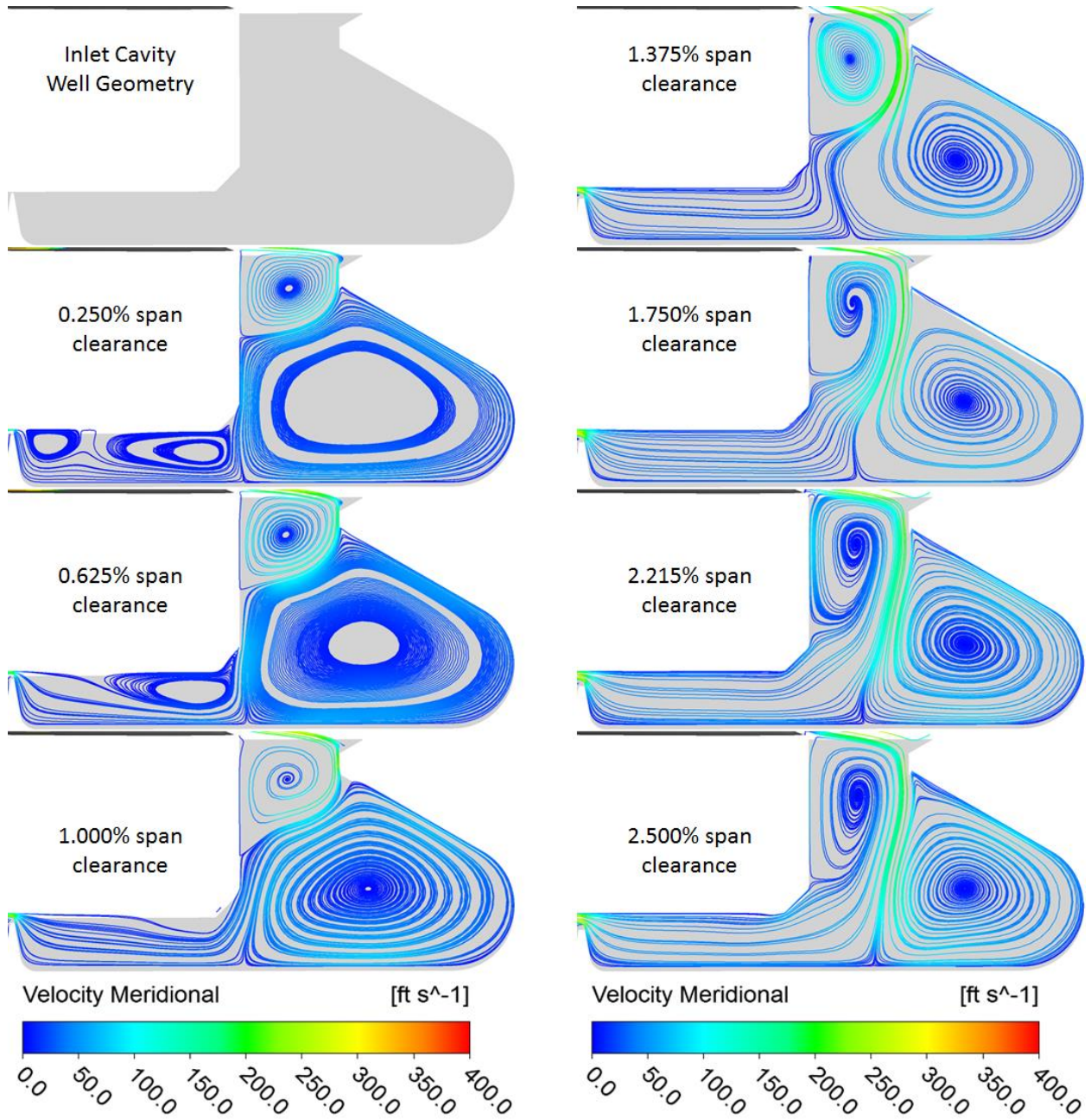


Figure 4.6: Meridional Streamlines in the inlet cavity well for varying seal clearance cases.

4.2.1.2 Radial Variations in Flow Profiles

Figure 4.7 shows how the cavity geometry is divided into a range of radius ratios and axial locations in order to investigate the flow parameters within the cavity wells. For a series of plots presented in this section, the abscissa is the local axial location, where 0 is the furthest upstream location of the cavity geometry and 1 is the furthest downstream location and holds a range of 0.50-1.00 to show the details in the inlet cavity well. The flow is moving in the opposite direction of the primary flow, therefore, the axial range of 0.75-1.00 is where the flow encounters the first two vortical structures presented in the prior section. First, Figure 4.8 shows the flow parameters at the cavity inlet interface. Here, the radial velocity profiles show where the fluid enters the inlet cavity well, with the maximum negative radial velocity at the corresponding axial location marking the radially inwards progression of the flow. For tighter clearance cases, the majority of the flow enters further downstream than larger clearances. The magnitude of the radial velocity increases with increasing seal clearances. On the other hand, the circumferential velocity profiles show increasing magnitude with tighter clearance. However, there is no clear trend in the total temperature profiles. Here, 0.25 percent span clearance case shows the hottest temperature, 1.00 percent span clearance shows the lowest temperature, and 2.50 percent clearance shows the second lowest temperature. This attributes to the re-ingestion discussed earlier, with the 0.25 percent span clearance case showing possibility for re-ingestion but the 1.00 percent span clearance avoiding the re-ingestion zone all together. Hence, the hotter fluid remains near-hub and arrives in the high negative radial velocity zone to get re-ingested into the cavity inlet well. Therefore, 0.25 percent span clearance case registers the hottest temperature, while 1.00 percent span clearance profile registers the lowest temperature.

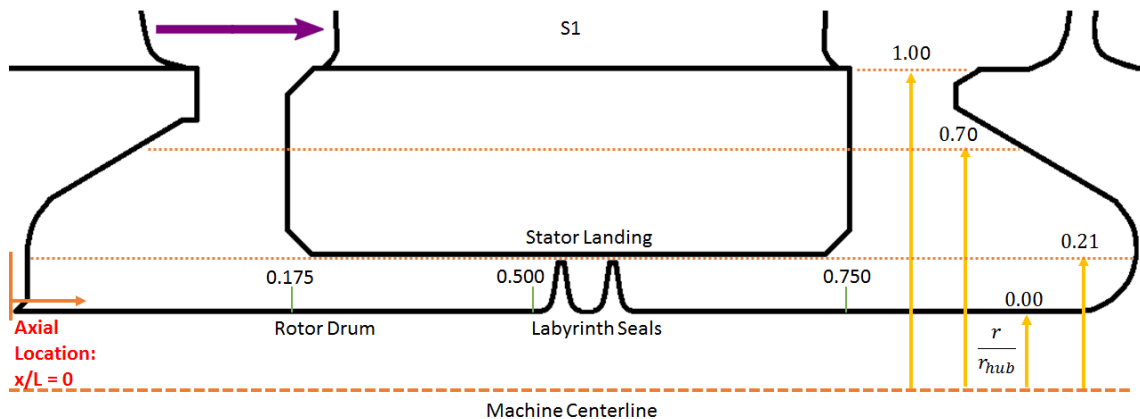


Figure 4.7: Datum definitions for the radial variation profiles in the inlet and outlet wells.

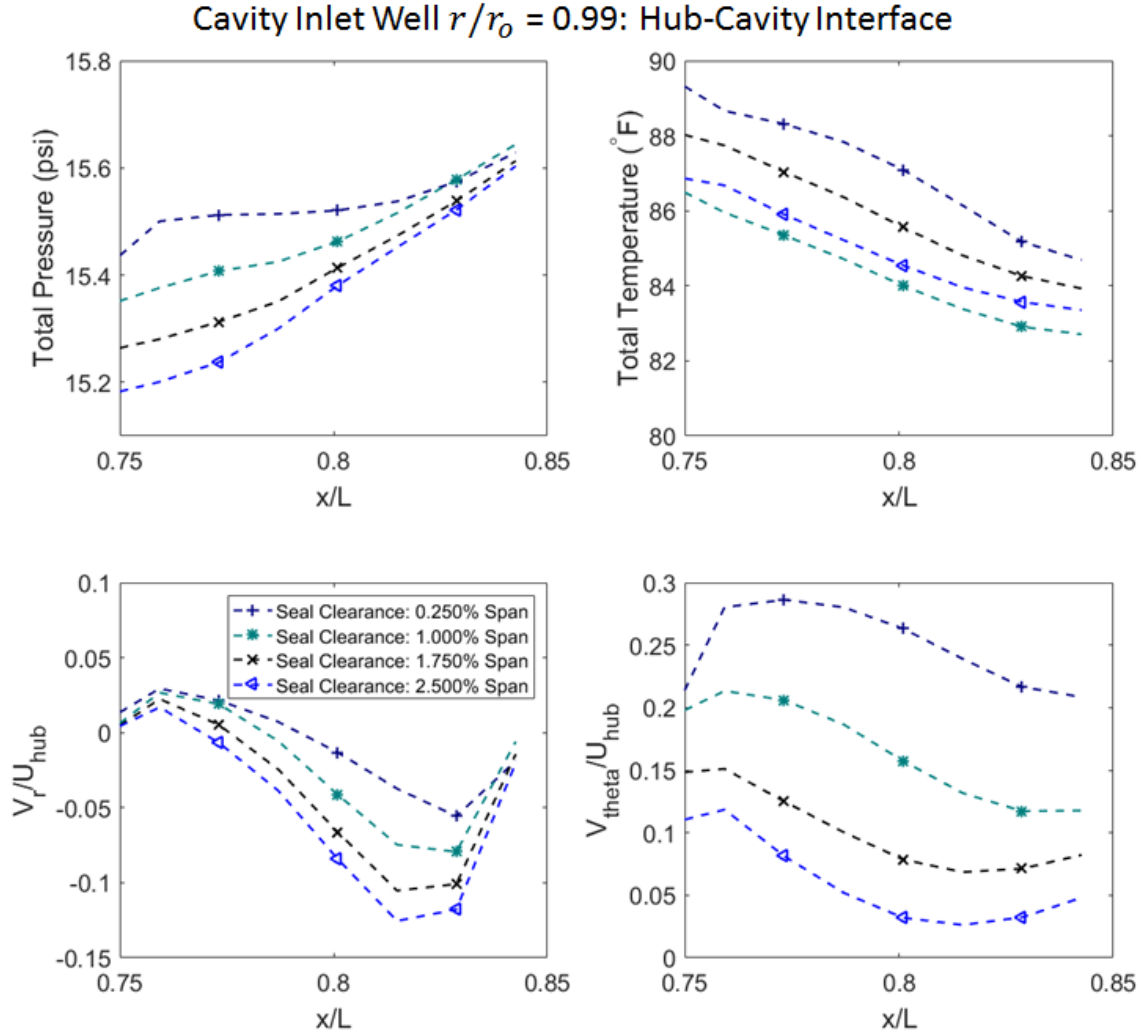


Figure 4.8: Radial variations in flow profiles at radius ratio 0.99 in the cavity inlet well.

Next, Figure 4.9 shows the flow parameters at the radial location which is directly below the rotor ledge. Here, the total pressure profiles show a sharp decline in pressure near the stationary side due to the presence of the vortical structure. While re-ingestion continues to dominate the order of total temperature profiles, the profiles show a decline in total temperature near the stationary surface where the vortical structure is present. This decline in temperature is consistent across seal clearance cases indicating that the vortical structure exists at a lower temperature than the cavity leakage fluid, which is moving radially inwards near the rotating surface. Similarly, the circumferential velocity profiles show that the vortical structures move at a lower circumferential velocity than the cavity leakage flow, with tighter clearances achieving higher circumferential

velocity. More importantly, comparing the magnitudes of circumferential velocity profiles across Figure 4.8 and Figure 4.9 indicates that the rotor ledge does a significant amount of work on the incoming cavity leakage fluid as it passes the rotor ledge. This is more evident when comparing the magnitude of total temperature profiles across Figures 4.8 and 4.9, indicating immediate rise in total temperature. Again, the magnitude of the radial velocity profiles at the corresponding axial location marks the radially inwards progression of the leakage fluid. As observed in the meridional streamlines of the inlet cavity well, the size and shape of the vortical structure forces the leakage fluid to carve a path closer to the stationary surface for tighter clearances, which is indicated again by the radial velocity profiles.

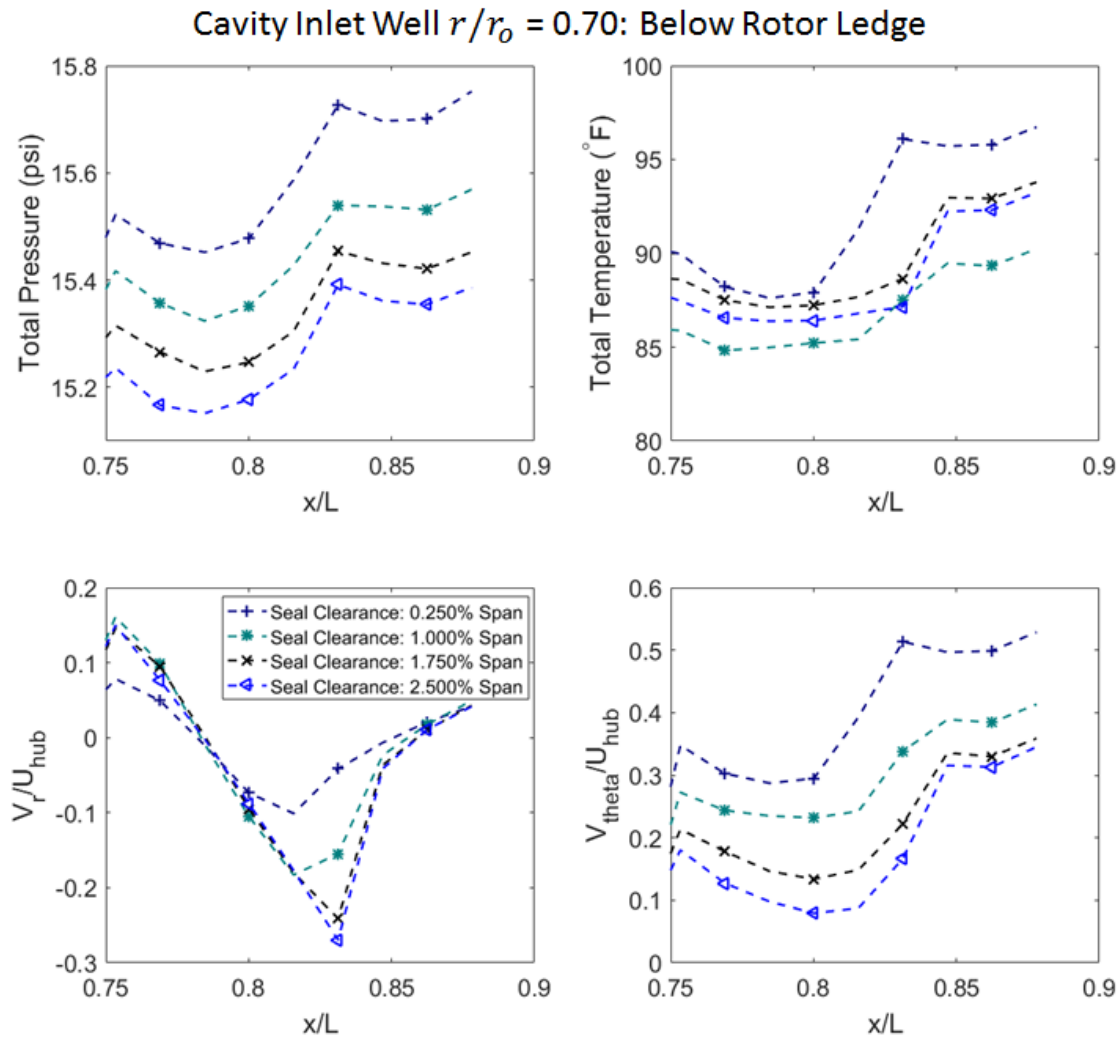


Figure 4.9: Radial variations in flow profiles at radius ratio 0.70 in the cavity inlet well.

Figure 4.10 shows the flow parameters at the radial location in between the labyrinth seal teeth and the stator landing. First, the total pressure profiles show the losses in pressure as the flow progresses from the inlet cavity well to the labyrinth seal. Here, the tightest clearance corresponds to the maximum total pressure, which represents minimum leakage flow rate. The peaks and corresponding axial locations in radial velocity profiles tracks where the incoming flow is moving radially inwards. These axial locations are more accurate representation of the flow path observed in the meridional streamlines presented earlier. For instance, the tightest clearance moves radially inwards closest to the stationary face as opposed to the largest clearance. Most importantly, the development of circumferential velocity as the flow progresses from the inlet well towards the labyrinth seals is also displayed in Figure 4.10. The tighter clearances show higher circumferential velocity for the cavity leakage flow. This observation also holds for vortical structures as tight clearance cases have larger vortical structures which, in turn, have higher circumferential momentum. Although, the flow path of the tighter clearance case is closest to the stator landing resulting in a lower circumferential momentum transfer for the flow exiting the inlet well at axial location of 0.75. Nevertheless, due to less leakage flow rate and a flow path closer to the rotor drum before the labyrinth seal (axial location 0.50-0.75), the leakage fluid regains circumferential momentum quicker than any other large clearance cases.

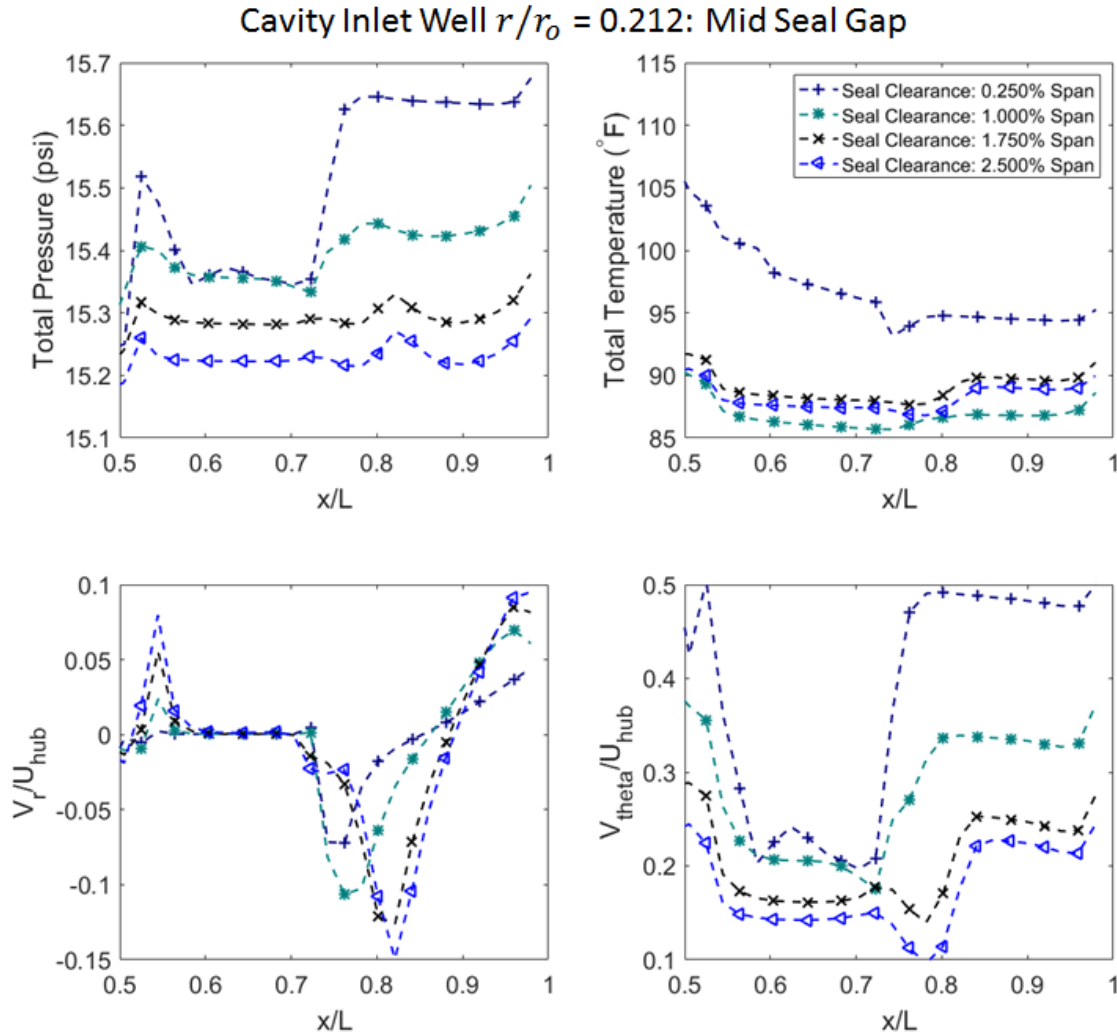


Figure 4.10: Radial variations in flow profiles at radius ratio 0.212 in the cavity inlet well.

In Figure 4.9 the vortical structure existed at a lower circumferential velocity than the cavity leakage fluid because it was closer to the stationary surface, but in Figure 4.10 the vortical structure exists at a higher circumferential velocity because it is closer to the rotor drum. This suggests that the vortical structure does not negatively impact the development of circumferential momentum as the entire vortical structure rotates with the same momentum, rather the cavity leakage flow path being in direct contact with the stationary surface hinders the transfer of circumferential momentum. This is evident when comparing the magnitude of circumferential velocity in Figure 4.10 and Figure 4.11 as the flow reaches the section before the labyrinth seal in the axial range of 0.50-0.75. This section is devoid of any vortical structure as the flow progresses

between the rotor drum and the stationary stator landing surface. The circumferential velocity profiles, when compared across Figures 4.10 and 4.11, show the transfer of viscous work from near the rotor drum to radially outwards with the profile closest to the rotor drum showing the most circumferential velocity. This transfer of momentum drops drastically from profiles of radius ratio 0.01 to 0.212. More importantly, comparing the magnitude of total temperature profiles across Figures 4.10 and 4.11 shows a steady rise in temperature due to frictional heating between the stator landing and the cavity leakage fluid. Here, the profiles near the rotor drum report the highest temperatures indicating that the rotor drum surface is a critical component for mechanical considerations. Lastly, the immediate rise in radial and circumferential velocity as well as the drop in total pressure near the local axial location of 0.5 indicates the flow interacting with the first labyrinth seal as the flow prepares to pass through the labyrinth seal and enter the outlet cavity well. As the flow approaches the labyrinth seals, the temperature rises suddenly suggesting the labyrinth seal teeth being subject to heating and thermal stresses. For all cases, regardless of re-ingestion, the rise in total temperature near the labyrinth seal is as high as 10 °F hotter than the fluid in the cavity wells.

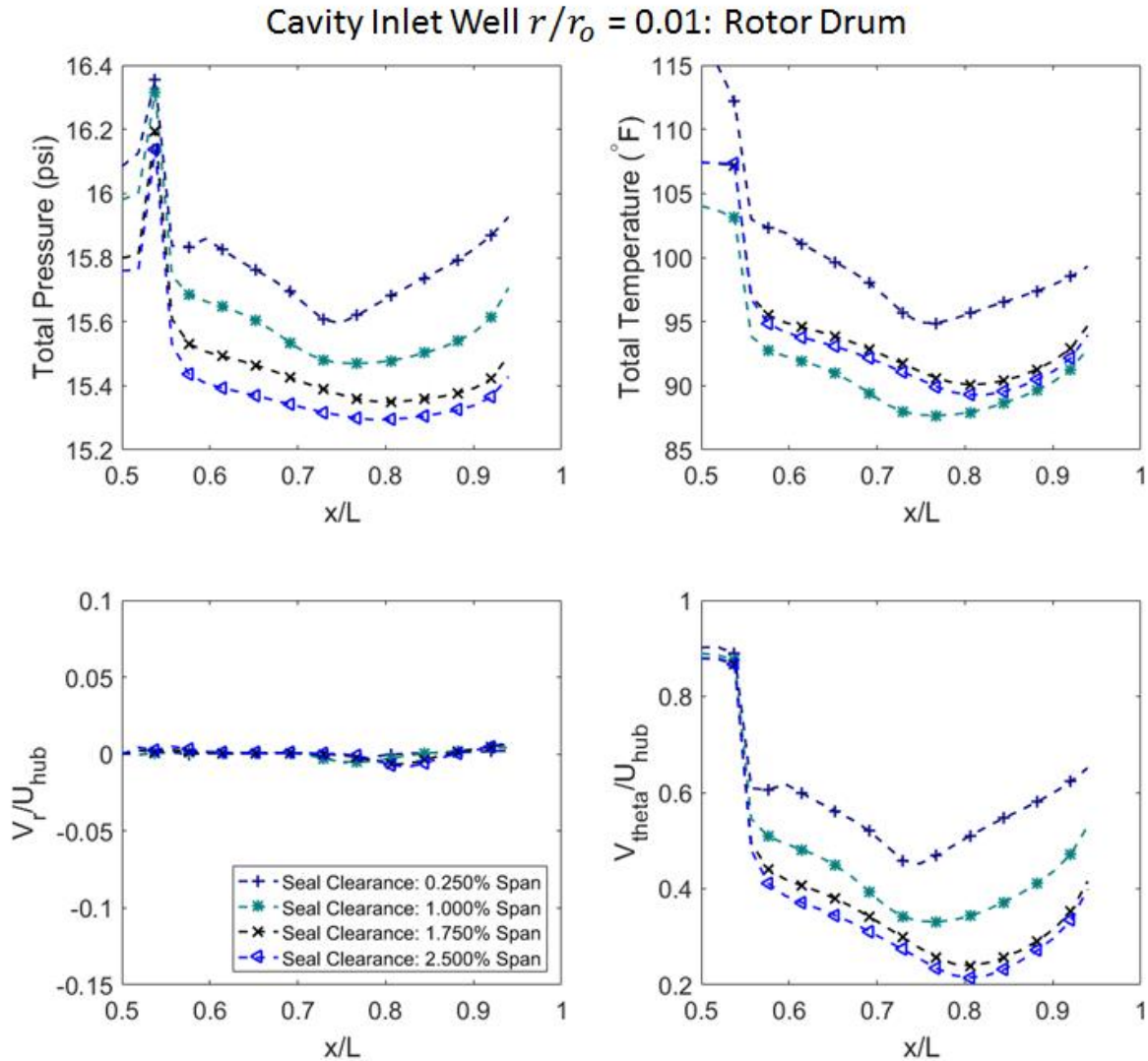


Figure 4.11: Radial variations in flow profiles at radius ratio 0.01 in the cavity inlet well.

These profiles show how the cavity leakage flow interacts with the vortical structures and the cavity geometry features. More importantly, these profiles show how the flow characteristics change with labyrinth seal clearance. In particular, the radial and circumferential profiles possess the ability to track the cavity leakage flow path and the viscous work being imparted on the flow, respectively. The total temperature profiles are also a good indicator of areas subject to heating and thermal stresses, which, in this case, are the rotor drum and the labyrinth seals as they indicate hotter overall temperatures than the rest of the geometry. This allows designers to not only predict the flow path and investigate the development of circumferential velocity and temperature in the

cavity leakage fluid but also employ changes to the cavity geometry for optimization. In the next section, a similar analysis approach is undertaken to investigate the flow characteristics in the cavity outlet well.

4.2.2 Cavity Outlet Well

4.2.2.1 Meridional Velocity Streamlines

Figures 4.12 shows the meridional streamlines for the cavity outlet well. As the flow exits the labyrinth seals constriction, a wide vortical structure forces the leakage flow to travel along the stator landing. The simulations suggest these vortical structures are radially taller and axially narrower with tighter clearance. Therefore, majority of the leakage flow will travel closely along the stator landing but for a shorter distance because the vortical structures are narrower for tighter clearance when compared to large clearance cases. Next, a large vortical structure in the cavity outlet well forces the leakage flow to transition towards the rotor drum and follow the rotor drum geometry curvature until the leakage flow exits to the primary passage. This vortical structure also increases with tighter clearance, forcing the flow path to be closer to the rotor drum which aids in the development of circumferential momentum.

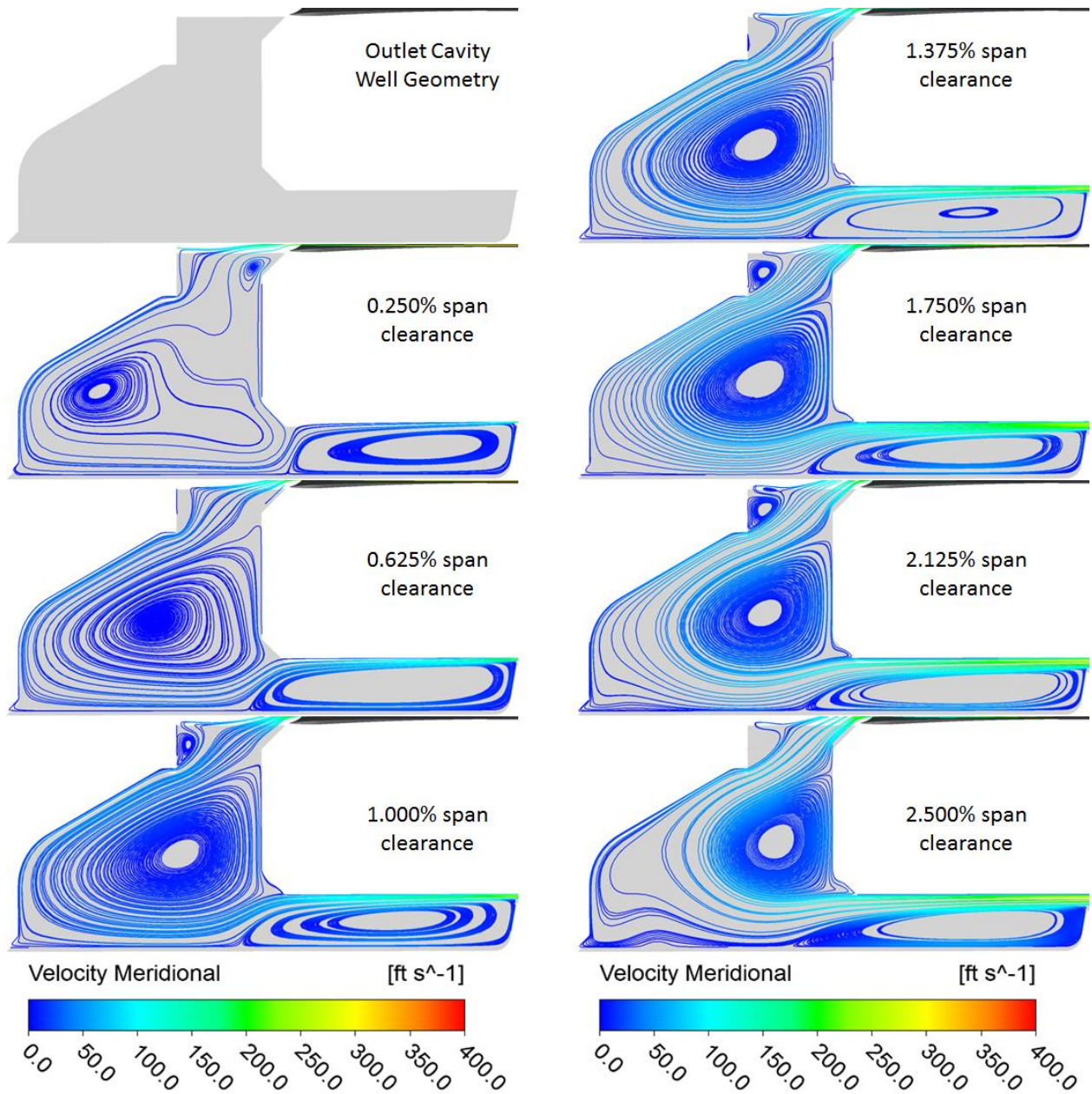


Figure 4.12: Meridional Streamlines in the outlet cavity well for varying seal clearance cases.

In general, the simulations suggest that the size of both vortical structures scale such that the distance travelled by the cavity leakage along the stator landing and the rotor drum changes. Tighter clearance cases show a more abrupt switch from stator landing to the rotor drum, while that transition is gradual for large clearance cases. Like the inlet cavity well, the interactions of these vortical structures, and the flow path along the rotor drum determine the development of circumferential velocity of the cavity leakage flow. Again, the quantitative details of the flow parameters for the baseline-cold clearance case in the cavity outlet well are discussed first, then the effects of labyrinth seal clearance are investigated.

4.2.2.2 Radial Variations in Flow Profiles

The plots presented to investigate the cavity outlet well follow the same format as Figure 4.7. As denoted by the streamlines, the flow enters the cavity outlet well near the stator landing, then proceeds to the rotor drum before traveling radially outwards towards the cavity outlet interface. Therefore, the Figures are presented in that order to convey information. First, Figure 4.13 shows the flow parameters of the cavity leakage fluid exiting the labyrinth seals and traveling along the stator landing with the focus on the axial range of 0.25-0.50. Here, the total pressure continues to drop to adjust with the upstream cavity pressure. The radial velocity profiles show that the flow continues to travel along the stator landing until axial location 0.25, after which the flow transitions radially inwards, i.e., towards the rotor drum. As long as the leakage fluid travels along the stator landing, the circumferential velocity continues to drop, and the total temperature continues to climb, as seen in the corresponding profiles. Here, profiles of the 0.25 percent span clearance case show large variations because of the development of a secondary vortical structure as observed in the streamlines of the cavity outlet well earlier. Nevertheless, the overall trends discussed are the same. Circumferential velocity continues to be the highest for tighter clearances because of the less amount of leakage flow rate and lower distance travelled along the stator landing before transitioning to the rotor drum. Lastly, the peaks in the axial range of 0.00-0.20 in radial velocity profiles tracks where the flow moves radially outwards after travelling along the rotor drum.

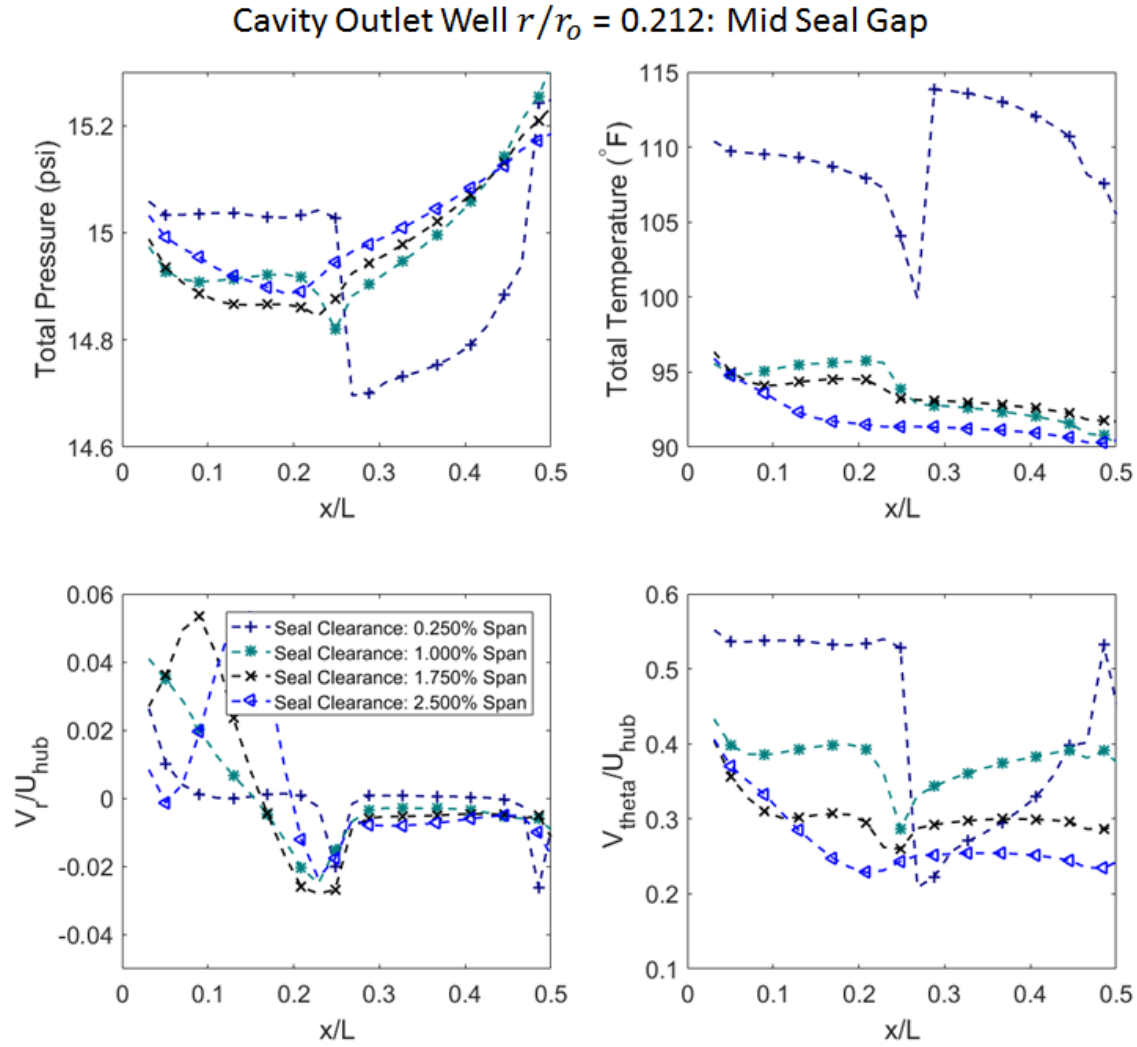


Figure 4.13: Radial variations in flow profiles at radius ratio 0.212 in the cavity outlet well.

Next, Figure 4.14 shows the flow parameters of the leakage fluid transitioning from the stator landing to the rotor surface in the range of 0.00-0.25. Circumferential velocity starts to develop once the flow transitions to the rotor drum. This is indicated by the increasing trend in the circumferential velocity profiles from axial location 0.25 to 0.00. Also, profiles near the rotor drum report the highest temperature. While temperature development in the cavity wells is largely non-existent in literature, some quantitative observations by Ozturk (1998) and Bayley (1994) noticed similar temperature developments. Especially, when the flow travels along the rotating rotor drum surface or when the flow experiences frictional heating along the stator landing in their standalone labyrinth seal investigations.

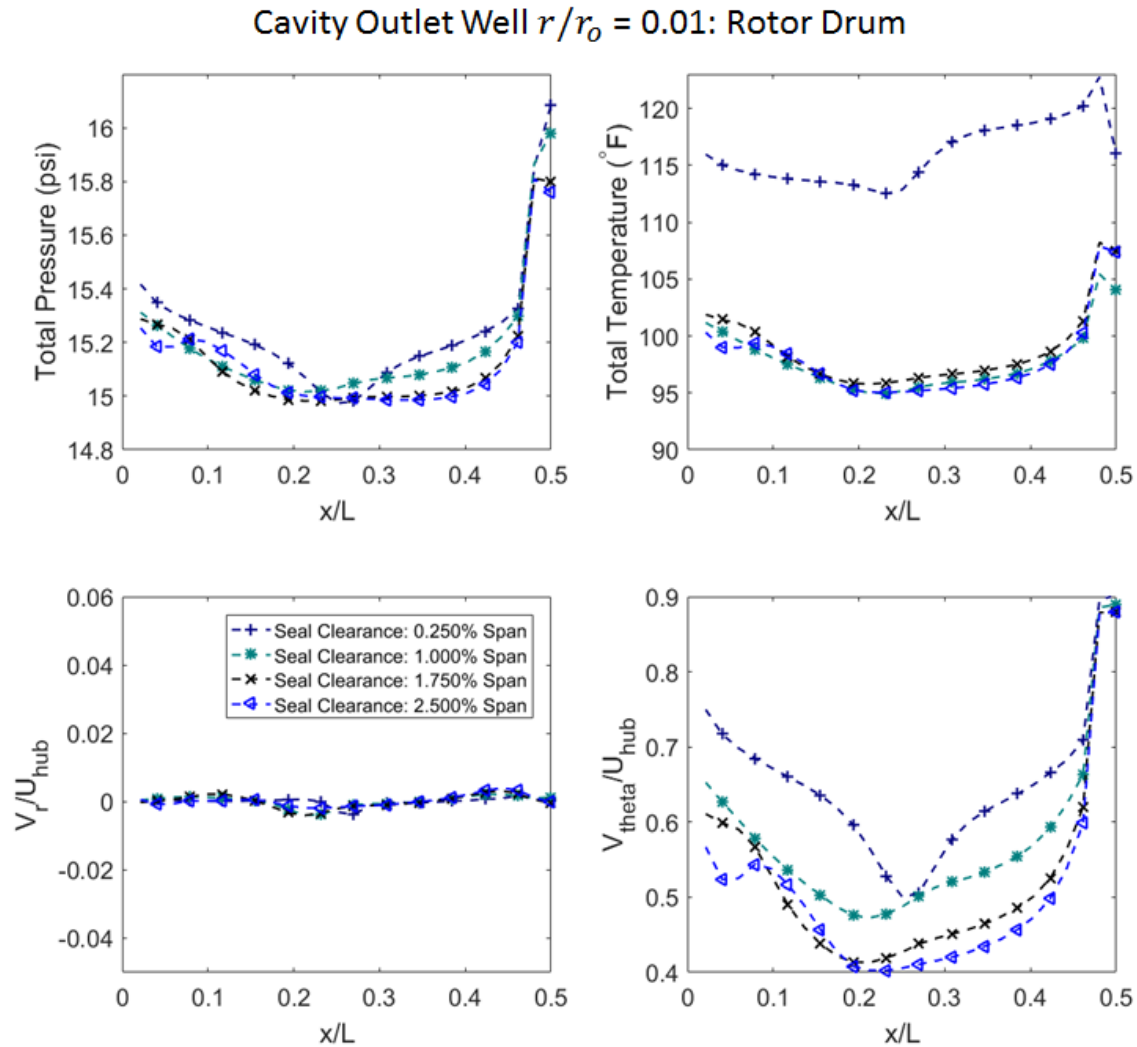


Figure 4.14: Radial variations in flow profiles at radius ratio 0.01 in the cavity outlet well.

These trends continue across seal clearances in Figure 4.15, which shows the flow parameters of the leakage fluid as the flow travels radially outwards towards the outlet interface. Higher radial velocity magnitudes near the rotor drum show that the leakage fluid continues to travel along the rotor drum surface as the large vortical structures occupy most of the outlet well. Due to the path along the rotor drum, the leakage fluid continues to maintain higher circumferential velocity and hotter temperature as it travels radially outwards. Lastly, Figure 4.16 shows the flow parameters as the leakage fluid exiting at the outlet interface. The radial velocity profiles show that the majority of the leakage flow exits near the downstream surface. The tighter clearances showing higher circumferential velocity and hotter temperatures for the flow exiting the cavity.

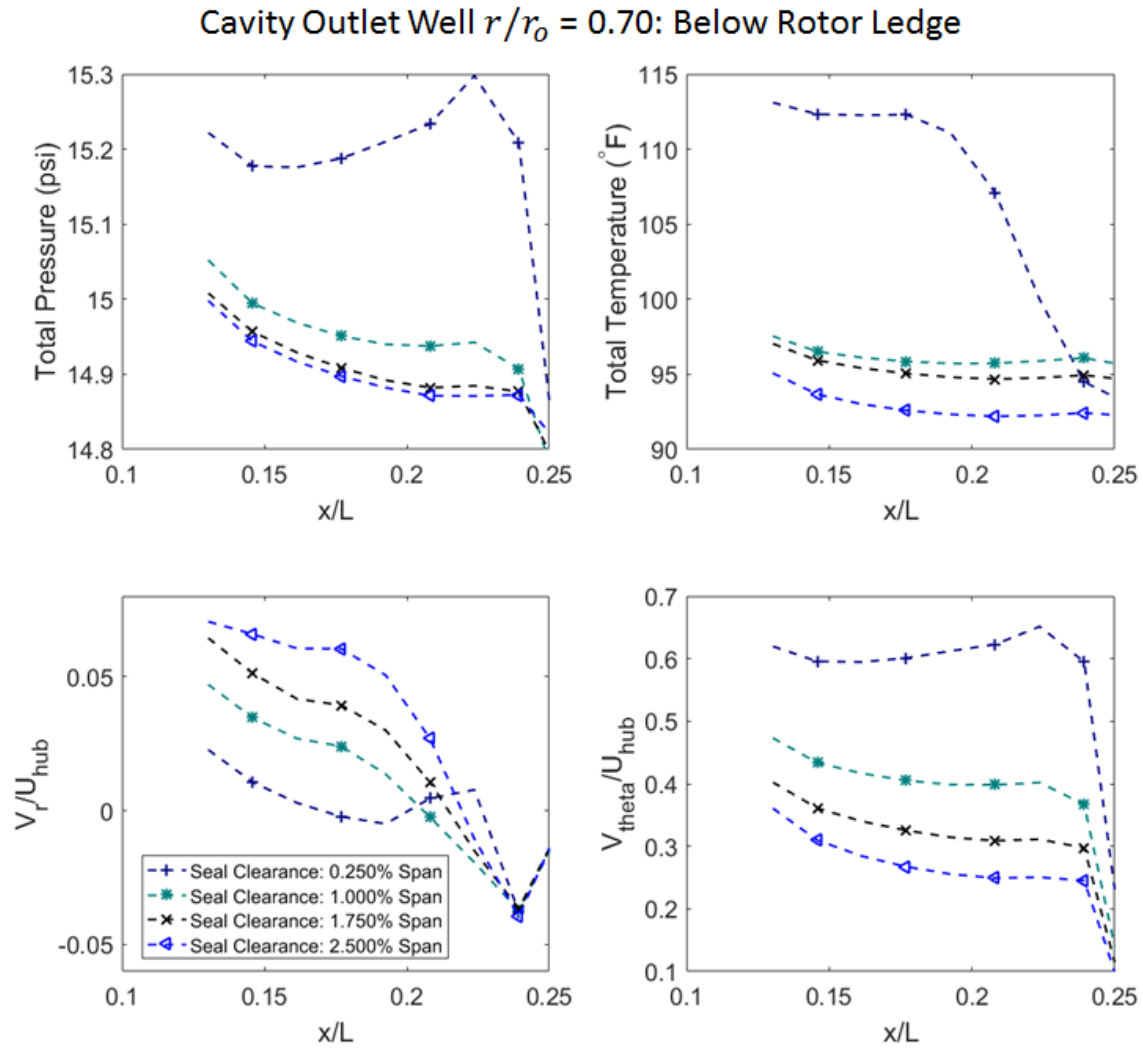


Figure 4.15: Radial variations in flow profiles at radius ratio 0.70 in the cavity outlet well.

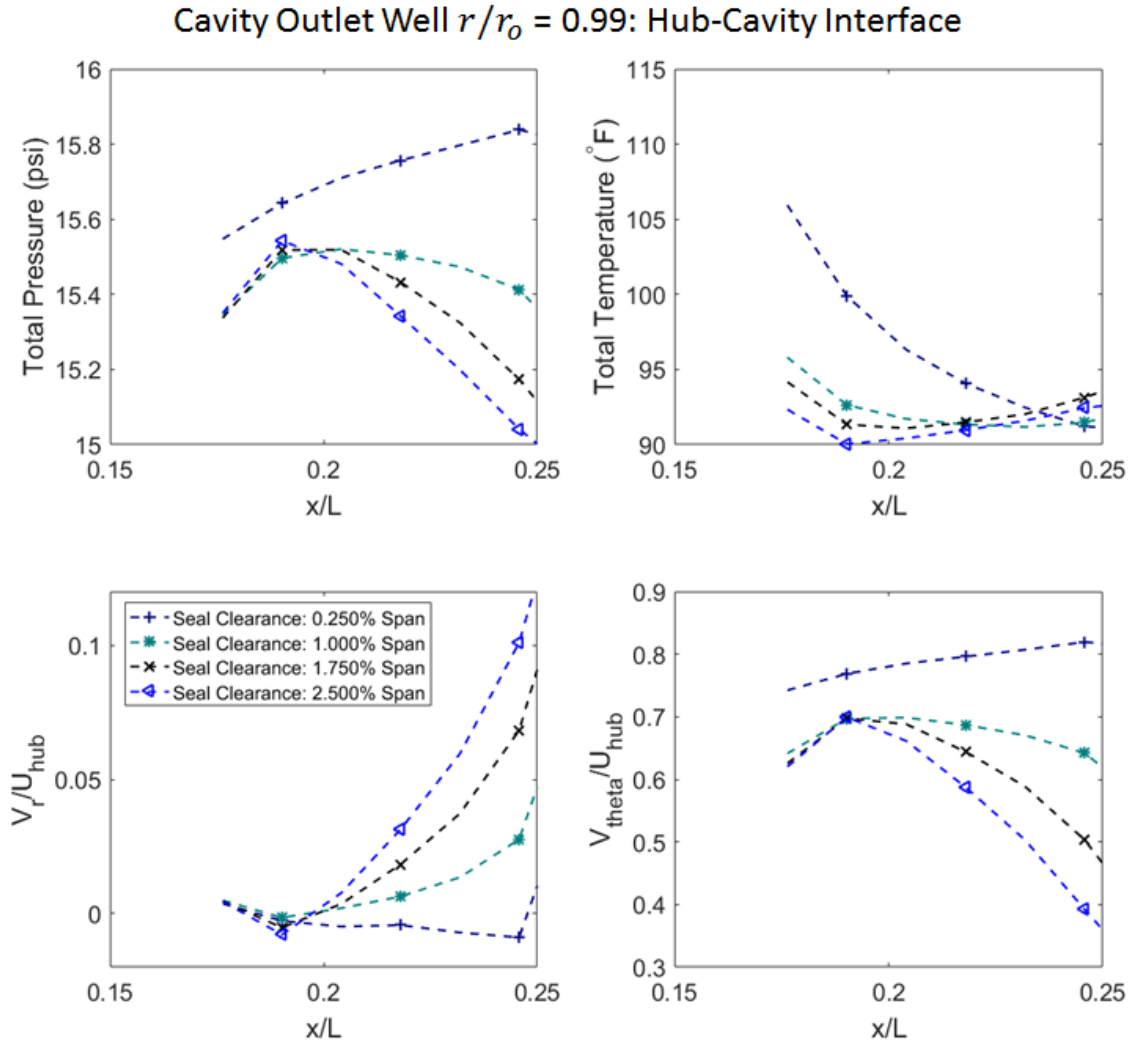


Figure 4.16: Radial variations in flow profiles at radius ratio 0.99 in the cavity outlet well.

All other radius ratio profiles for varying seal clearances cases of the cavity inlet and outlet wells can be found in Appendix A and Appendix B, respectively. Lastly, the profiles of radius ratio 0.212 traversing the inlet well, outlet well, and the labyrinth seal are presented in Figure 4.17. These profiles show the complete development of flow parameters across the stator cavity wells. The radial momentum peaks near axial locations 0.1 and 0.8 show flow entering and leaving the cavity wells, respectively. Other radial momentum peaks at axial locations 0.20 and 0.50 show the flow transitioning from the stator landing to rotor drum following the labyrinth seal, and flow entering the labyrinth seals, respectively. Most importantly, the circumferential velocity profiles show that the flow traveling near the stator landing or the rotor drum has a more significant impact

on the development of the circumferential momentum than the vortical structures. When the cavity leakage flow travels along the rotor drum as it progresses through the cavity, it attains more circumferential velocity regardless of the location of the vortical structure. These profiles also show the development of temperature as the cavity leakage fluid travels across the cavity geometry, with the re-ingestion evident in the 0.25 percent span clearance profile. For all cases, and at all radial locations, these figures show that the smallest clearance case leads to the greatest rise in temperature in the cavity well. Consequently, increasing the leakage flow through the labyrinth seals reduces the temperature rise through the cavity well. Nevertheless, the temperature profiles decrease for seal clearance case that avoids re-ingestion, suggesting an optimum case.

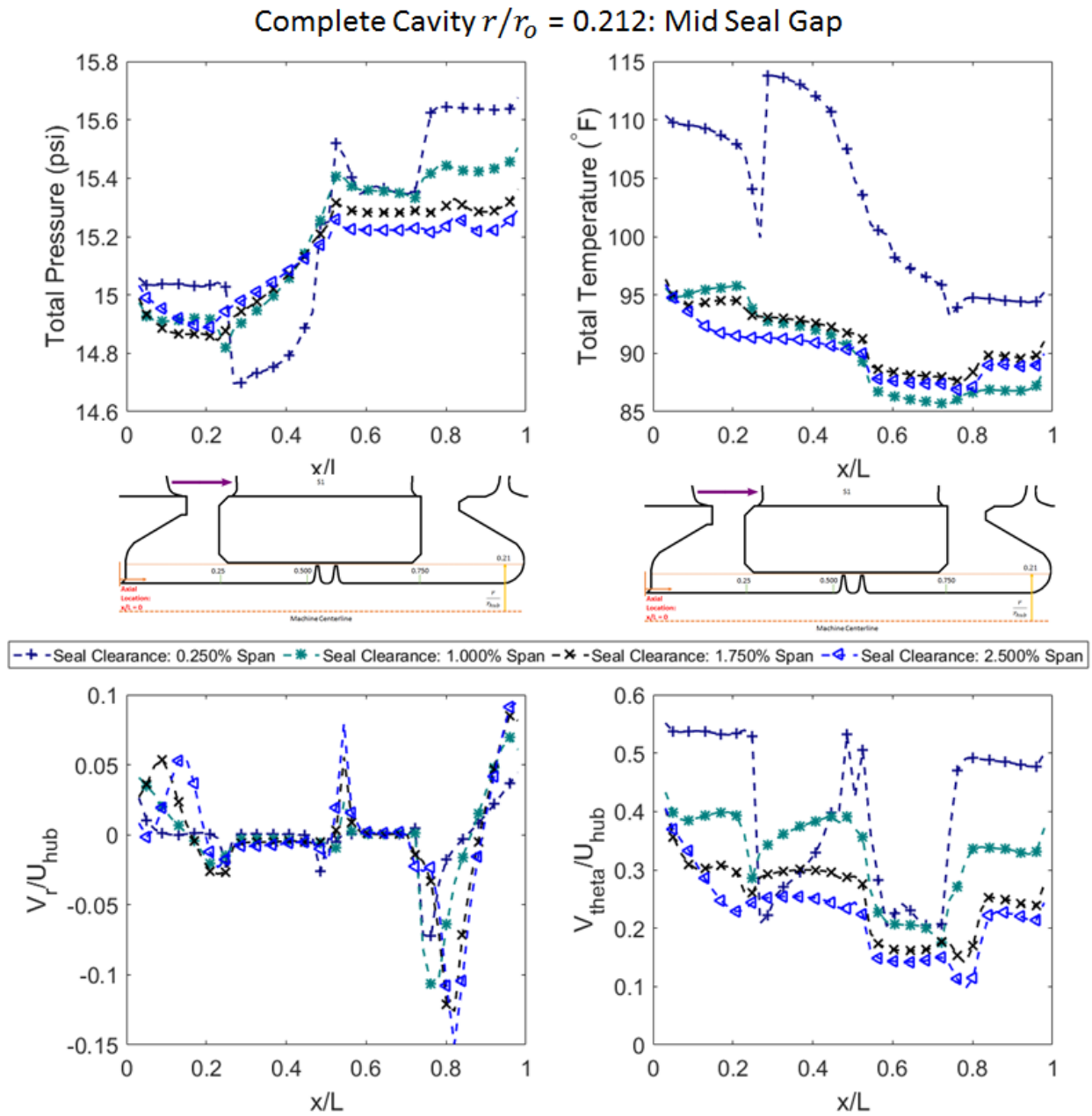


Figure 4.17: Radial variations in flow profiles at radius ratio 0.212 throughout the cavity well.

4.3 Windage Heating

4.3.1 Overall Temperature Rise

Figures 4.18 and 4.19 show the total temperature at the inlet and outlet cavity interfaces as well as the rise in total temperature. First, Figure 4.18 shows both incoming and outgoing leakage flow temperatures are higher for tighter seal clearances. The high temperatures correspond to the re-ingestion observed for tighter clearances. The seal clearance case of 1.0 percent span achieves the lowest temperature as it avoids re-ingestion. More importantly, as the seal clearance increases the temperatures reach an almost asymptotic value because increased flow rate at larger clearances makes momentum transfer more difficult resulting in lower temperatures. Therefore, for tighter clearance cases, which is a criterion for improved aerodynamic performance, will have higher cavity well temperatures as a result of less cavity leakage flow through the cavity. Then, the interdependence of circumferential velocity and total temperature is shown in Figure 4.19. The plot shows that tighter seal clearances achieve higher increase in circumferential velocity, but higher circumferential velocity also correspond to increased total temperature rise. Therefore, investigating circumferential velocity development is crucial for understanding the development of temperature in the cavity wells.

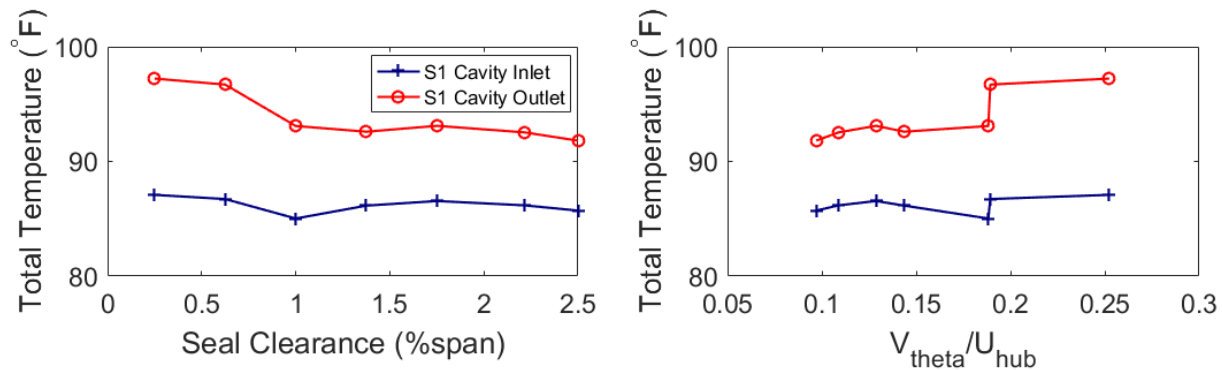


Figure 4.18: Changes in total temperature at the hub-cavity interfaces for varying seal clearance and inlet circumferential velocity.

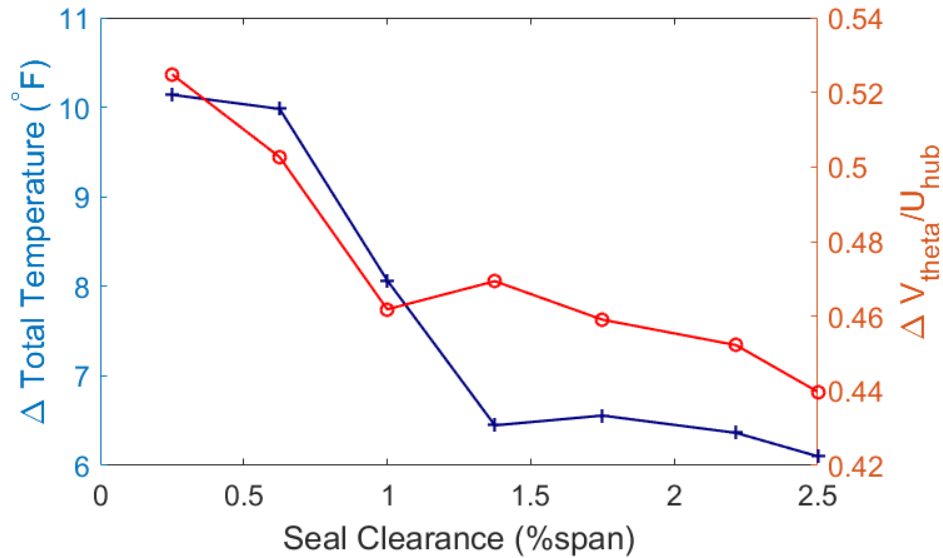


Figure 4.19: Change in total temperature inlet to outlet cavity interfaces for varying seal clearance and inlet circumferential velocity.

4.3.2 Overall Windage Work

In this section, windage work on the cavity leakage flow for varying seal clearance, inlet circumferential velocity, as well the contributions of the cavity wells and labyrinth seals to the overall windage work are presented. Figure 4.20 shows that the windage heating (Eq. 2.9) increases with increasing seal clearance. For tighter clearance, the leakage flow through the cavity is relatively low which results in less shear work done on the fluid as opposed to larger seal clearance cases. On the other hand, windage heating decreases with increasing inlet circumferential velocity because for higher inlet circumferential flow, the difference between the rotor drum and cavity leakage flow velocity is smaller which results in less viscous work dissipation as well as less windage heating.

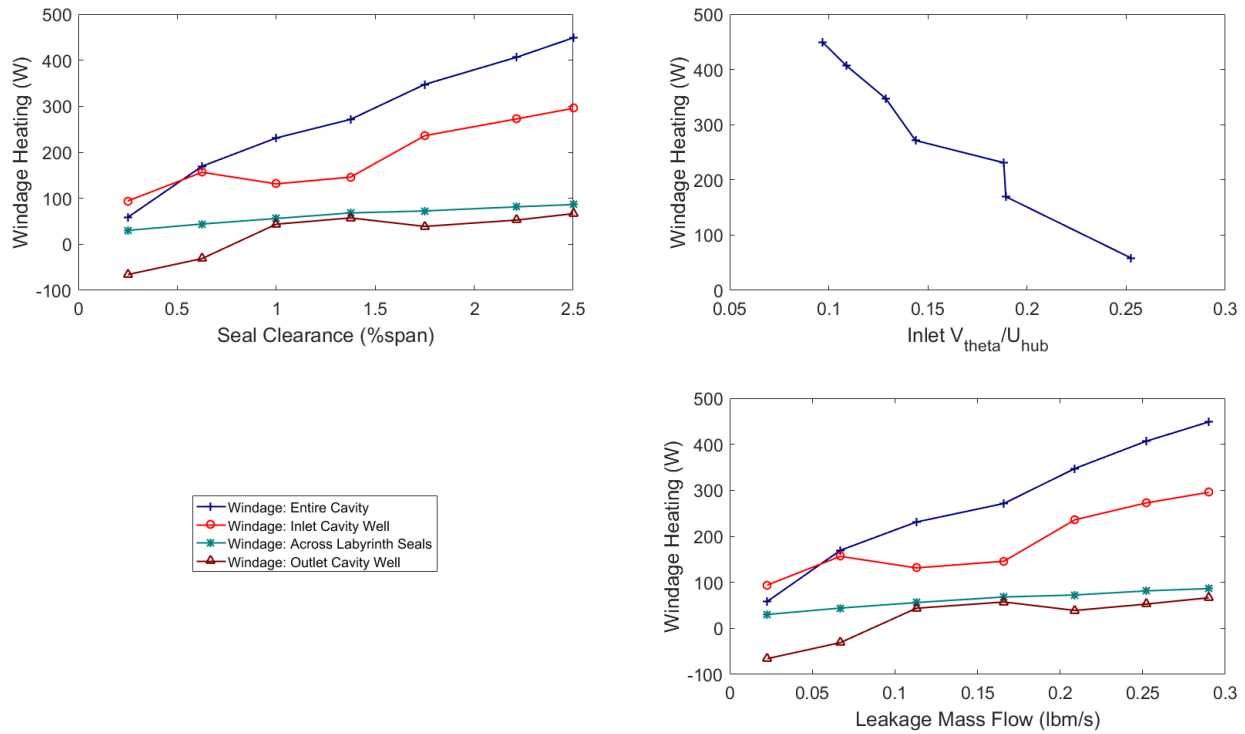


Figure 4.20: Windage heating contributions by the cavity for varying seal clearance as well as windage heating interdependence on inlet circumferential velocity.

Additionally, Figure 4.20 shows the windage work contributions by the inlet and outlet wells, and labyrinth seals. For all cases, at least 50 percent of the windage work is generated in the inlet cavity well, approximately 30 percent of the windage work is generated by the labyrinth seals, and approximately 20 percent by the outlet cavity well. More interestingly, all except the middle cases of 1.000 and 1.375 percent span clearance cases, the inlet cavity well tends to show increasing contributions to windage heating. The drop in inlet cavity well windage heating for 1.000 and 1.375 percent span is attributed to the drop in total temperature of the incoming cavity flow, as shown in Figures 4.18 and 4.19. This is another clear justification of no cavity flow re-ingestion occurring for these cases.

Hence, temperatures throughout the cavity are higher for tighter seal clearance, and they decrease asymptotically with increasing seal clearance. On the other hand, windage heating increases with increasing seal clearance due to increased cavity flow rate. Most importantly, both the temperature rise and windage heating have strong dependence on inlet circumferential velocity.

4.4 Overall Cavity Leakage Flow Characteristics

In this section, bulk flow parameters are analyzed at the inlet and outlet cavity interface to understand the changes in cavity leakage flow properties entering and leaving the primary passage with changes in the labyrinth seal clearance. First, Figure 4.21 presents the changes in total pressure at the hub-cavity interfaces. In general, total pressure tends to decrease with increasing seal clearance indicating worsening near-hub performance. Moreover, the change in total pressure increases with increasing clearance, Figure 4.22, indicating more cavity leakage flow. However, the smallest labyrinth seal clearance is an exception to this trend due to the additional vortical structure formation on the downstream surface of the outlet cavity well which skews the area average at the outlet interface. More importantly, the change in total pressure decreases as the inlet circumferential velocity increases. This indicates that the hub total pressure loss can be decreased by increasing the circumferential velocity of the fluid entering the cavity at stator exit. In this case, hub total pressure losses decreased by 0.9 percent for every 10 percent increase in circumferential velocity at the stator exit. Similar observation was reported by Demargne (2000) for investigations carried out using a linear cascade experimental setup. In that case, the hub stagnation pressure loss decreased by 0.85 percent for every 10 percent increase in circumferential velocity.

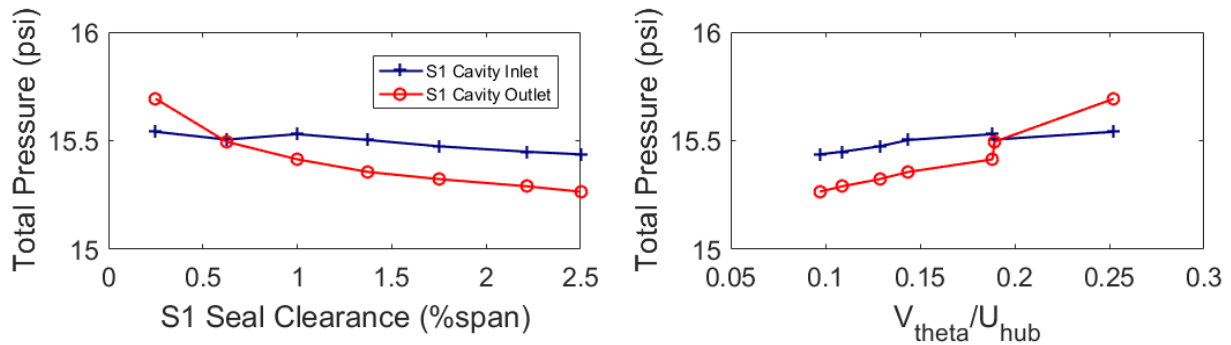


Figure 4.21: Changes in total pressure at the hub-cavity interfaces for varying seal clearance and inlet circumferential velocity.

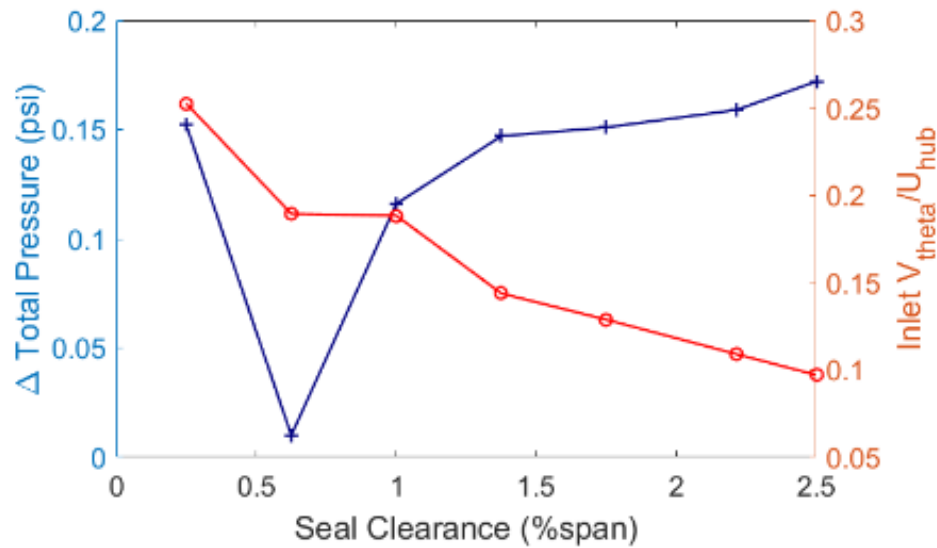


Figure 4.22: Change in total pressure from inlet to outlet cavity interfaces for varying seal clearance and inlet circumferential velocity.

Next, Figure 4.23 presents the changes in circumferential velocity at the hub-cavity interfaces. Here, the circumferential velocity of both the flow entering and leaving the cavity decreases with increasing seal clearance. More importantly, the rise in circumferential momentum across the cavity decreases with increasing seal clearance. Similar observations were reported by (Wellborn 2001, Heidegger, 1996) where increasing the leakage amount typically reduced the increase in circumferential velocity across the cavity. As the seal clearance increases, i.e. cavity leakage amount increases, the frictional momentum is transferred over more fluid which, in turn, results in a reduced circumferential momentum rise. Since the leakage fluid's flow path is closest to the rotor drum for majority of the path, the circumferential velocity of the leakage flow approaches wheel speed. However, the wheel speed is constant for this investigation. Therefore, increased wheel speeds will lead to increased circumferential velocity and increased incidence as compressor designs evolve to higher wheel speeds. Hence, since both, the cavity leakage flow rate and the circumferential velocity change, tend to affect compressor performance near the hub, these conclusions can be significant for designers.

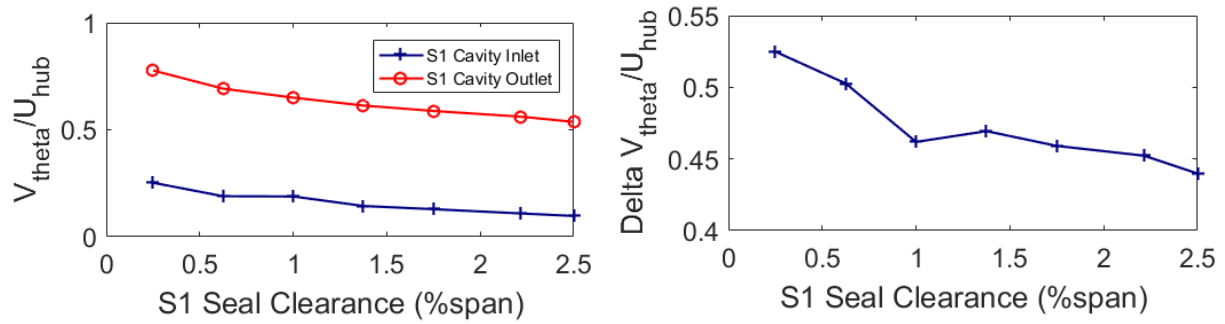


Figure 4.23: Circumferential velocity changes from inlet to outlet cavity interfaces for varying seal clearance and inlet circumferential velocity.

As expected, Figure 4.24 shows the increase in radial momentum with increase in seal clearance. Intuitively, when the seal clearance increases and allows for higher cavity leakage flow rates, the magnitude of radial velocity increases. The negative magnitude of the cavity inlet well profile indicates flow entering the cavity. Nevertheless, the inlet and outlet radial velocity profiles are mirrored across the abscissa stating that the flow enters and exits the inlet and outlet interfaces with nearly the same magnitude.

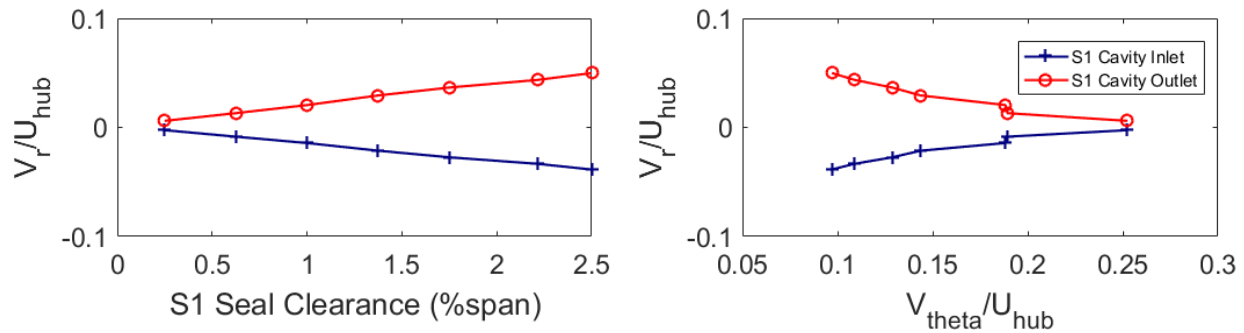


Figure 4.24: Changes in radial velocity at the hub-cavity interfaces for varying seal clearance and inlet circumferential velocity.

CHAPTER 5. CONCLUSIONS AND RECOMMENDATIONS

The principal objective of this work was to investigate flow physics in the stator cavity wells for understanding the flow path of the cavity leakage fluid as well as windage heating within the cavity. The investigations presented in this work consist of a series of numerical simulations using ANSYS CFX Solver, a CFD tool, on a parametric model of the Purdue 3-Stage Compressor Facility with the ability to apply rapid geometric modifications to the labyrinth seal clearance in a coupled stator and cavity system. Measurements performed by the previous investigators on the P3S facility were utilized for defining the boundary conditions of the parametric model. The goal of this study was to characterize the interdependence of parameters such as cavity leakage flow rate, circumferential velocity development, and windage heating for understanding the flow structure inside the cavity wells as well as their impact on cavity temperatures. The data acquired from the computational model reveals the mechanisms through which cavity leakage flows affect the stator passage aerodynamics as well as the windage heating within the cavity, both regarding their flow effect on the compressor performance and regarding the details of the flow path within the cavity wells. This study also investigates the cavity wells to understand the development of circumferential velocity and temperature in the cavity wells. While some of the results related to the overall impact on the stator passage are reiterated from the existing literature, the details inside the cavity wells of a coupled cavity model, which are largely missing in the existing literature due to linear cascades or standalone labyrinth seal investigations, are revealed by this study. Consequently, this understanding will provide insight into how the added complexities of the cavity wells and long rotating walls on the cavity leakage flow might influence the design considerations for optimizing stator passage aerodynamics as well as minimizing stator cavity heating.

First, the performance of the standalone model showed that not modeling the cavity results in underpredicting hub temperatures, flow deviation, and overestimated performance. For the stator passage performance, increase in seal clearance leads to increased leakage mass flow across the labyrinth seals causing a decrease in compressor performance. Every 1 percent increase in labyrinth seal clearance-to-percent span indicated an approximate 0.50 percent increase in cavity leakage flow, 0.60 percent decrease in TPR, and 0.50-point decrease in efficiency. Since this performance degradation corresponds to varying the stator 1 cavity only, the performance

degradation is likely higher while varying all labyrinth seal clearances. Nevertheless, the performance degradation is due to the cavity leakage flow disrupting the near-hub stator flow field and producing deteriorated stator exit flow conditions. The radial profiles at stator exit along with detailed contours showed increasing leakage producing additional flow blockage, deviation, and total pressure loss near the hub. Most importantly, as the labyrinth seal clearance increase, the increased leakage flow causes the blockage to shift radially outwards towards the shroud. However, the losses near the midspan region of the stator remained largely unchanged. Below the 50 percent span region, the cavity seal clearance dictates the amount of radial mixing occurring in the primary passage, with tighter clearances limiting radial mixing below 10 to 15 percent span, but larger clearance deteriorated performance as high as 30 percent span.

This altered flow is caused by the leakage fluid originating at the stator leading edge which controls the circumferential momentum near the hub. When the cavity circumferential momentum is low the cavity leakage flow collects on the stator suction surface aggravating the hub corner separation and hurting the stator performance. Otherwise, high cavity circumferential momentum restricts the cavity leakage flow on the stator pressure side. The investigations showed tighter labyrinth seal clearance correlated with higher circumferential momentum near the hub restricting the hot cavity leakage flow on the pressure side, while larger labyrinth seal clearance led to lower circumferential momentum near the hub leading to cavity leakage flow collecting on the stator suction surface and aggravating the hub corner separation. The total pressure and total temperature contours along the chord of the stator showed this apparent cross-passage migration, which is responsible for corner separation. For the cases with small cavity clearance (≤ 0.625 percent span), the streamlines on the suction side of the stator vane showed minor separation along the hub corner starting at near 75 percent chord and extending radially to 20 percent span near the trailing edge. For large clearances (≥ 1.75 percent span), the hub corner separation was worsened as more flow could pass through the cavity starting at nearly 50 percent chord and extending radially as high as 30 percent span. Nevertheless, two cases (1.000 and 1.375 percent span) showed improvements for the separation on the suction side with the hub corner starting at nearly 80 percent chord and extending radially to only 15 percent span near the trailing edge. Therefore, the circumferential velocity, which is inherently dependent on the labyrinth seal clearance, has a major influence on the primary passage flow field near the hub and greatly influences the aerodynamic design. Nevertheless, this disruption of the primary passage flow deteriorated the stator exit conditions

which led to downstream stages suffering more degradation as the deteriorated flow reached the rotor in the next stage. The radial profiles showed that the downstream rotor is not able to improve the degraded incoming flow near-hub and the near-hub performance of the downstream stator continues to deteriorate.

Next, investigating the hub-cavity interfaces revealed that the bulk of the leakage flow entered or left the cavity near the downstream face of the interface gap. More importantly, the leakage flow originating at the stator leading edge or being ingested at the stator trailing edge also showed circumferential variations in the flow properties. Near the upstream interface, the circumferential variations existed due to the potential field established by the stator. Here the cavity leakage flow is driven radially inwards near the leading edge of the stator due to the stagnation point, while the leakage flow entered the primary passage away from the leading edge. For the downstream interface, the most apparent variations were caused by secondary flow, namely the stator wakes and hub corner separations. These secondary flows governed, across the stator pitch, which fluid particles are ingested in the cavity. While the magnitude of fluid being ingested was different for all cases, the negative radial momentum region spans the entire vane passage for all cases except for 1.000 and 1.375 percent span clearance cases which show almost no negative radial momentum in the middle of the passage. While these circumferential variations have been observed in the past, no relation to re-ingestion is available in the open literature. Using 3D streamlines, this study shows that the heated efflux from the outlet cavity interface dwells in the primary passage near-hub and arrives at the negative radial momentum region at the inlet cavity interface for the tighter clearance cases but manages to avoid this zone for 1.000 and 1.375 percent span clearance cases. For larger clearance cases, the heated efflux manages to partially avoid the negative radial momentum region, but the leakage mass flow is much higher for larger clearance cases and a portion of the heated leakage flow gets re-ingested.

While the above conclusions resonate the existing aerodynamic research in the open literature, the following conclusions are unique as this study incorporates the cavity wells and long rotating rotor drum walls in the analysis instead of investigating standalone labyrinth seals or linear cascades, which are common in the existing literature. In addition to the vortical structures at the hub-cavity interface, larger vortical structures existed in the cavity wells which carved a more arduous path for the cavity leakage flow to navigate. The vortical structures were observed to be increasing in size with tighter clearance causing the flow to interact more with the rotor drum

which determined the development of the circumferential velocity as well as the temperature rise of the cavity leakage flow. The radial variations in flow profiles showed an increase in circumferential velocity for tighter clearances. The radial variations also clearly showed the re-ingestion cases achieved much higher temperatures. On the other hand, the cases that avoided re-ingestion all together registered the lowest temperatures. The rotor ledge also revealed to impart a significant amount of work on the incoming cavity leakage fluid, indicated by immediate rise in total temperature and circumferential velocity. More importantly, the vortical structures did not negatively impact the development of circumferential momentum as they rotated with the same circumferential momentum. Rather, the cavity leakage flow path being in direct contact with the stationary stator landing or rotor drum determined the transfer of circumferential momentum, because the viscous work transfers from near the rotor drum to radially outwards towards the stator landing. Similarly, vortical structures also existed at a uniform temperature and the flow profiles near the rotor drum reported higher temperatures with a steady rise in temperature observed due to frictional heating from rotor drum to cavity leakage fluid to stator landing. In general, the simulations showed that the size of both vortical structures scaled such that the distance travelled by the cavity leakage along the stator landing and rotor drum changed. Therefore, the seal clearance, the size of vortical structures, and flow path along the stator landing and rotor drum are closely dependent and play a major role in determining the development of circumferential velocity as well as temperature rise of the cavity leakage flow in the cavity wells.

Overall, at the hub-cavity interfaces, the total pressure decreased with increasing seal clearance indicating worsening near-hub performance, while total temperature increased with decreasing seal clearance indicating high metal temperatures and reduced component fatigue life. Moreover, the change in total pressure decreased and the rise in total temperature increased as circumferential velocity increased at the cavity inlet interface indicating that increased inlet circumferential velocity reduced hub total pressure loss but increased metal temperatures. Lastly, the circumferential velocity of the incoming and outgoing cavity leakage flow increased with decreasing seal clearance. Hence, these mechanisms suggested that decreasing seal clearance allows for the aerodynamic optimization, but, in practice, these considerations must be balanced by the increase in temperature rise associated with reduced cavity leakage flow rate and higher circumferential velocities. Nevertheless, for tighter clearance, the leakage flow through the cavity is relatively low which results in less shear work done on the fluid as opposed to larger seal

clearance cases. At least 50 percent of the said windage work was performed by the inlet cavity well, with the outlet cavity well and labyrinth seals accounted for 30 percent and 20 percent of the work, respectively. Furthermore, windage heating decreased with increasing inlet circumferential velocity because for higher inlet circumferential flow, the difference between the rotor drum and cavity leakage flow velocity is smaller which results in less viscous work dissipation. Therefore, total pressure loss, total temperature rise and windage heating have strong dependence on inlet circumferential velocity, which is inherently dependent on the labyrinth seal clearance.

Therefore, for future research, as the compressor designs evolve to higher wheel speeds, analysis of the cavity wells at higher rotation speeds becomes essential due to the development of higher circumferential velocity. Since majority of the parameters analyzed in this study showed strong dependence on circumferential velocity, there are many factors that will affect the leakage characteristics at increased wheel speeds. The rotation of the rotor at a different speed will change the flow structure with a stronger circumferential velocity and consequently, the cavity leakage fluid will take a different flow path relative to the length travelled on the stator landing as opposed to the rotor drum. The labyrinth seals will also allow different mass flow through the cavity causing changes in the axial and radial flow losses at the hub-cavity interfaces. Higher rotation speeds will likely change the windage heating through the cavity wells and give much larger temperature rise because increasing the rotational speed leads to increased viscous work generated by the rotor. Higher rotation speeds and larger temperature rise result in larger circumferential and thermal growth of the labyrinth seals. Hence, the interdependence of all these variations will be essential while analyzing the complexities of the cavity leakage flow at different loading conditions or higher speeds. Nevertheless, the methodology for the development of the computational model and the post-processing capabilities for a thorough analysis of the interdependent parameters have been presented to aid future investigators continuing work at different rotation speeds, operating conditions or cavity geometry. This model allows for investigations at different rotational speeds and operating conditions with changes in just the boundary conditions. Although, for investigations of cavity leakage effects in a different geometry, the near-hub and boundary layer resolution of the computational domain become increasingly important. A thorough grid convergence study near the hub, stator landing, and rotor drum is recommended for ensuring model fidelity when analyzing temperature rise and circumferential velocity development in the cavity wells or while tracking cavity leakage flow particles for re-ingestion.

APPENDIX A. ADDITIONAL RESULTS – CAVITY INLET WELL

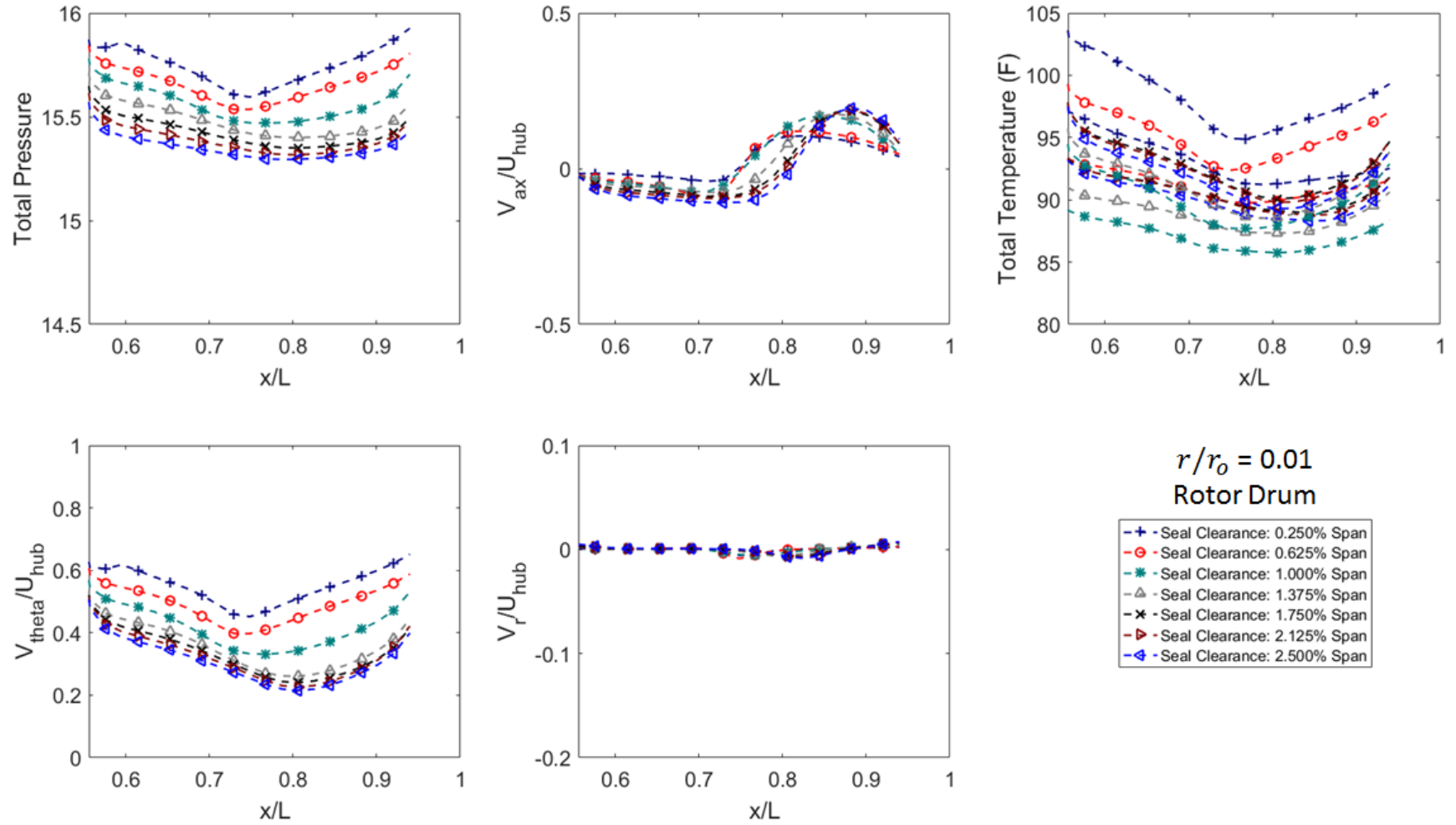


Figure A.1: Variations in flow profiles at radius ratio 0.01 in the cavity inlet well for varying seal clearance

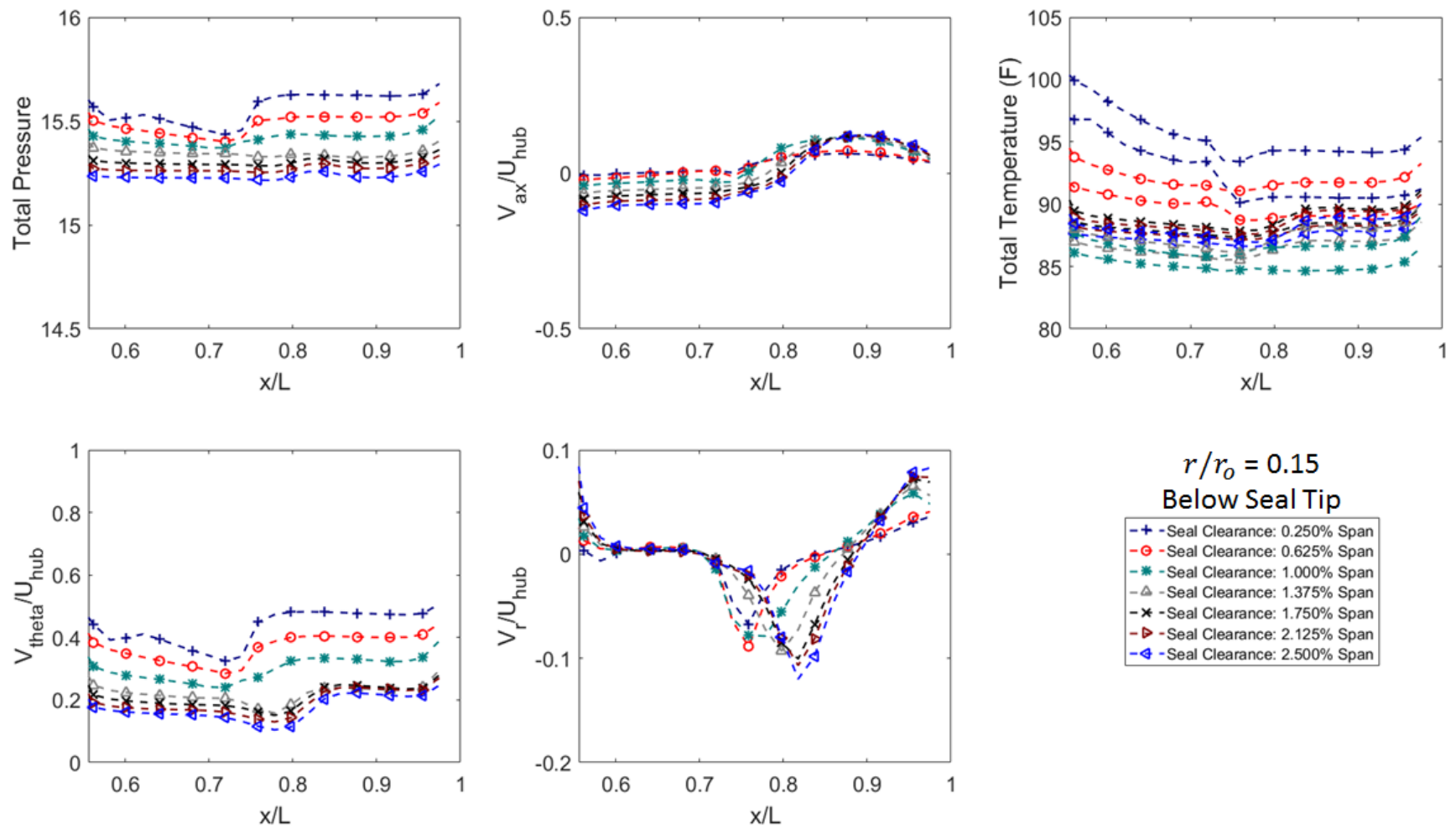


Figure A.2: Variations in flow profiles at radius ratio 0.15 in the cavity inlet well for varying seal clearance

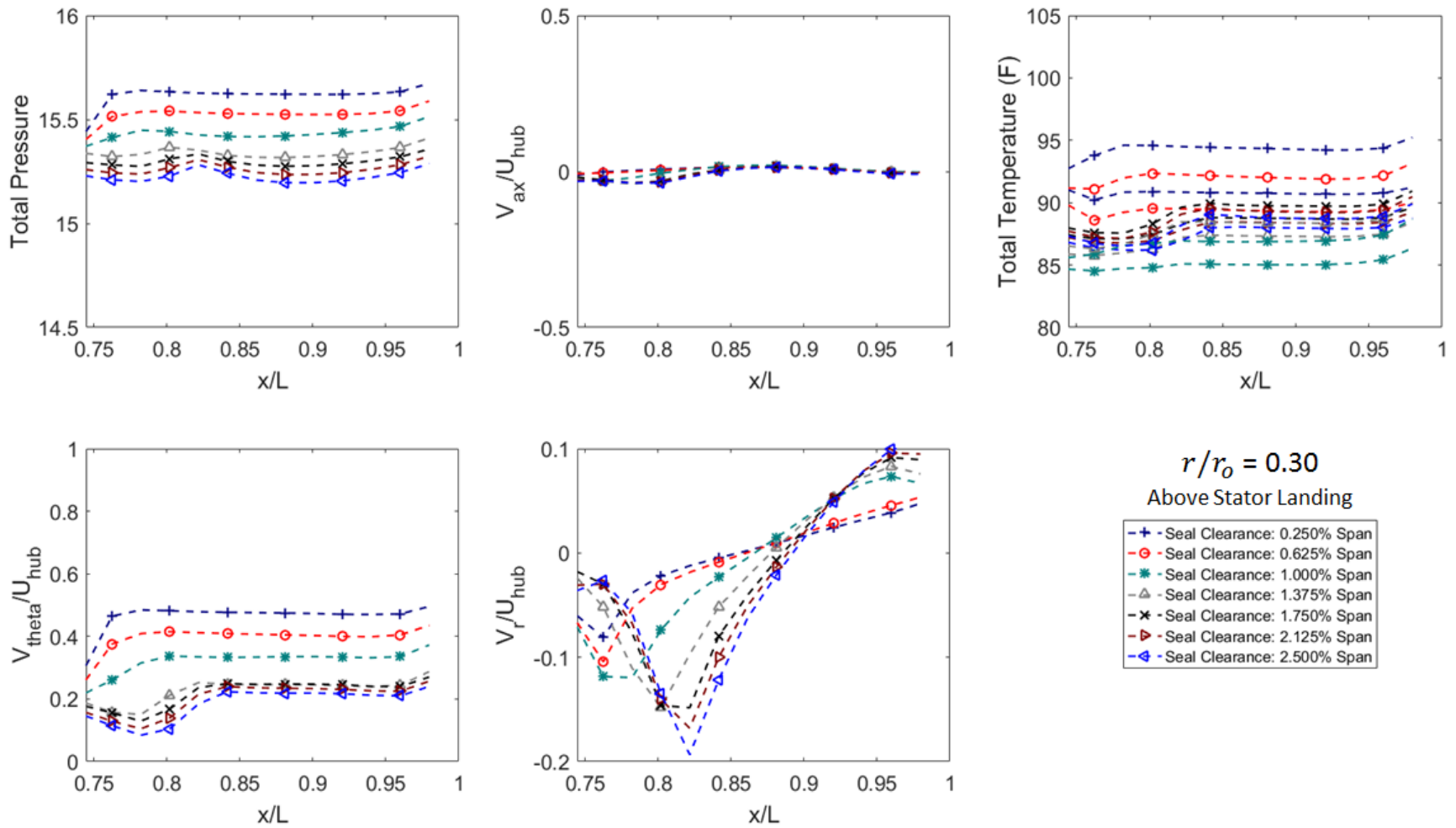


Figure A.3: Variations in flow profiles at radius ratio 0.30 in the cavity inlet well for varying seal clearance

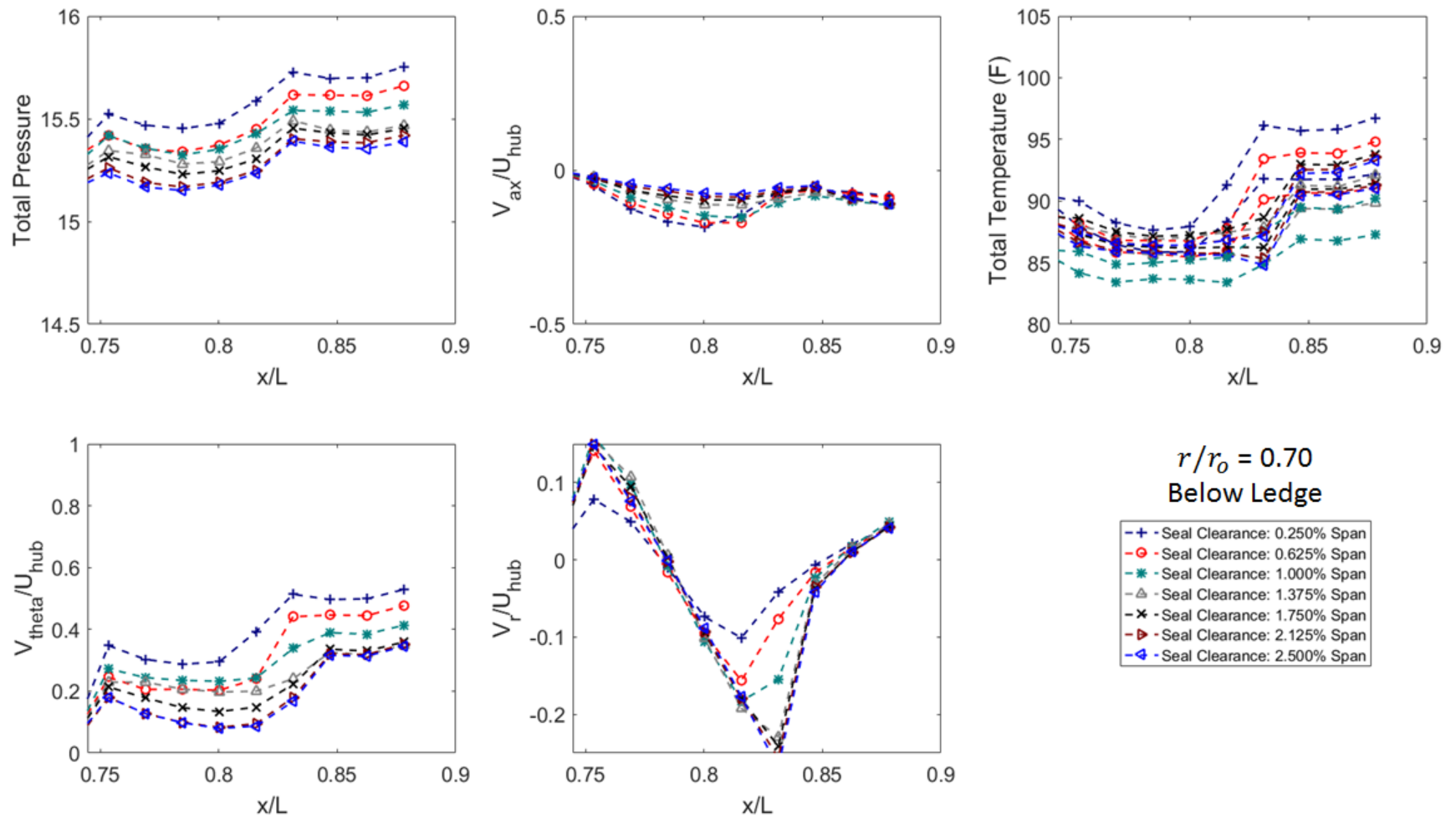


Figure A.4: Variations in flow profiles at radius ratio 0.70 in the cavity inlet well for varying seal clearance

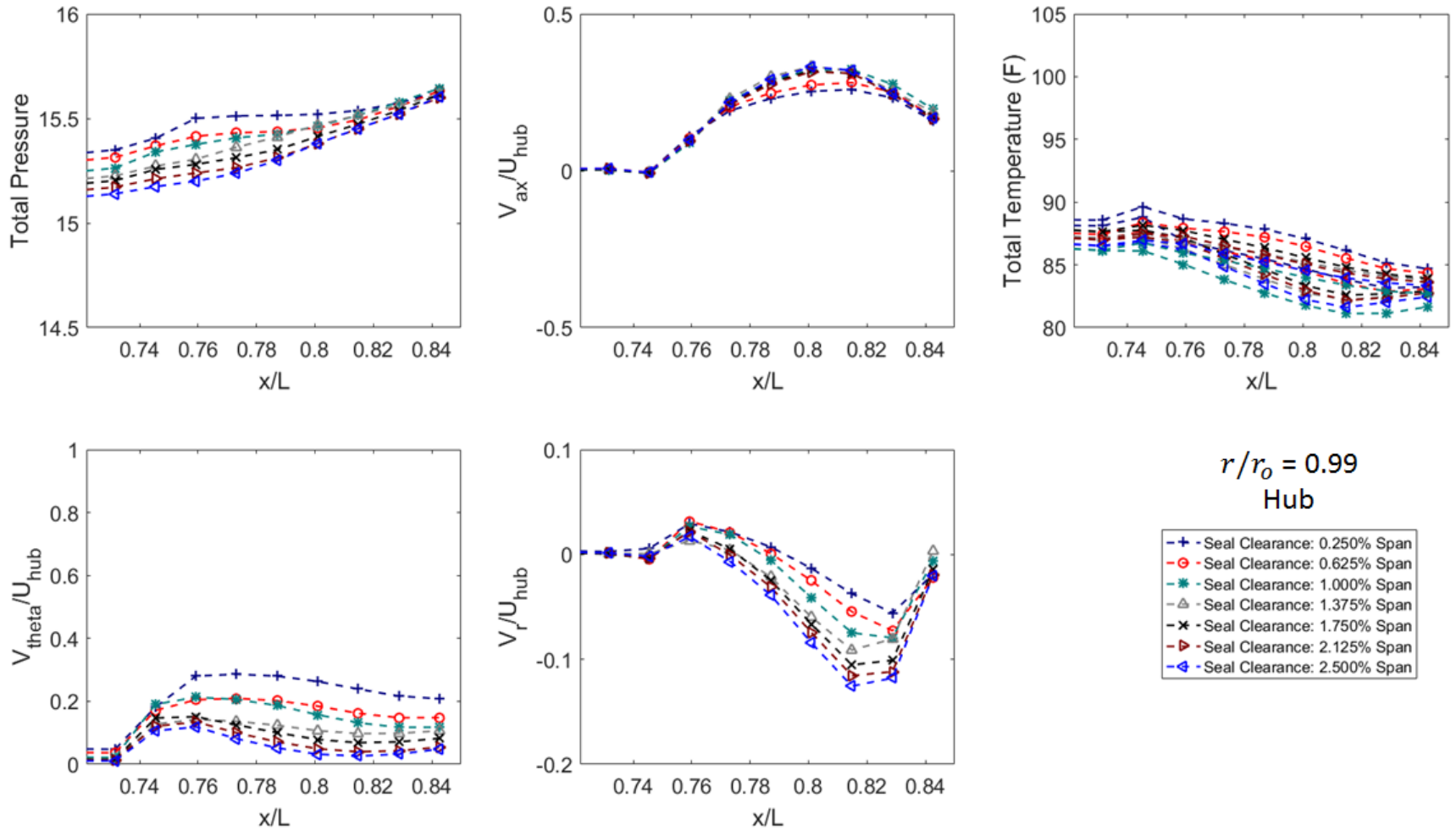


Figure A.5: Variations in flow profiles at radius ratio 0.99 in the cavity inlet well for varying seal clearance

APPENDIX B. ADDITIONAL RESULTS – CAVITY OUTLET WELL

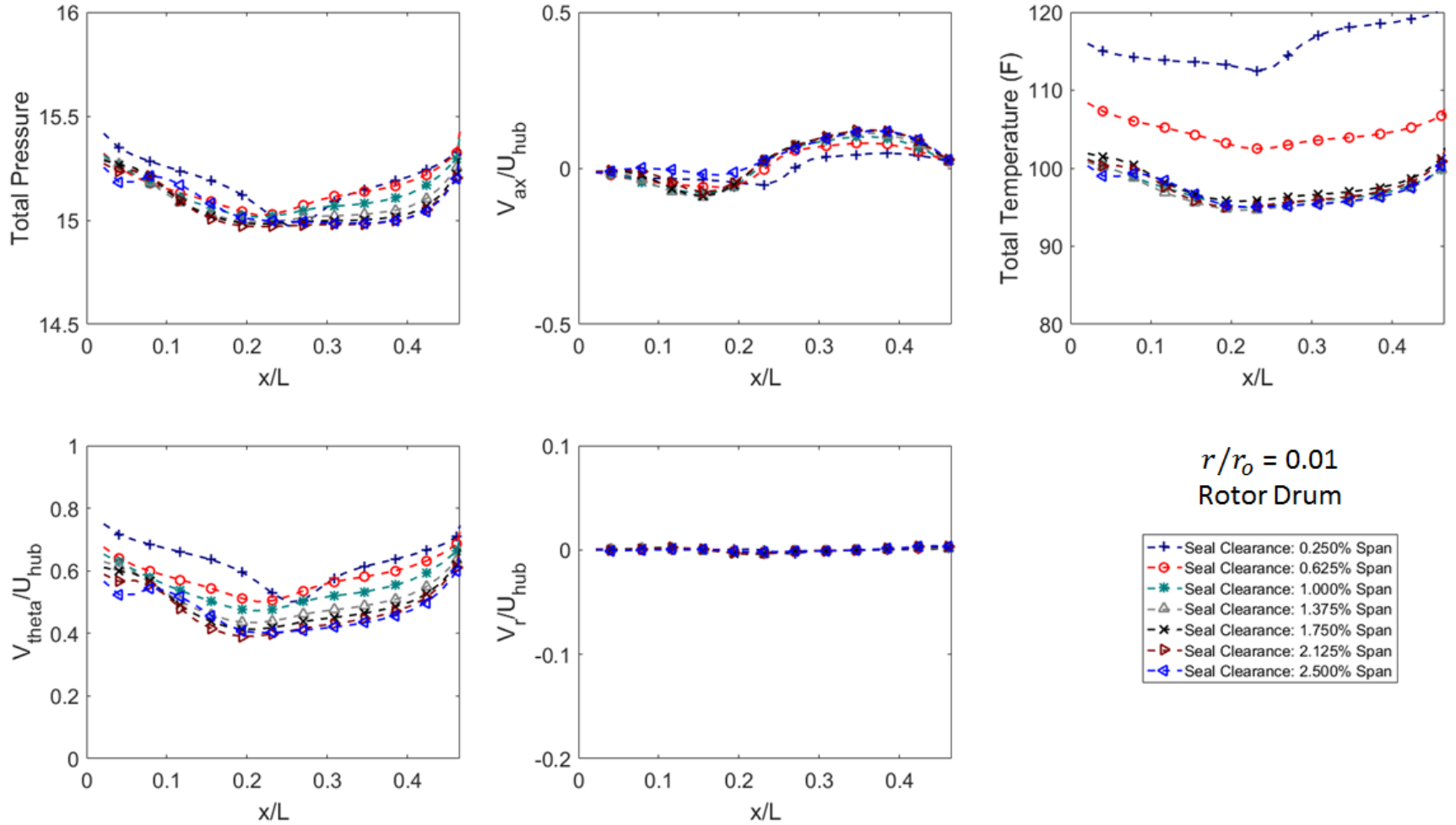


Figure B.1: Variations in flow profiles at radius ratio 0.01 in the cavity outlet well for varying seal clearance

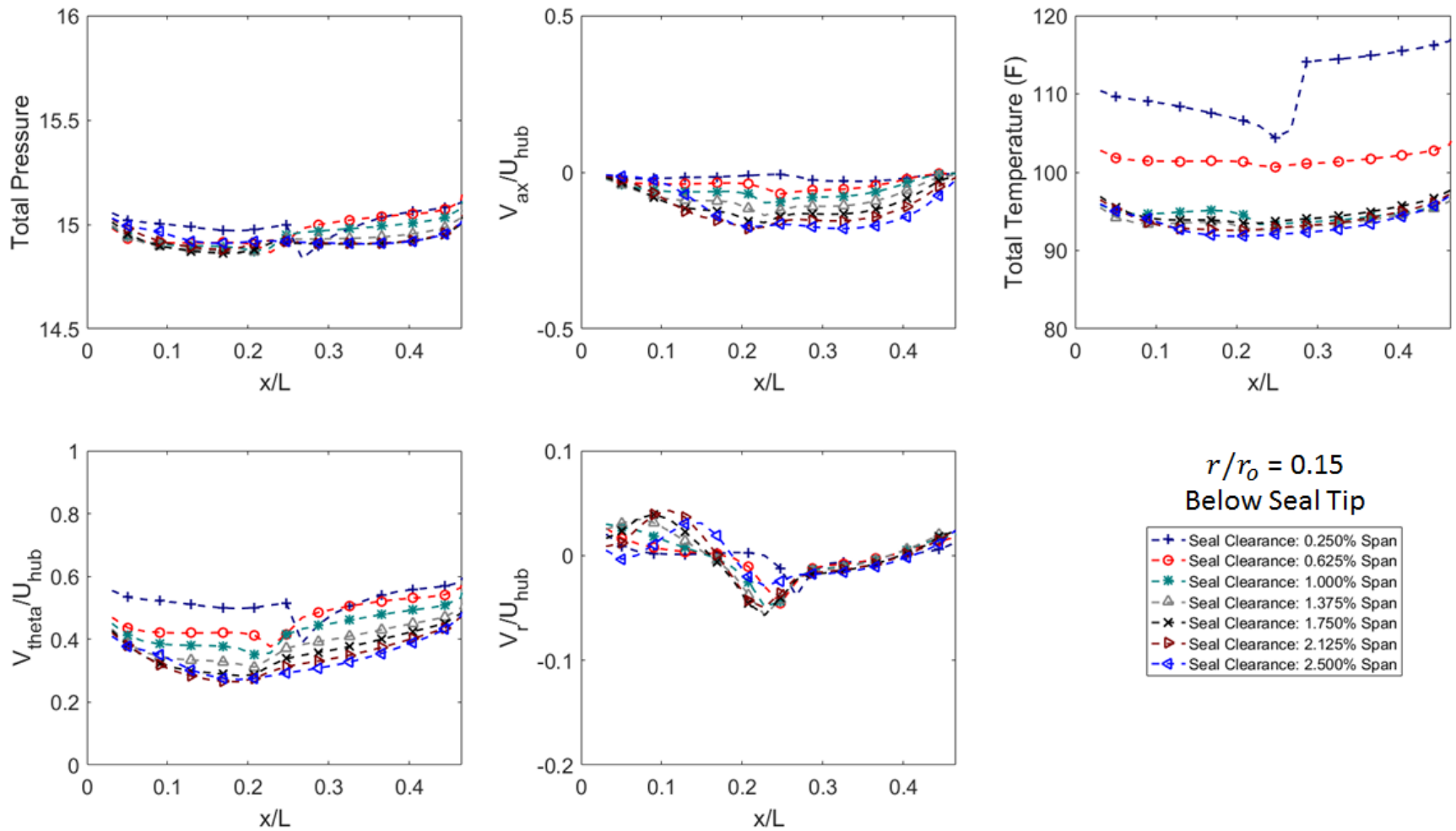


Figure B.2: Variations in flow profiles at radius ratio 0.15 in the cavity outlet well for varying seal clearance

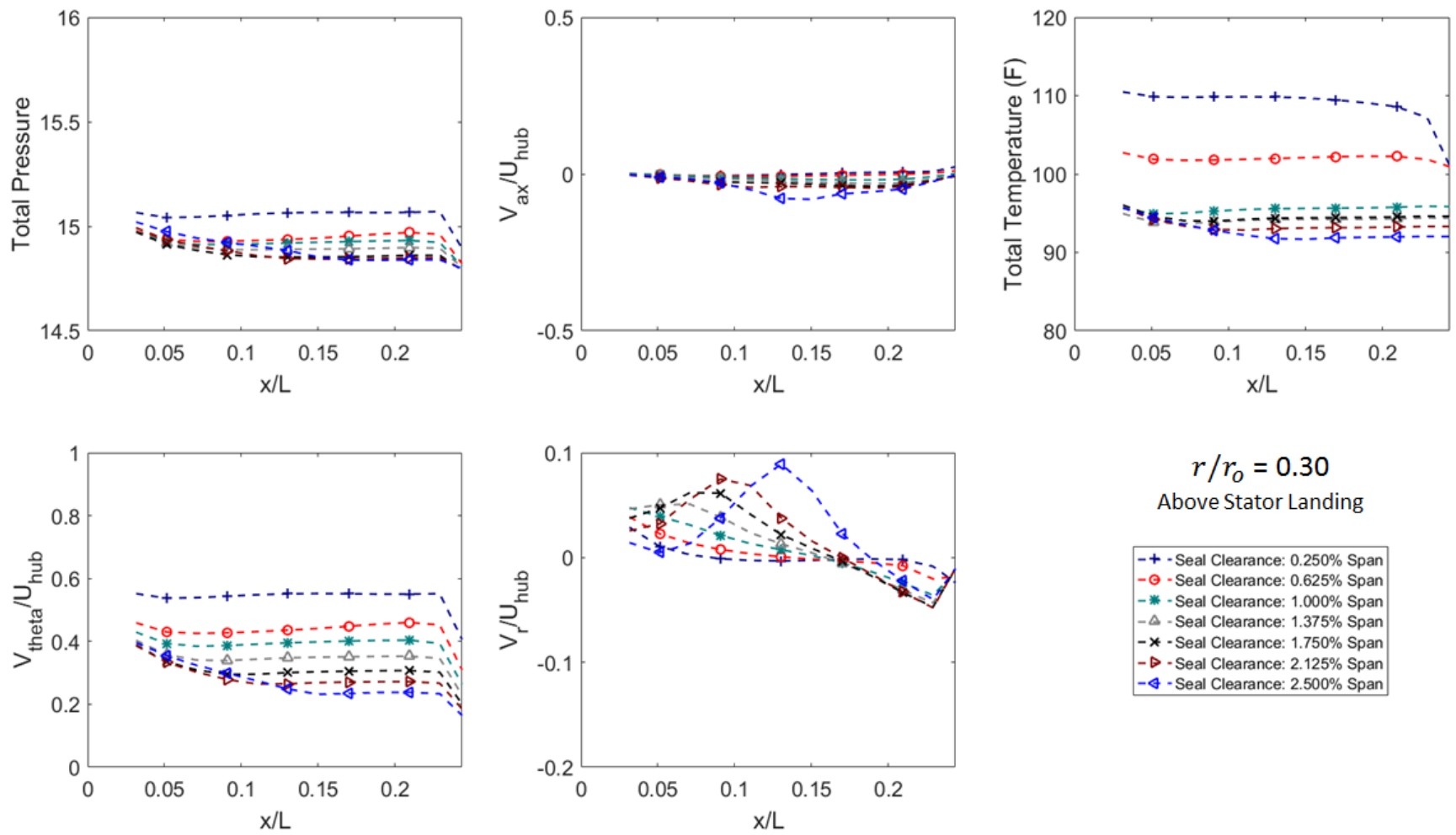


Figure B.3: Variations in flow profiles at radius ratio 0.30 in the cavity outlet well for varying seal clearance

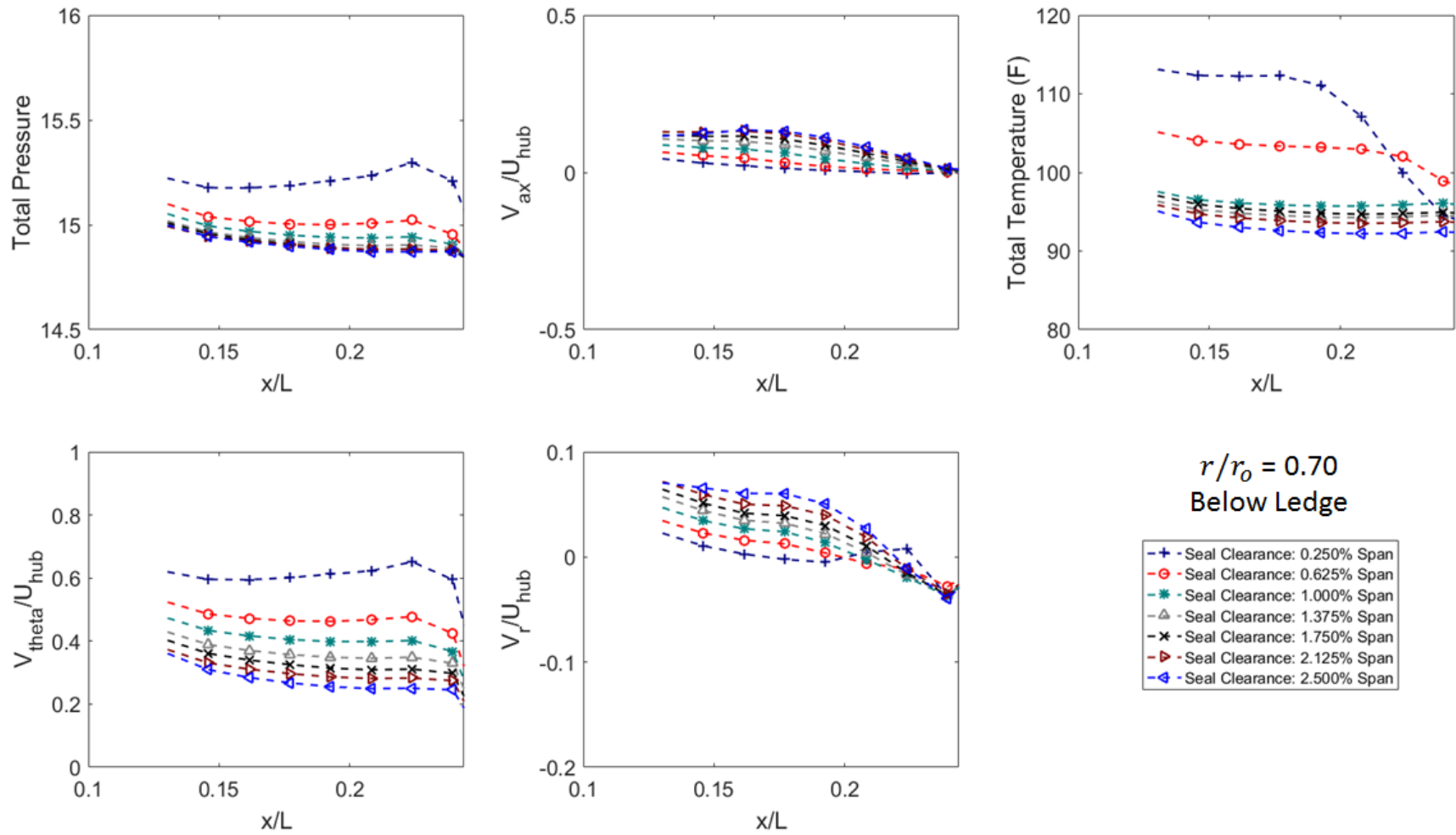


Figure B.4: Variations in flow profiles at radius ratio 0.70 in the cavity outlet well for varying seal clearance

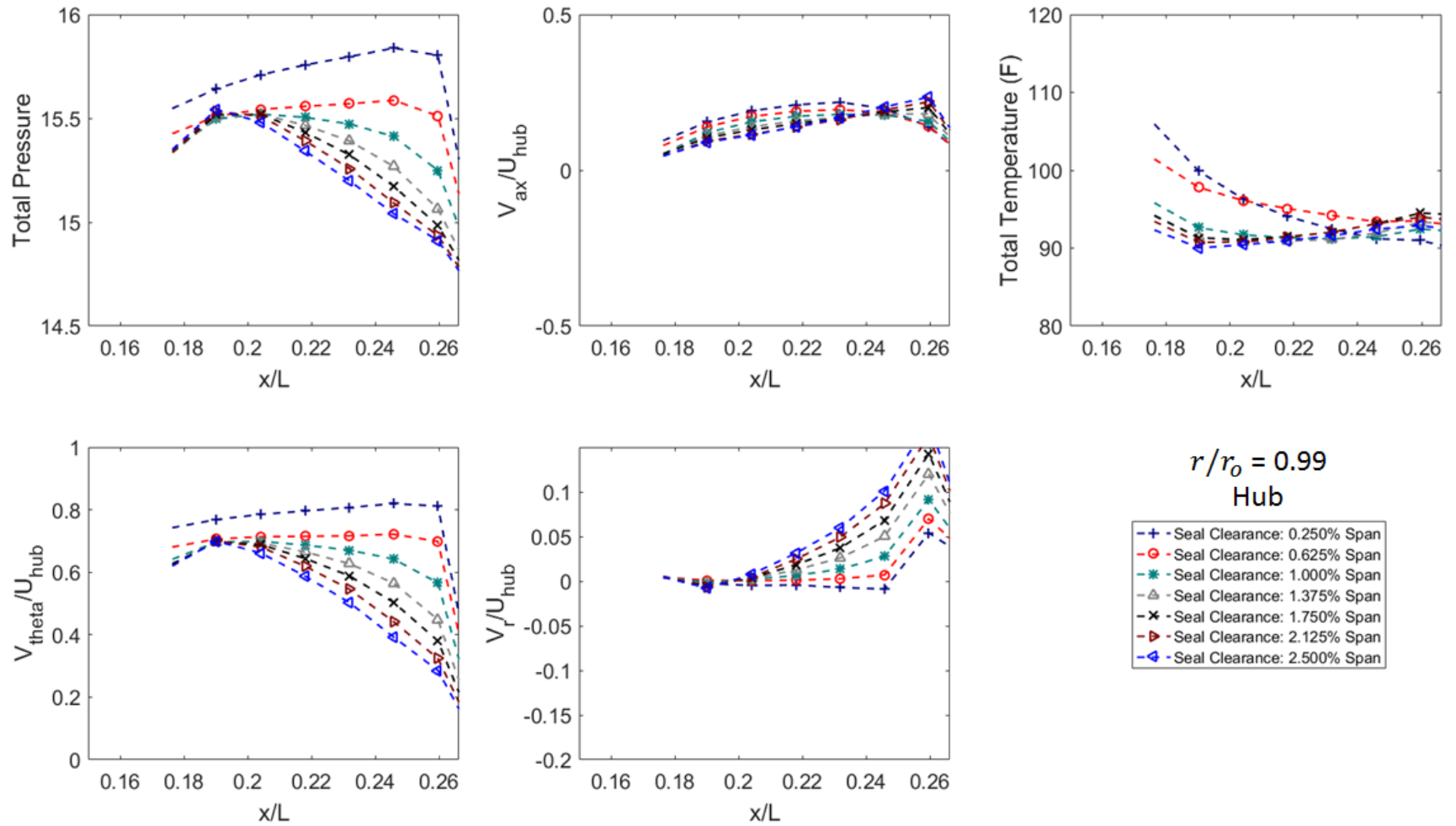


Figure B.5: Variations in flow profiles at radius ratio 0.99 in the cavity outlet well for varying seal clearance

REFERENCES

- ANSYS CFX-Reference Guide, 2018, Canonsburg, PA: ANSYS.
- ANSYS CFX-Solver Theory Guide, 2018, Canonsburg, PA: ANSYS.
- ANSYS Meshing Users Guide, 2018, Canonsburg, PA: ANSYS.
- ANSYS TurboGrid Users Guide, 2018, Canonsburg, PA: ANSYS.
- Ball, P.R., 2013, “An Experimental and Computational Investigation on the Effects of Stator Leakage Flow on Compressor Performance,” Purdue University, Master Thesis.
- Bayley, F.J. and Childs P.R.N., 1994, “Air Temperature Rises in Compressor and Turbine Stator Wells,” ASME Paper 94-GT-185.
- Berdanier, R.A. and Key, N.L., 2015b, “An Experimental Investigation of the Flow Physics Associated with End Wall Losses and Large Rotor Tip Clearances as Found in the Rear Stages of a High-Pressure Compressor,” NASA/CR-2015-218868.
- Brossman, J.R., 2012, “An Investigation of Rotor Tip Leakage Flows in the Rear-Block of a Multistage Compressor,” Purdue University, PhD Thesis.
- Demargne, A.A.J. and Longley, J.P., 2000, “The Aerodynamic Interaction of Stator Shroud Leakage and Mainstream Flows in Compressors,” ASME Paper 2000-GT-507.
- Denecke, J., Dullenkopf, K., Wittig, S., and Bauer, H.J., 2005, “Experimental Investigation of the Total Temperature increase and Swirl Development in Rotating Labyrinth Seals,” ASME Paper GT2005-68677, pp. 1161-1171.
- Denecke, J., Dullenkopf, K., Farber, J., and Bauer, H.J., 2008, “Interdependence of Discharge Behavior, Swirl Development and Total Temperature Increase in Rotating Labyrinth Seals,” ASME Paper GT2008-51429, pp. 1717-1724.
- Flores, D. and Seume, J.R., 2014, “Selecting Cavity Geometries for Improving the Aerodynamic Performance of an Axial Compressor,” ASME Paper GT2014-25328.
- Freeman, C., 1985, “Effect of Tip Clearance Flow on Compressor Stability and Performance,” von Karman Institute for Fluid Dynamics Lecture Series 1985-05.
- Heidegger, N.J., Hall, E.J., and Delaney, R.A., 1996, “Parameterized Study of High-Speed Compressor Seal Cavity Flow,” AIAA Paper 96-2807.

- Kong, X., Liu, G., Liu, Y., and Feng, Q., 2016, "Investigation on the Leakage Flow, Windage Heating and Swirl Development of Rotating Labyrinth Seal in a Compressor Stator Well," ASME Paper GT201-56740.
- Lewis, L.V., 2002, "In-Engine Measurements of Temperature Rises in Axial Compressor Shrouded Stator Cavities," ASME Paper No. GT2002-30245, pp 781-794.
- Li, J., Yan, X., and Feng, Z.P., 2006, "Effects of Pressure Ratio and Fin Pitch on Leakage Flow Characteristics in High Rotating Labyrinth Seals," ASME Paper GT2006-91145.
- Ludwig, L., 1978, "Gas Path Sealing in Turbine Engines," *Seal Technology in Gas Turbine Engines*, AGARD Publication.
- McGreehan, W.F. and Ko, S.H., 1989, "Power Dissipation in Smooth and Honeycomb Labyrinth Seals," ASME Paper 89-GT-220.
- Millward, J.A. and Edwards, M.F., 1996, "Windage Heating of Air Passing Through Labyrinth Seals," *Journal of Turbomachinery*, **118**(2), pp. 414-419.
- Nayak, K.C. and Dutta, P., 2016, "Numerical Investigations for Leakage and Windage heating in Straight-Through Labyrinth Seals," *Journal of Engineering for Gas Turbines and Power*, **138**(1).
- Naylor, E., Montomoli, F., Hodson, H., and Lapworth, L., 2009, "Numerical Modeling of Cavities in Multistage Axial Compressors," ISABE-2009-1186.
- Oztruk, H.K., Childs, P.R.N., Turner, A.B., Hannis, J.M., and Turner, J.R., 1998, "A Three-Dimensional Computational Study of Windage Heating within an Axial Compressor Stator Well," ASME Paper 98-GT-119.
- Phadke, U.P. and Owen, J.M., 1987, "Aerodynamic Aspects of the Sealing of Gas Turbine Rotor-Stator Systems, Part I, II, and III," School of Engineering and Applied Sciences, University of Sussex Report 86/TFMRC/94.
- Scott, R.M., Childs, P.R.N., Hills, N.J., and Milward, J.A., 2000, "Radial Inflow into the Downstream cavity of a Compressor Stator Well," ASME Paper 2000-GT-507.
- Talalayev, A., 2011, "On the Renovation of the Three-Stage Axial Compressor Facility for Compressor Performance Research," Purdue University.
- Waschka, W., Wittig, S., and Kim, S., 1992, "Influence of High Rotational Speeds on the Heat Transfer and Discharge Coefficients in Labyrinth Seals," *Journal of Turbomachinery*, **114**(2), pp. 462-468.

- Wellborn, S.R. and Okiishi, T.H., 1996, "Effects of Shrouded Stator Cavity Flows on Multistage Axial Compressor Aerodynamic Performance," NASA CR 198536.
- Wellborn, S.R. and Okiishi, T.H., 1999, "The Influence of Shrouded Stator Cavity Flows on Multistage Compressor Performance," *Journal of Turbomachinery*, **122**(3), pp. 486-497
- Wellborn, S.R., Tolchinsky, I., and Okiishi, T.H., 2000, "Modeling Shrouded Stator Cavity Flows in Axial-Flow Compressors," *Journal of Turbomachinery*, **122**(1), pp. 55-61
- Wellborn, S.R., 2001, "Details of Axial-Compressor Shrouded Stator Cavity Flows," ASME Paper No. 2001-GT-0495.
- Wisler, D. C., 1985, "Aerodynamic effects of tip clearance, shroud, leakage flow, casing treatment and trenching in compressor design blading design in the end-wall region," von Karman Institute for Fluid Dynamics Lecture Series 1985-05.
- Wisler, D. C., 1988, *Advanced Compressor and Fan Systems*, GE Aircraft Engines, Cincinnati, Ohio; also 1986 Lecture to ASME Turbomachinery Institute, Ames, Iowa.